To the Graduate Council:

I am submitting herewith a dissertation written by Sharon Leigh White entitled "A Study of Small Angle Radiative Bhabha Scattering and Measurement of the Luminosity at SLD". I have examined the final copy of this dissertation for form and content and recommend that it be accepted in partial fulfillment of the requirements for the degree of Doctor of Philosophy with a major in Physics.

William M. Bugg, Major Professor

We have read this dissertation
and recommend its acceptance:

Accepted for the Council:

Associate Vice Chancellor
and Dean of The Graduate School

A STUDY OF SMALL ANGLE RADIATIVE BHABHA SCATTERING AND MEASUREMENT OF THE LUMINOSITY AT SLD

A DISSERTATION
PRESENTED FOR THE
DOCTOR OF PHILOSOPHY
DEGREE
THE UNIVERSITY OF TENNESSEE, KNOXVILLE

BY
SHARON LEIGH WHITE
DECEMBER, 1995

This dissertation is dedicated to my parents, Perry and Marguerite White.

Acknowledgements

As I reach the completion of my degree, there are many people I want to thank for their help along the way. First I would like to thank my advisor, Bill Bugg, who has taught me a great deal and has provided guidance throughout the process of completing my degree despite a very busy schedule as department head. I would also like to thank the other members of my committee, George Condo, Tom Handler, Bennie Ward, and Richard Williams for reading my dissertation and providing many useful comments and suggestions. In particular I'd like to thank Bennie Ward, co-author of the BHLUMI Monte Carlo program used throughout this dissertation, for many useful discussions about the use of BHLUMI. I would also like to thank Joe Hargis for the many hours he spent running BHLUMI events through the full shower simulation.

The luminosity monitor was the responsibility of the University of Oregon and the University of Tennessee, and I want to thank the members of these groups for the design, construction and operation of the SLD luminosity monitor - Steve Berridge, Bill Bugg, Rob Kroeger, and Achim Weidemann from Tennessee, and Jim Brau, Ray Frey, Koichiro Furuno, Jenny Huber, Hyun Hwang, Matt Langston, Hwanbae Park, Kevin Pitts, and Cary Zeitlin from Oregon. In particular I want to thank Kevin Pitts for many useful discussions about luminosity measurement and for providing me with luminosity monitor figures for this dissertation. I would also like to thank Hwanbae Park for helpful advice on SLD code. The SLD experiment could not operate without the extraordinary efforts of many people and I'd like to thank the entire SLD and SLC collaborations. This work was supported in part by U.S. Department of Energy grant number DOE DE-FG05-91ER40627.

In the final stages of the preparation of this dissertation I received much helpful advice from three Tennessee students who preceded me in the completion of their degrees; Kathy Danyo Blackett, Gavin Blackett, and Murali Pisharody.

Finally, the support of family and friends helped to sustain me in my years of graduate study. I would especially like to thank my parents, Perry and Marguerite White, and my sister, Sarah White, for their continual support and encouragement. They always knew I could do it.

Abstract

Small angle Bhabha scattering ($e^+e^- \rightarrow e^+e^-$) is used to measure the luminosity for the 1993 run of the SLD experiment. SLD operates at the Stanford Linear Collider at Stanford Linear Accelerator Center where electrons and positrons are collided at center of mass energy on the Z^0 resonance. A silicon tungsten luminosity monitor is used to record the Bhabha events and a description of this device and its performance is presented. The luminosity is measured using two different methods to correct for small displacements in the luminosity monitor and the results are:

$$\mathcal{L} = 1726.5 \pm 5.1_{stat} \pm 3.9_{sys} \pm 4.6_{MC} \ \text{nbarn}^{-1}$$

$$\mathcal{L} = 1718.5 \pm 5.0_{stat} \pm 2.2_{sys} \pm 5.5_{MC} \ \text{nbarn}^{-1}$$

Measurement of the integrated luminosity is essential for the determination of the cross section for all final states in the experiment.

Radiative Bhabha events are studied using two types of radiative events; those with a photon visible in the luminosity monitor, and events with an undetected photon radiated down the beampipe, i.e. less than 28 mrad. The measured cross sections for these types of events in the acceptance region of the luminosity monitor are compared with Monte Carlo predictions from the BHLUMI 2.01 Monte Carlo. These cross sections are $\sigma_{sep\ photon} = 0.644 \pm 0.019_{stat} \pm 0.013_{sys} \pm 0.003_{lum}$ nbarn for the events with an identifiable photon in the luminosity monitor, and $\sigma_{beampipe} = 7.45 \pm 0.22_{sys} \pm 0.07_{stat} \pm 0.03_{lum}$ nbarn for events with a photon down the beampipe. Characteristics of the radiative events including photon energy distribution and acollinearity distributions are compared with the BHLUMI predictions.

Contents

List of Tables

List of Figures

Chapter 1

Introduction

This dissertation will present a study of small angle Bhabha scattering, ($e^+e^- \rightarrow e^+e^- + n\gamma$) at a center of mass energy on the Z^0 resonance. The data were taken using the SLAC Large Detector (SLD), operating at the Stanford Linear Collider (SLC) at Stanford Linear Accelerator Center (SLAC). A measurement of the luminosity for the 1993 SLD run will be presented. At e^+e^- colliders the measurement of the cross section of various processes is done by first monitoring a process whose cross section is well known from theory. Bhabha scattering is used for this purpose, since at small angles the cross section is well known from theory. The luminosity is calculated from $\mathcal{L} = N/\sigma$ where N is the number of Bhabha events and σ is the cross section for Bhabha scattering. This relationship between luminosity and cross section is true for any other process X, so that $\sigma_x = N_x/\mathcal{L}\epsilon_x$ where N_x is the number of events measured for the process X and ϵ_x is the relative efficiency for measuring this process with respect to measuring Bhabha events. A silicon tungsten luminosity monitor (LMSAT) was used to record Bhabha scattering events at small angles, 28 to 68 mrad. At small angles the theoretical cross section for Bhabha scattering can be calculated accurately from QED (quantum electrodynamics). This is done with the Monte Carlo program BHLUMI 2.01, a state of the art Monte Carlo generator for Bhabha scattering. The BHLUMI program explicitly generates multiple photons, so that a detailed comparison of radiative Bhabha events with Monte Carlo is possible. A study of two types of radiative Bhabha events is presented; events with a visible photon in the luminosity monitor, and events with highly forward photons radiated down the beampipe. The measured cross section for each type of event in the luminosity monitor is compared with the Monte Carlo prediction from BHLUMI, and comparisons of photon energy distributions and acollinearity distributions are presented.

A brief introduction to the Standard Model is given in Chapter 2, along with a discussion of the theory of Bhabha scattering and a description of the BHLUMI Monte Carlo. Chapter 3 describes the Stanford Linear Collider and the components of SLD, with the exception of the luminosity monitor and medium angle silicon calorimeter. A detailed description of these detectors is given in Chapter 4, along with details on the performance of the luminosity monitor. Chapter 5 presents the measurement of the luminosity for the 1993 run, using two methods. Chapter 6 presents the study of small angle radiative Bhabha scattering and Chapter 7 summarizes the results.

Chapter 2

Theory

2.1 Introduction to the Standard Model

High energy physics is the study of the fundamental particles that make up the universe and the interactions between them. In the early part of this century, only a few subatomic particles were known. The electron was discovered in 1897 by J.J. Thompson, and the fact that an atom is composed of electrons surrounding a massive nucleus was discovered by Rutherford in 1910. The fact that the nucleus is composed of protons and neutrons was not fully realized until the discovery of the neutron in 1932. In 1933 the first particle of antimatter, the positron, was observed in cosmic ray experiments. Throughout the 1940's, 1950's and 1960's a plethora of different types of particles was observed in cosmic ray experiments and experiments at early accelerators using such techniques as nuclear emulsion, cloud chambers and bubble chambers. With dozens of new particles identified, the situation seemed chaotic and physicists began looking for some underlying symmetries and order behind the vast array of particles. Today, as a result of the interplay between theory and experiment over the last few decades, a simplified picture has emerged to describe the fundamental particles and forces in nature, now known as the Standard Model. One of the fundamental aspects of this model is that all matter is composed of fermions, spin one half particles divided into two classes known as quarks and leptons. Examples of leptons are electrons and neutrinos. Quarks have fractional electric charge and are not observed in a free state. They are the building blocks of protons and neutrons. Another fundamental tenet of the model is that the particles interact by the exchange of force carrying particles known as gauge bosons. The interactions between particles are due to the electromagnetic force, the weak force, and the strong force. Gravity is also a force which exists between any two objects with mass, but at the subatomic level masses are so small that gravitational effects are negligible compared to the other three forces. The electromagnetic force is the most familiar, it is the force that binds electrons inside an atom, for example. It is mediated by the photon. The strong force, mediated by the exchange of gluons, binds together the quarks inside a nucleon, and binds the nucleons together inside the nucleus of an atom. The weak force has two types of interactions; the charged current interaction, mediated by the $W^{\pm}$ bosons, and the neutral current interaction, mediated by Z^0 bosons. An example of the weak force at work is radioactive beta decay. The Standard Model actually consists of two major parts. The electromagnetic and weak interactions are unified into a single electroweak theory developed by Glashow, Weinberg and Salam in the early 1960's [1, 2, 3]. The strong interactions are described by quantum chromodynamics (QCD). (See for example, reference [4]). The following sections provide more detail on the electroweak sector of the Standard Model.

2.2 Theoretical Framework of the Standard Model

The theory describing the electroweak interaction is a non-Abelian gauge theory based on the group SU(2)$_L\times$U(1). The strong interaction, described by QCD, is based on an SU(3) gauge group. We will emphasize the electroweak theory here. The SU(2)$_L$ group describes the weak interaction, which has V-A (vector-axial vector) coupling which only couples to left handed particles, hence the subscript L. A particle with right handed helicity has its spin axis aligned parallel to the direction of motion, and a particle with left handed helicity has its spin axis aligned anti-parallel to the direction of motion. The group is generated by an isotriplet of vector fields ${W_\mu}^i$ in weak isospin space. The U(1) group describes the electromagnetic interaction, which couples to both left and right handed fermions. It is generated by a single vector field B_μ in weak hyperspin space. The fields ${W_\mu}^1, {W_\mu}^2, {W_\mu}^3$ and B_μ do not correspond to the physical gauge bosons, but linear combinations of these fields do. The neutral electromagnetic and weak fields are mixed using a parameter θ_W, known as the weak mixing angle or the Weinberg angle. (We follow the notation and conventions of references [4] and [5].) Four physical gauge bosons are given by:

$$
\begin{aligned}
{W_\mu}^\pm &= \sqrt{\frac{1}{2}}({W_\mu}^1 \mp i{W_\mu}^2) \\
A_\mu &= B_\mu cos\theta_W + {W_\mu}^3 sin\theta_W \\
Z_\mu &= -B_\mu sin\theta_W + {W_\mu}^3 cos\theta_W
\end{aligned}
$$

The ${W_\mu}^\pm$ correspond to the charged massive $W^\pm$ gauge bosons which mediate the charged portion of the weak interaction. A_μ corresponds to the massless photon, γ, which mediates the electromagnetic interaction. Z_μ corresponds to the massive neutral Z^0 boson which mediates the neutral current portion of the weak interaction. The fact that the $W^\pm$ and Z^0 bosons have mass is due to a process known as spontaneous symmetry breaking. The "Higgs mechanism" that accomplishes this includes a scalar Higgs field and predicts the existence of one or more massive Higgs gauge scalars which have not been observed. The masses of the $W^\pm$ and Z^0 are related by $M_W = M_Z cos\theta_W$. The weak mixing angle θ_W can also be expressed in terms of the gauge coupling constants g and $g\prime$, by $tan\ \theta_W = \frac{g\prime}{g}$. The coupling constants g and $g\prime$ are used to describe how fermions couple to the gauge bosons and are related to θ_W by

$$g\ sin\theta_W = g\prime\ cos\theta_W = e,$$

where e is the charge of the electron.

2.3 Fermions

The gauge bosons mediating the electroweak forces between fermions were described in the preceding section. All matter is composed of fermions, which fall into two categories, quarks and leptons. There are six types of each, the quarks are designated by u (up), d (down), c (charm), s (strange), t (top), b (bottom). The leptons are designated by e (electron), ν_e (electron neutrino), μ (muon), ν_μ (muon neutrino), τ (tau), and ν_τ (tau neutrino). The quarks and leptons are grouped into three generations as follows, where their charge Q is also shown:

$$\begin{array}{lcccc} \text{Quarks} & \begin{pmatrix} u \\ d \end{pmatrix} & \begin{pmatrix} c \\ s \end{pmatrix} & \begin{pmatrix} t \\ b \end{pmatrix} & \begin{array}{c} Q = +2/3 \\ Q = -1/3 \end{array} \\ \text{Leptons} & \begin{pmatrix} \nu_e \\ e \end{pmatrix} & \begin{pmatrix} \nu_\mu \\ \mu \end{pmatrix} & \begin{pmatrix} \nu_\tau \\ \tau \end{pmatrix} & \begin{array}{c} Q = 0 \\ Q = -1 \end{array} \end{array}$$

The helicity states, or handedness, of the quarks and leptons are also significant in their coupling to the gauge bosons. The $W^\pm$ bosons couple only to left handed fermions, so the weak charged current involves only left handed fermions. The electromagnetic force is not sensitive to handedness so the photon couples to right and left handed fermions with equal strength. The Z^0 gauge bosons, couple to both left and right handed fermions, but with different strength. The left handed states of the quarks and leptons exist as weak isodoublets:

$$\begin{pmatrix} u \\ d \end{pmatrix}_L \begin{pmatrix} c \\ s \end{pmatrix}_L \begin{pmatrix} t \\ b \end{pmatrix}_L$$
$$\begin{pmatrix} \nu_e \\ e \end{pmatrix}_L \begin{pmatrix} \nu_\mu \\ \mu \end{pmatrix}_L \begin{pmatrix} \nu_\tau \\ \tau \end{pmatrix}_L$$

and the right handed states are isosinglets:

$$u_R, d_R \quad c_R, s_R \quad t_R, b_R$$
$$e_R \quad \mu_R \quad \tau_R$$

All the quarks and leptons have an antiparticle with the same mass and opposite charge and helicity. Note that right handed neutrinos or left handed antineutrinos do not exist. Leptons have integer charge and are fundamental particles that can be observed in a free state. The charged leptons interact via the electromagnetic and weak interactions, while the neutrinos and their antiparticles interact with other particles only via the weak force. Quarks, with fractional charge, are never observed in a free state. They are bound in either a quark anti-quark pair to form mesons, such as a pion, or in three quark states to form baryons, such as a proton. Quarks are subject to strong, weak and electromagnetic interactions. The τ neutrino is the only fermion which has not yet been observed directly. The top quark has long been assumed to exist, and was recently observed in the CDF [6] and D0 [7] experiments at Fermilab. Spontaneous symmetry breaking is responsible for the fermion masses, as well as for the massive gauge bosons.

2.4 Z^0 Production and Decay at e^+e^- Colliders

An e^+e^- collider provides an excellent environment for a high precision study of the Z^0 and its decays. The Standard Model predicts two tree level processes (no closed loop radiative corrections) for $e^+e^- \rightarrow f\overline{f}$, where $f\overline{f}$ is any fermion anti-fermion pair. (The special case where the $f\overline{f}$ final state is e^+e^- has two additional diagrams, which will be discussed in the next section). The Feynmann diagrams representing these two processes are shown in Figure 1. The SLC and the LEP collider in Geneva, Switzerland are e^+e^- colliders designed to operate at the Z^0 resonance, that is, the energy of each beam is equal to half the Z^0 mass. At the Z^0 resonance, except for small angle e^+e^- final states, the contribution of the photon process shown above is very small compared to the Z^0 process. Since the Z^0 is heavier than any of the fermions except for the top quark, fermion pairs are produced, providing for numerous detailed measurements of cross sections, partial widths, coupling constants, asymmetries, etc. to test the Standard Model in detail, and to search for indications of new physics beyond the Standard Model. The SLC operates with a polarized electron beam, which allows additional measurements to

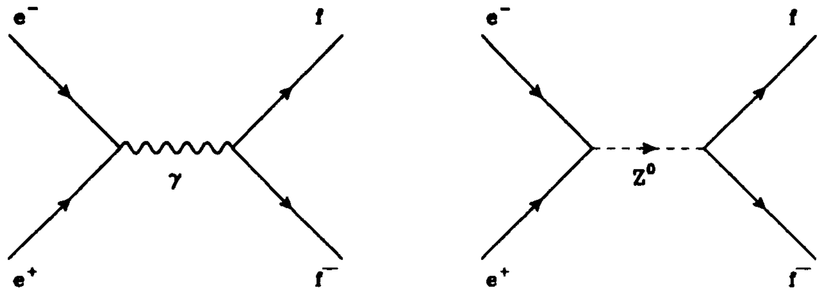

Figure 1: Tree level Feynmann diagrams for e^+e^- collisions at the Z^0 resonance.

be made that are sensitive to helicity states. The most significant of these is the measurement of the left-right asymmetry, A_{LR}, which is the difference in Z^0 boson production rates when left and right handed electrons are used, divided by the sum of the two rates. The measurement of A_{LR} provides for a very sensitive measurement of $\sin^2\theta_W$, a key parameter of the Standard Model.

2.5 Introduction to Bhabha Scattering

The Bhabha scattering process, $e^+e^- \rightarrow e^+e^-$, is named for Homi Bhabha, who first studied the process in 1935 [8]. At energies at or near the Z^0 resonance, Bhabha scattering proceeds via Z^0 or photon exchange, with interference between the Z^0 and photon also contributing, particularly at large angles. At small angles the pure QED photon exchange process dominates the interactions, which can be calculated to high precision. The small angle Bhabhas can therefore be used to measure the luminosity.

Precision calculation of the Bhabha cross section requires that radiative corrections be taken into account to correctly compare data with theory, since tree level contributions do not adequately describe the process at the energy of the Z^0. To directly compare data with theory it is important to have a Monte Carlo that not only calculates the cross section but which serves as a full scale event generator. The Monte Carlo events are run through a detailed shower simulation. Cuts similar to those applied to the data sample can then be directly applied to the Monte Carlo events and the cross section determined for arbitrary experimental cuts. Since radiative corrections are so important for correctly calculating a total cross section necessary for luminosity determination, a direct comparison of radiative events with the Monte Carlo predictions is of interest to check how well the Monte Carlo takes the radiative corrections into account.

2.6 Lowest Order Contributions to Bhabha Scattering

The lowest order, Born level contribution to Bhabha scattering consists of four terms, represented by their Feynmann diagrams in Figure 2. The dominant processes are a) and b), while the processes corresponding to c) and d) are suppressed near the Z^0 at low angles by the s and t dependences of the respective γ and Z^0 propagators. The process shown in a) is pure QED t channel photon exchange. This process is unique to Bhabha scattering and is the dominant process at low angles where the QED cross section can be calculated accurately. Small angle Bhabhas can then be used to measure the luminosity. The process shown in b) is s channel annihilation via the Z^0. This process also occurs in the other fermion final states consisting of two leptons. Each diagram represents a contribution of one term to the Born level cross section, with the interference between each pair of diagrams contributing another six terms, for a total of ten terms. In this dissertation only the small angle Bhabhas are studied, and the Born level cross section containing only the photon exchange terms is given by:

$$d\sigma/d\Omega = \frac{\alpha^2}{s}\left(\frac{3+cos^2\theta}{1-cos\theta}\right)^2 \tag{1}$$

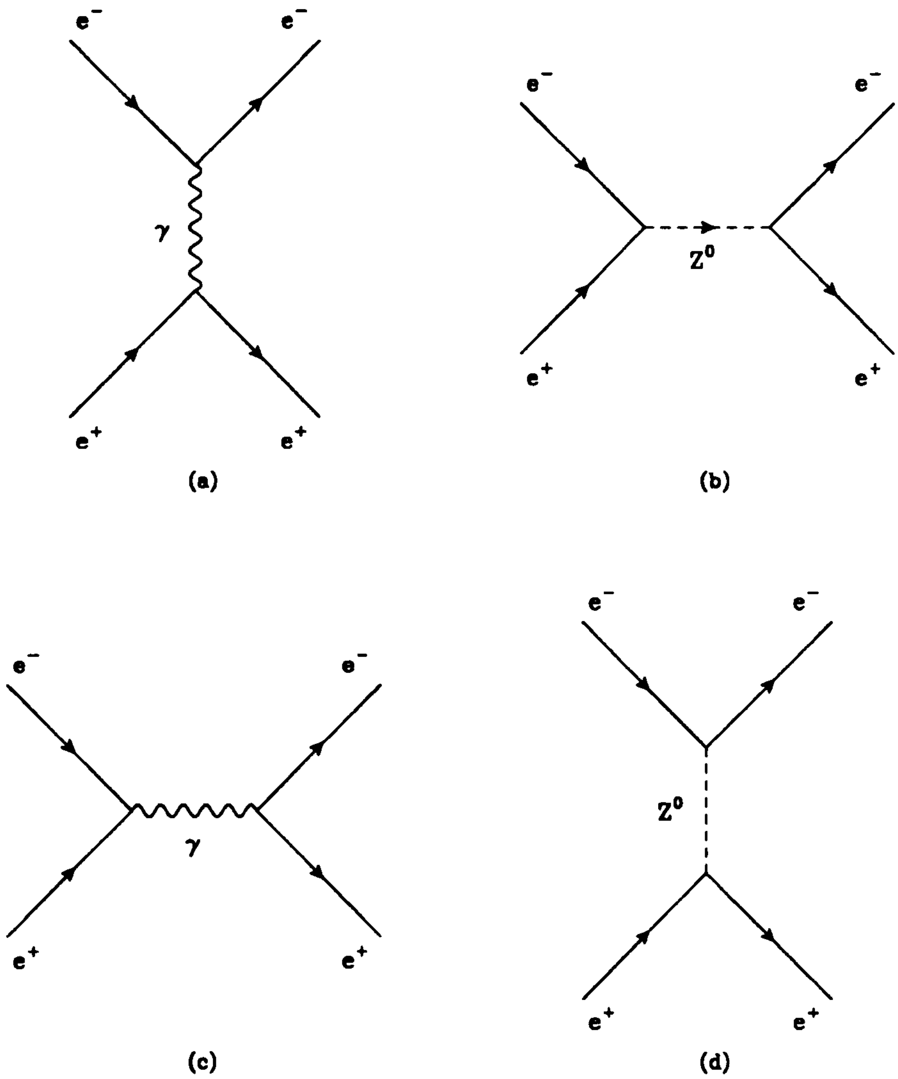

Figure 2: Born level contributions to Bhabha scattering.

where α is the fine structure constant, s is the square of the center of mass energy, θ and ϕ are the polar and azimuthal scattering angles, and $d\Omega$ is the solid angle element $\sin\theta d\theta d\phi$.

2.7 Radiative Corrections

At center of mass energies at or near the Z^0 resonance, radiative corrections play a more significant role in low angle Bhabha scattering than at the lower energy experiments at PEP or PETRA. This is primarily because of the higher precision of the LEP/SLC experiments, since the amount of low angle Bremsstrahlung radiation increases only as the logarithm of the beam energy. The emission of photons in the initial state reduces the effective center of mass energy, and may also change the angular profile of the outgoing electrons and positrons, since the available energy from the beam is reduced in a non-symmetric way. The magnitude of the effect is dependent on the experimental cuts. For example, a cut requiring the outgoing electron and positron to be approximately collinear will eliminate some radiative events. The effect of radiative corrections should be taken into account to as high an order as possible when calculating the total cross section or when studying the characteristics of the radiative Bhabha events. Feynmann diagrams representing the lowest order radiative corrections are shown in Figure 3. These are the order α QED corrections to the photon exchange diagram. The size of these effects is $\approx$ 10% at low angles, ($\approx$ 50 mrad), in the Z^0 resonance regime for the typical SLC/LEP type luminosity acceptance.

We used the BHLUMI 2.01 [9] Bhabha generator to obtain the Monte Carlo results presented in this dissertation. This program is designed to be used for scattering angles less than about 10°. It is based on Yennie-Frautschi-Suura (YFS) $O(\alpha)$ exponentiation [10] of the radiative correction terms. Exponentiation is a method of summing up to infinite order the contribution for real and virtual radiated photons [9]. The technique allows calculation of the cancellation of the

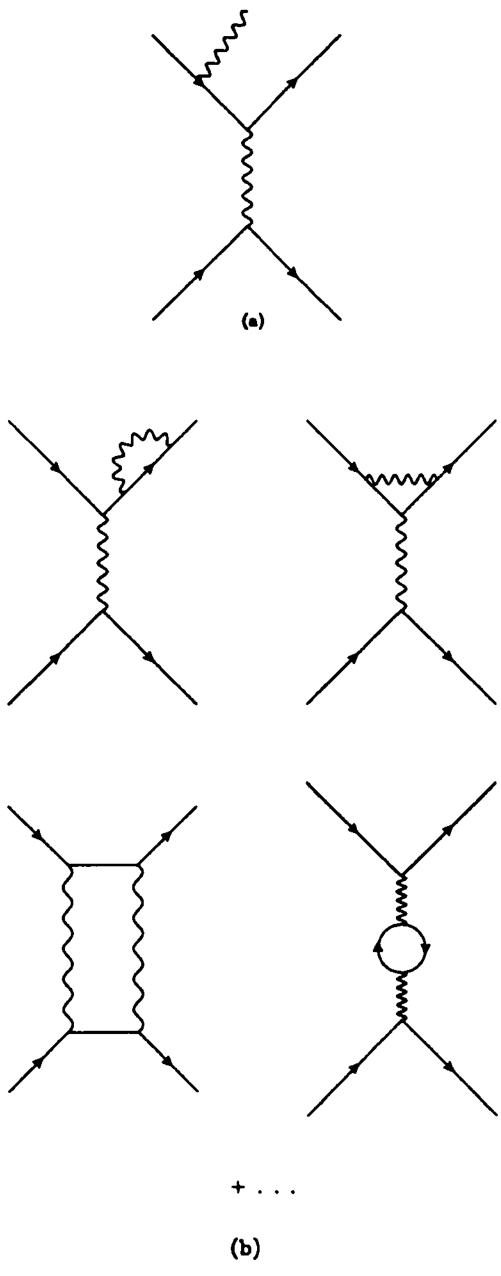

Figure 3: Lowest order radiative corrections, where (a) shows real emission, and (b) shows virtual corrections.

infrared divergent terms in the cross section to all orders in α. The infrared contributions are correctly summed up to infinite order, and the remaining non-infrared parts are calculated perturbatively order by order [9]. This technique can accommodate an arbitrary number of real photons. A complete description of the program BHLUMI 2.01 is given in reference [9] and the earliest version of this program is described in [11]. Further references of interest are [12, 13, 14]. Historically, the first Bhabha scattering Monte Carlo was the generator OLDBAB [15], developed for use at PEP and PETRA, where the center of mass energy was ≈ 30 GeV. OLDBAB is an $O(\alpha)$ Monte Carlo generator for $e^+e^- \rightarrow e^+e^-(\gamma)$, with the generation of one photon possible. OLDBAB has an accuracy of $\approx 2\%$, which was adequate for the detectors of that era. OLDBAB was updated to BABAMC [16] for use at LEP/SLC and it can in principle achieve an accuracy of 1-1.5% for the LEP/SLC luminosity measurements. It is still an $O(\alpha)$ generator with at most one real photon per event. With the advent of high precision luminosity monitors at LEP and SLC, capable of precisions below 1%, an infinite order Monte Carlo was needed, in which an arbitrary number of photons are produced on an event by event basis, so that the Monte Carlo events could then simulate Bhabha events observed in luminosity monitors with a precision below 1%. The work done in references [11, 12, 13, 14] has resulted in the Monte Carlo BHLUMI, which is now the state of the art calculation of the Bhabha scattering process at low angles, in the acceptance region of the SLC and LEP luminosity monitors. In this dissertation we compare in detail BHLUMI 2.01 and data from the SLD luminosity monitor.

Chapter 3

SLC and SLD

3.1 Introduction

The data for this dissertation were taken with the SLD detector using the Stanford Linear Collider (SLC) at the Stanford Linear Accelerator Center (SLAC). The SLC was designed to collide electron and positron beams at a center of mass energy near the Z^0 boson resonance, around 91 GeV. For the first few years of operation, beginning with the first beams delivered to the interaction point in 1988, SLC collided unpolarized electrons and positrons, but the capability for using polarized electron beams was included in the initial design [17]. The first physics data from SLC was produced in 1989 with the upgraded Mark II [18] detector recording about 700 Z^0 bosons in 1989 and 1990 [19]. In 1991 the SLD detector replaced Mark II at the interaction point and detected about 400 Z^0's during a 3 month engineering run. The 1992 run began with an unpolarized electron beam, and about 1000 Z^0's were collected before a shutdown in April of 1992 to install a polarized electron source. SLC resumed production of Z^0's in May of 1992 with a polarized electron beam, and became the first collider in the world (and to date the only such collider) to produce Z^0 bosons with a polarized electron beam. The 1992 run yielded approximately 10,000 Z^0's with an average electron polarization

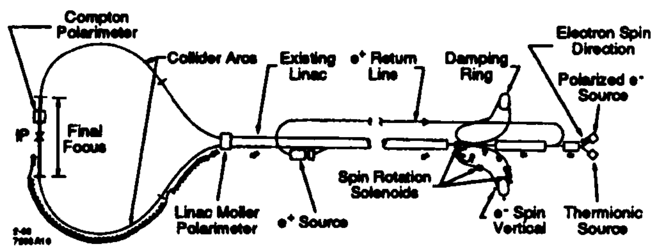

Figure 4: A simplified schematic of the SLC.

of 22%. In 1993 an improved polarized electron source was installed and about 50,000 Z^0's were recorded in the SLD detector betwen March and August of 1993, with average electron polarization of 63%. A brief description of the operation of the SLC with the polarized source, the measurement of the polarization, and a description of the SLD detector are given in the following sections.

3.2 SLC

3.2.1 The Collider

A simplified diagram of the layout of SLC [20] is shown in Figure 4. Polarized electrons are produced in bunches of about 6×10^{10} when a polarized laser beam from a Yag pumped Ti:Sapphire laser strikes the photocathode on the electron gun. Two bunches of electrons are produced in each 120 Hz machine cycle. The electron bunches are accelerated to 1.19 GeV and injected into the North Damping Ring, where they are "cooled" by synchrotron radiation damping. At the same time, a positron bunch produced from the positron source during the previous machine cycle is being similarly cooled in the South Damping Ring. After damping, the positron bunch followed by the two electron bunches are extracted from the two damping rings and are accelerated down the 3 km long linear collider. The positron bunch and the first electron bunch are accelerated to about 46.6 GeV and collide at the interaction point. The second electron bunch is diverted from the linac approximately 2/3 of the way down and then transported to the positron production target. When the tungsten target is struck by the electrons, an electromagnetic shower results and electrons and positrons are produced. The positrons are separated and returned to the beginning of the linac where they are accelerated to 1.19 GeV and then stored in the South Damping Ring to be ready to join the next pair of electron bunches to be accelerated down the linac [21, 22].

When the 46.6 GeV beams of electrons and positrons reach the end of the linac, they are split by a dipole magnet and are transported through the arcs toward the interaction point at the collider experimental hall. The beams lose a small amount of energy by synchrotron radiation as they travel through the arcs. To achieve as high a luminosity as possible, the beams are strongly focused to a very small spot size when they collide. The Final Focus system consists of quadrupole, sextupole, and superconducting quadrupole magnets on each side of the interaction point. During 1993 "flat beam" operation, bunch sizes of 2.1 microns horizontally and 0.8 microns vertically were achieved [23]. Particles that do not interact at the interaction point continue on to beam dumps. Their energies are measured by energy spectrometers just before the beam dump, and the polarization of the electron beam is measured by the Compton polarimeter 33 meters away from the e^+e^- interaction point. The Compton polarimeter is described in section 3.3.2.

3.2.2 Polarized Electron Source

As mentioned in the previous section, longitudinally polarized electrons are produced by photoemission when a Yag pumped Ti-Sapphire laser [24] is used to illuminate the GaAs target. A bulk GaAs photocathode was used as the polarized electron source in the 1992 run, and a strained GaAs source was used for the 1993 run [25].

The laser beam is circularly polarized and for 1992 the wavelength of the laser beam was $\lambda = 715$ nanometers [22]. In 1993 the laser operated at $\lambda = 850$ nanometers for the first 20% of the run [26], and at 865 nanometers for the rest of the run.

The laser photons have an energy slightly above the band gap energy in GaAs, and induce a transition of electrons in the GaAs from the $P_{3/2}$ valence band to the $S_{1/2}$ conduction band. From conservation of angular momentum and selection rules for transitions between bands, right handed circularly polarized light will preferentially cause the electron promoted to the $S_{1/2}$ band to be preferentially right handed with a ratio of 3:1, and left handed circularly polarized light will preferentially cause production of left handed electrons. The circular polarization state of each laser pulse is chosen randomly. The maximum theoretical polarization of bulk GaAs is 50% [27]. The actual polarization achieved for 1992 was 28-29% at the source with an average polarization at the interaction point of 22.4 $\pm$ .7 %. Strained GaAs cathodes have been shown to produce polarizations greater than 50%, since the strained lattice causes energy level splitting of the m_j=3/2 and m_j=1/2 levels of the $P_{3/2}$ valence state and removes their degeneracy. In theory a polarization of 100% is possible [25, 27, 28]. The strained GaAs cathode used in the 1993 run produced 80% polarization at the source [27]. The luminosity weighted average polarization at the interaction point (IP) was 63.0 $\pm$ 1.1% [29]. The full polarization from the source is not preserved at the IP due to depolarizing effects, e.g. the energy spread of the beam and spin transport in the arcs.

3.3 SLD

3.3.1 Introduction

The SLD detector is shown in Figure 5. Charged particle tracking is provided by a CCD vertex detector and high precision drift chamber operating inside a 0.6 Tesla magnetic field. Particle identification is provided by a Cherenkov ring imaging detector. A liquid argon calorimeter with both electromagnetic and hadronic sections operates inside the magnetic field for total energy measurement. A warm iron calorimeter provides additional hadronic calorimetry for energy leaking from the liquid argon calorimeter as well as serving as a muon tracker. A silicon-tungsten

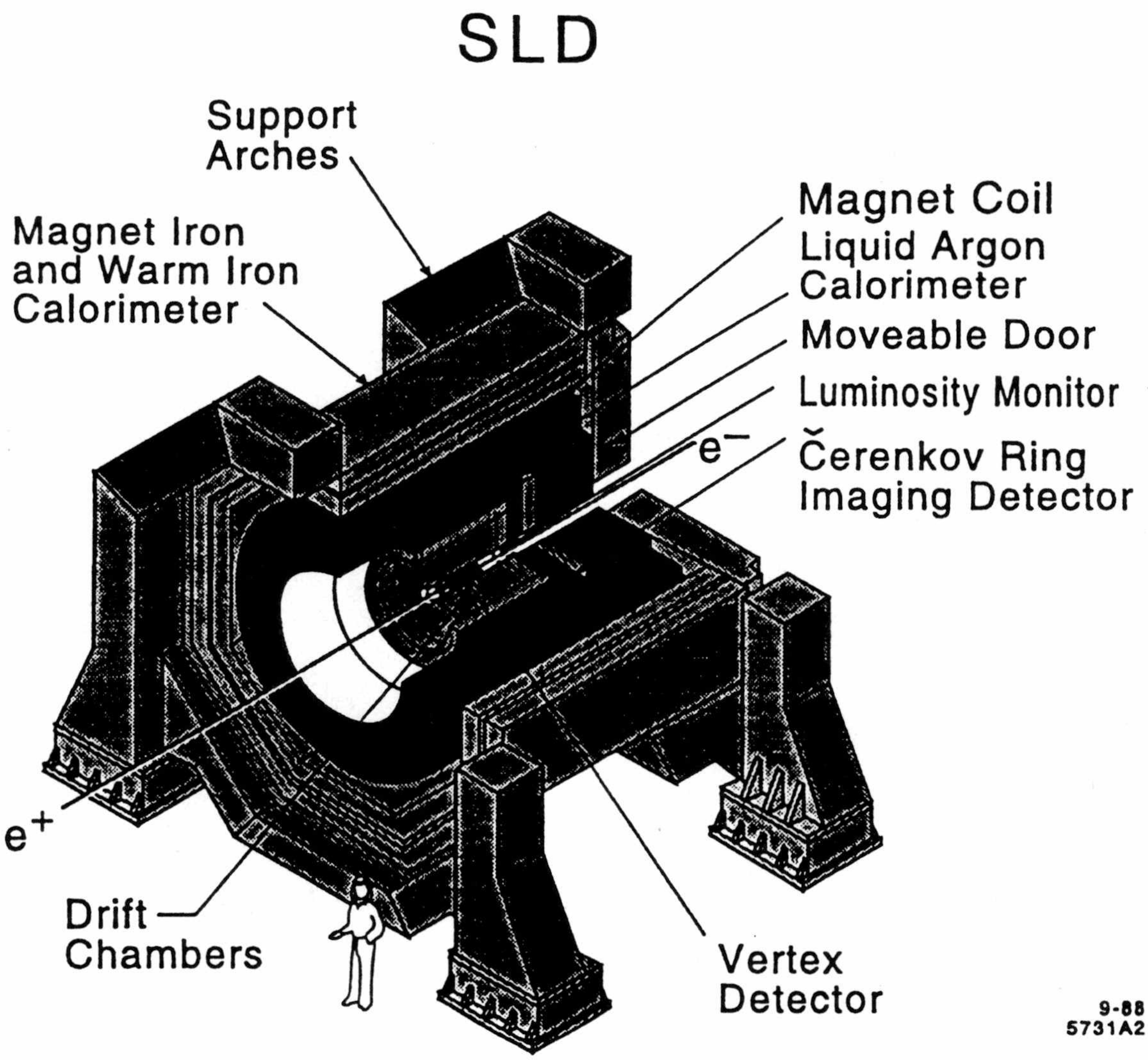

Figure 5: Isometric drawing of SLD detector.

luminosity monitor and medium angle silicon calorimeter complete the electromagnetic calorimetry at small angles. All the systems except for the vertex detector, luminosity monitor, and medium angle silicon calorimeter have endcap components as well as barrel components, although these are not shown in Figure 5. Figure 6 shows a quadrant view of all components, both barrel and endcap. The following sections describe the components of the SLD detector.

3.3.2 Polarimetry

The polarization of the electron beam is measured with a Compton scattering polarimeter [30], located 33 meters downstream from the SLC interaction point. Figure 7 shows a schematic of the Compton polarimeter system. After the electron beam from SLC has passed through the IP, it collides with a circularly polarized photon beam of 2.33 eV from a frequency doubled Nd:YAG laser. The asymmetry in the cross section for Compton scattering for parallel vs. anti-parallel combinations of helicities of the electrons and photons beams is exploited to measure the polarization of the electron beam. The differential cross section for Compton scattering of longitudinally polarized electrons and circularly polarized photons is given by [31]

$$d\sigma_p/dE_s = d\sigma_u/dE_s[1 + P_\gamma P_e A(E_s)]$$

where σ_p is the polarized cross section, E_s is the energy of the scattered electron, σ_u is the unpolarized Compton scattering cross section, P_γ is the photon polarization, P_e is the longitudinal polarization of the electron and $A(E_s)$ is the theoretical Compton asymmetry function at the energy E_s for photon electron spins parallel vs. anti-parallel. The counting rate for the parallel and anti-parallel combinations is measured in the detector, which gives the measured asymmetry, which is then related to the electron polarization by:

$$P_e = A_{meas}/P_\gamma < A > .$$

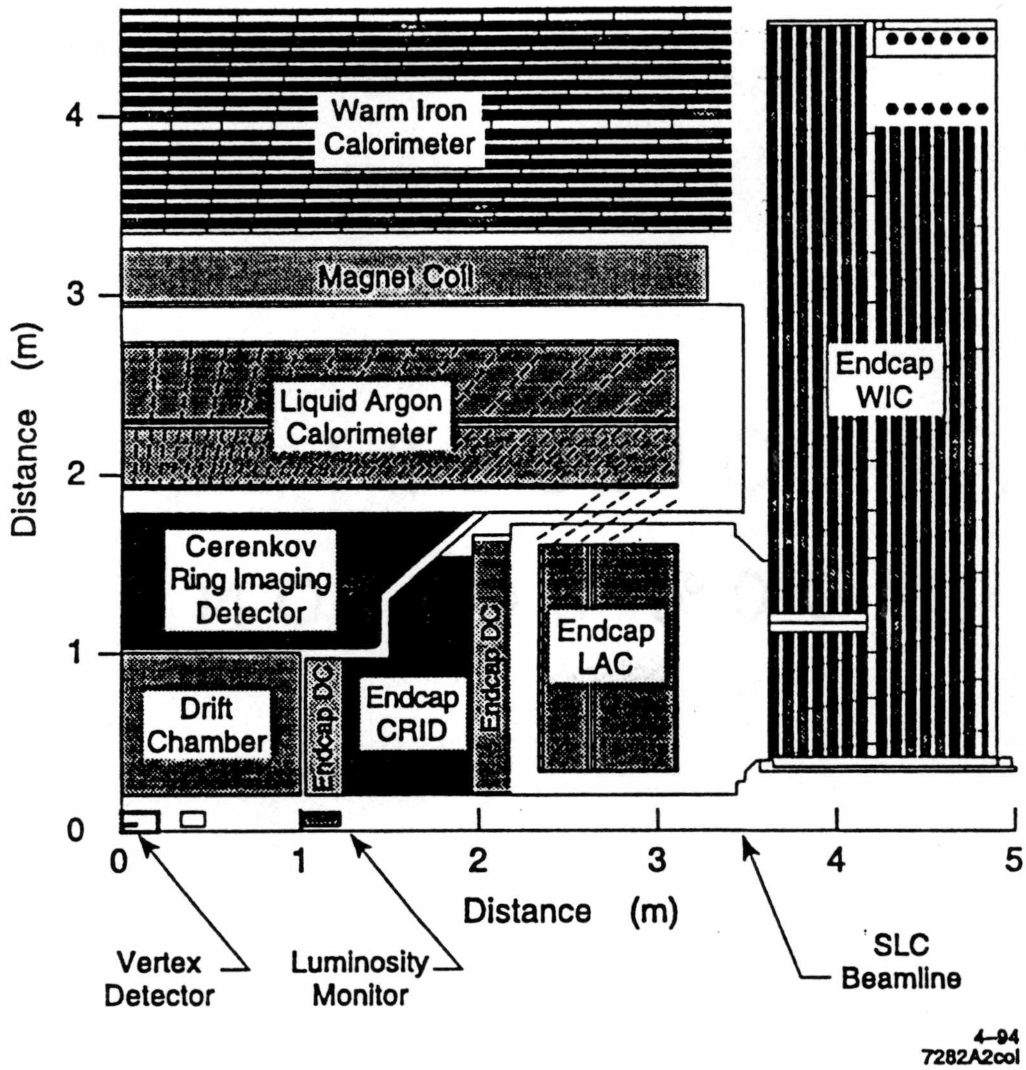

Figure 6: Quadrant of the SLD detector.

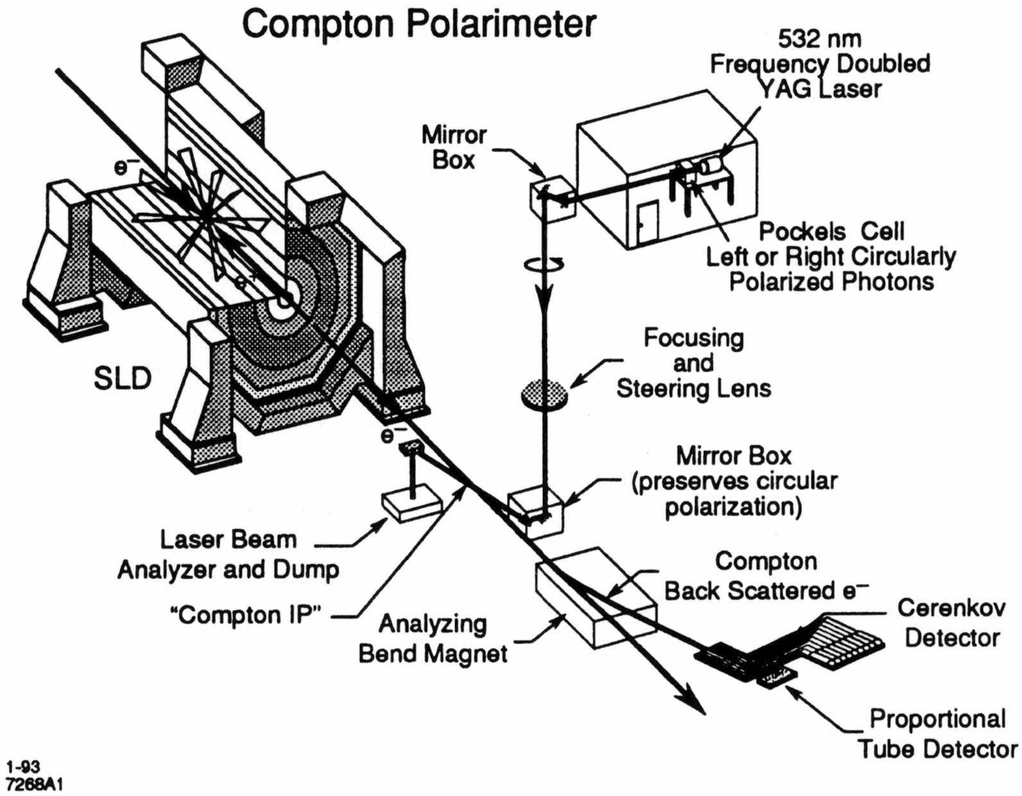

Figure 7: SLD Compton Polarimeter.

The analyzing power of the detector channel used, $< A >$, is the average Compton asymmetry for the energy interval subtended by the detector channel used to measure the rate asymmetry (determined theoretically), and P_γ is the measured polarization of the laser beam [32]. After the electron and photon beams have collided, the scattered and unscattered electrons remain together until they pass through a pair of dipole magnets. The Compton scattered electrons are separated horizontally and exit the vacuum system through a thin window, while the unscattered electrons are transported to a beam dump. Scattered electrons in the momentum range of 17 to 30 GeV/c are detected and momentum analyzed in multichannel Cherenkov and proportional tube detectors located downstream of the effective bend center of the dipole magnet pair. The kinematic limit for Compton scattering occurs at E_s = 17.4 GeV, corresponding to a scattering angle of 180° in the electron rest frame. The cross section asymmetry is zero at E_s = 25.2 GeV and these two points are used to calibrate the energy scale of the polarimeter. The counting rates for the parallel and antiparallel beam helicities are measured in each detector channel and the polarization asymmetry is determined [31, 22]. P_γ is measured and was 93 ± 2% for the 1992 run, 97 ± 2% for the first 26.9% of the 1993 run and 99.2 ± .6% for the remaining 73.1% of the 1993 run [29]. The laser polarization for the last 73.1% of the 1993 run was maintained by continuously monitoring and correcting phase shifts in the laser transport system. Data is taken continually with the polarimeter, with individual runs being approximately 3 minutes long. The electron polarization P_e is determined for each run using the measured value of P_γ, and the measured asymmetry in the counting rate. The measured electron beam polarization is typically 61-64% for 1993 and the luminosity weighted average polarization was 63.0 ± 1.1 % [29].

3.3.3 Tracking

Vertex Detector

The SLD vertex detector [33] (VXD) uses charged coupled devices (CCDs) to provide excellent three dimensional track resolution close to the interaction point. The small beampipe radius (25 mm), the low repetition rate of SLC, and the well defined interaction point allow this device to be used to distinguish secondary vertex tracks produced by the decay in flight of short lived heavy flavor hadrons or tau leptons [34]. The VXD consists of 480 CCDs in a configuration of four concentric cylinders. Figure 8 shows a drawing of the vertex detector. Each CCD

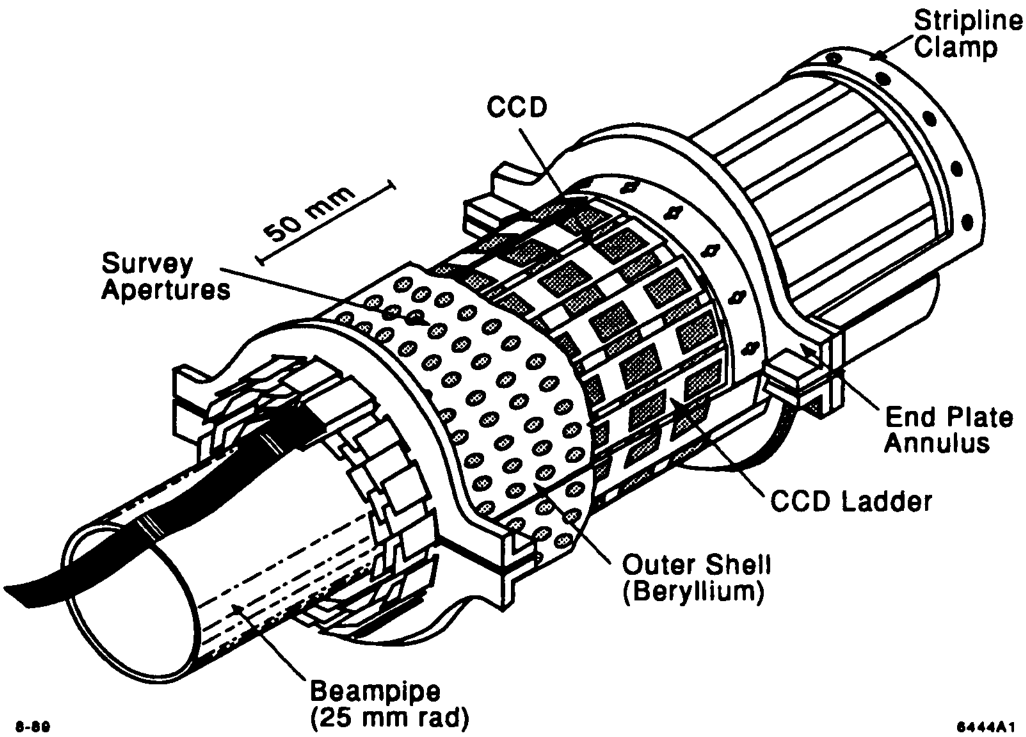

Figure 8: SLD Vertex Detector.

has $\approx 400 \times 600$ pixels. Each pixel is 22 μm $\times 22$ μm, and the total active area of a CCD is 8.5×12.7 mm^2. Spatial resolutions of ≈ 5 μm in the $R\phi$ and z coordinates have been measured, leading to impact parameter resolutions of 11 μm in $R\phi$ and 38 μm in Rz for high momentum tracks [35].

Drift Chambers

The Central Drift Chamber (CDC) [36] is a cylindrically shaped detector that provides position and momentum information for charged particles. It operates in a uniform solenoidal magnetic field of 0.6 Tesla and covers 80% of the solid angle of SLD. It is 2 meters long, with an inner radius of 0.2 m and an outer radius of 1.0 m. Its volume is filled with a gas mixture of 75% CO_2, 21% Ar, 4% isobutane and 0.2% water, with 80 layers of sense wires arranged in 10 superlayers of 8 wires each. Four of the superlayers have the wires strung axially, parallel to the beamline, and the other six make a 41 mrad stereo angle with respect to the beam axis. The superlayers consist of independent cells, with each cell containing high voltage wires to create a uniform electric field, sense wires for detecting charged particles, and field shaping wires. The structure of the cells is shown in Figure 9 and Figure 10 shows the arrangement of the superlayers. Charged particles traveling through the CDC ionize the gas, and the resulting electrons drift toward the sense wires. When they get close to the high electic field surrounding the sense wires an avalanche of electrons occurs. The resulting signals are read out on each end of a sense wire after being amplified by a preamplifier. Since both ends of the wires are read out, charge division assists in determining the z coordinate of the hit, and the fact that there are both axial and stereo layers provides additional position information. The gas mixture was chosen to be predominantly CO_2 because of its low drift velocity (7.9 μm/ns at the mean drift field), and also its low diffusion constant. The low drift velocity makes finer sampling of the pulse possible at a fixed electronics speed. The low diffusion constant reduces the contribution of diffusion to the resolution. These aspects of the gas along with the low mass of the chamber help minimize the drift distance mean error. An intrinsic drift resolution of 55-110 μm is measured in the region of uniform field [36].

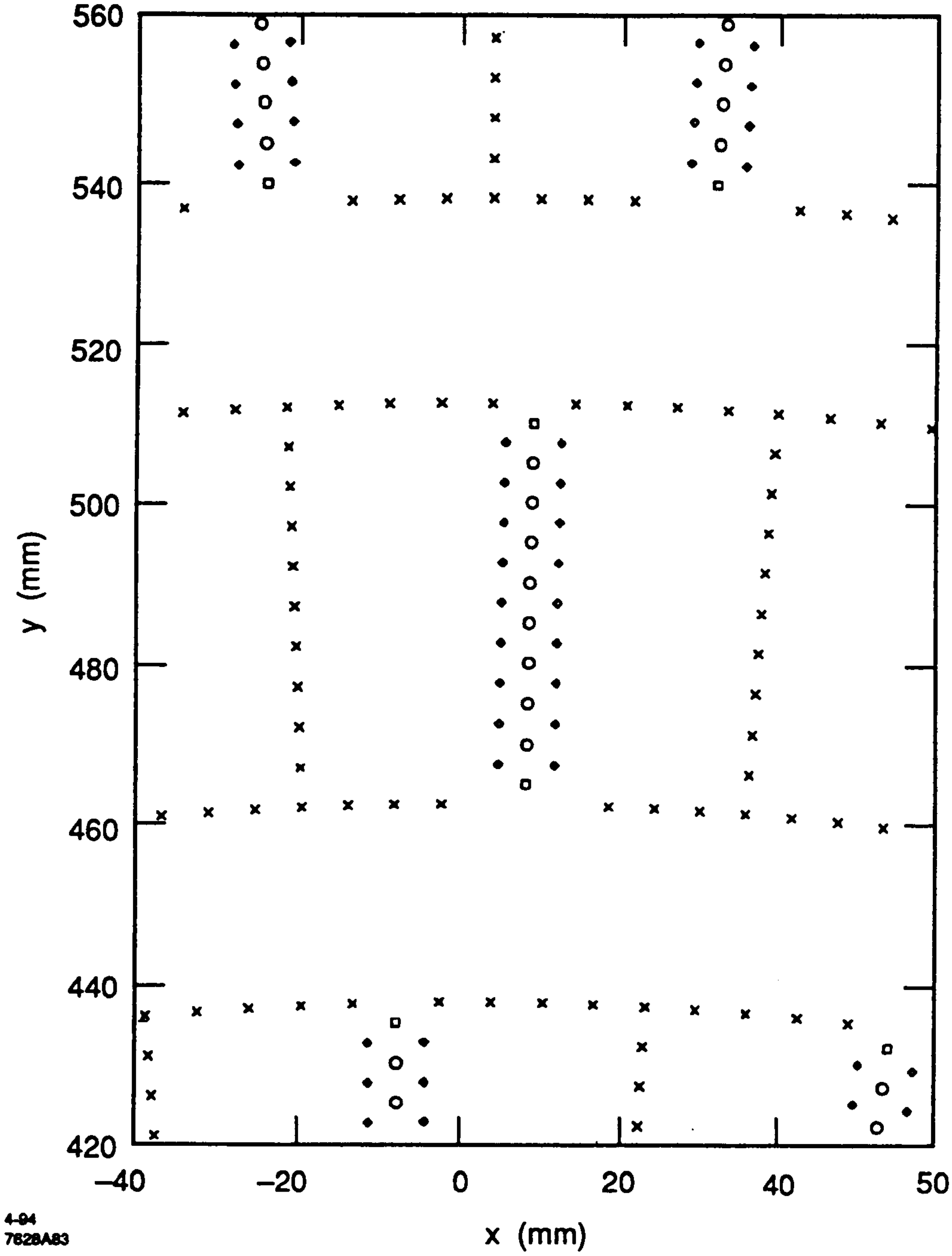

Figure 9: CDC cell structure. The circles represent sense wires, the diamonds are guard wires, and the crosses are field shaping wires.

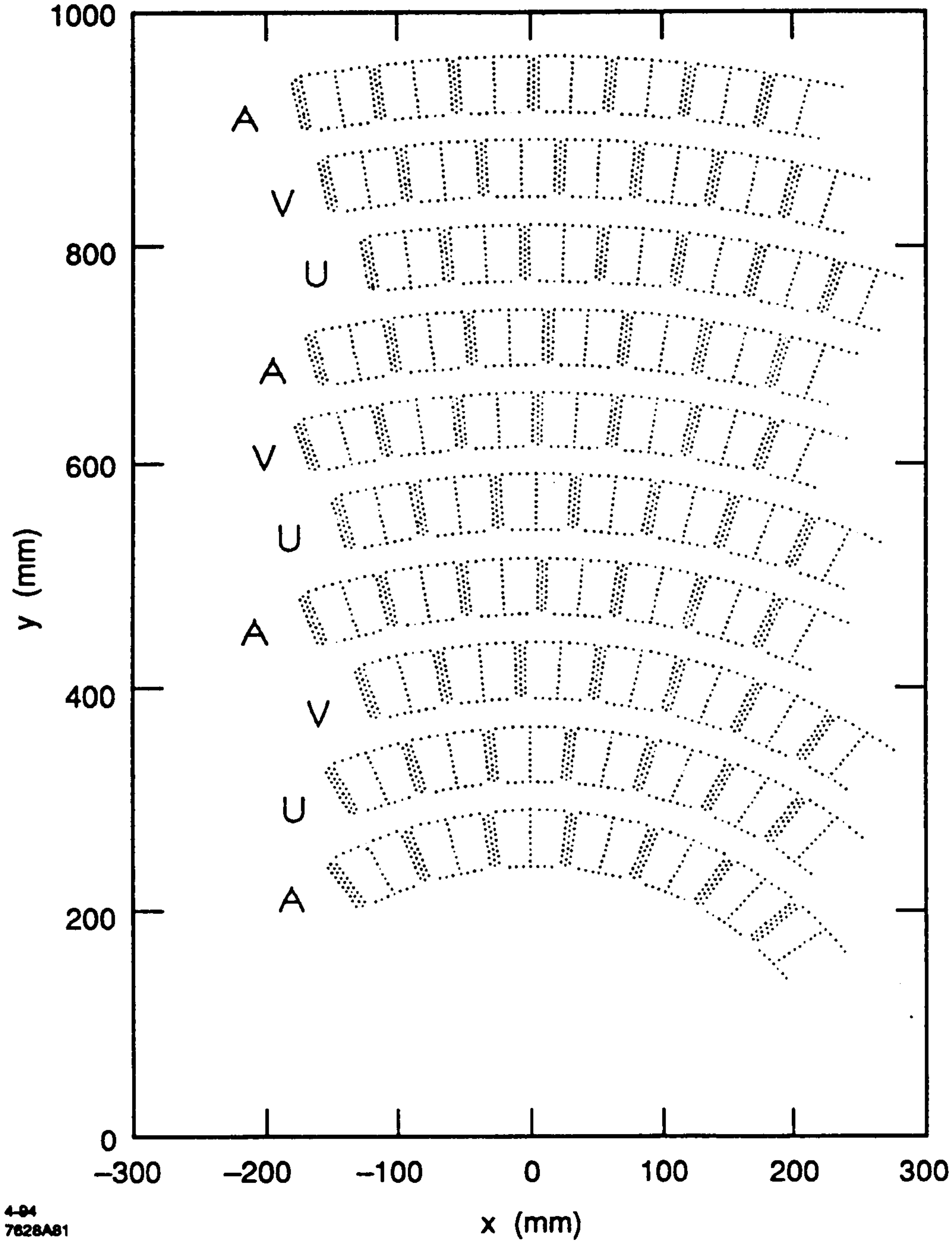

Figure 10: CDC superlayers. A denotes axial layers, U and V denote stereo layers.

3.3.4 Particle Identification

A Cherenkov Ring Imaging Detector (CRID) [37] is used for particle identification at SLD over a wide range of momenta. Its operation is based on the emission of Cherenkov light by a particle traveling in a medium at a speed faster than the speed of light in that medium. The angle at which light is emitted, known as the Cherenkov angle, is related to the velocity of the particle by $cos\theta = c/vn$, where v is the velocity of the charged particle, n is the refraction index of the material, and c is the speed of light. Measurement of the Cherenkov angle gives the velocity of the particle, and coupled with momentum information from the drift chamber, the mass of the particle and thus its identity can be determined. The CRID employs both liquid and gas radiators, so that $\pi/K/p$ separation is possible up to about 30 GeV/c and e/π separation up to about 6 GeV/c [38].

The barrel CRID is composed of 20 azimuthal sections. Each section contains two drift boxes, each of which are coupled to a multiwire proportional counter sensitive to single electrons [37, 39, 40]. Figure 11 shows a schematic of the barrel CRID components and Figure 12 shows a closer view of a drift box. When a charged particle enters the CRID, it first passes through the liquid radiator, a 1 cm thick layer of C_6F_{14} contained in a G-10 tray, with a quartz window. The Cherenkov light passes through the quartz window and into the drift box. As the charged particle continues on through the drift box and into the gas radiator, C_5F_{12}, additional Cherenkov photons are produced and are focused back into the drift box using two rows of spherical mirrors. The drift box is filled with a gas mixture that is about 1% TMAE (tetrakis[dimethylamino]ethylene), and a photon entering the drift box can ionize in the TMAE mixture and produce a single photoelectron. The photoelectrons drift in an electric field and are detected by a plane of 93 carbon sense fibers. The drift time, position of the carbon fiber, and charge division along the fiber give a set of coordinates so that a photon ring can be imaged. Thus the Cherenkov angle is measured and together with momentum information from the CDC, particle masses are determined. The barrel CRID pro-

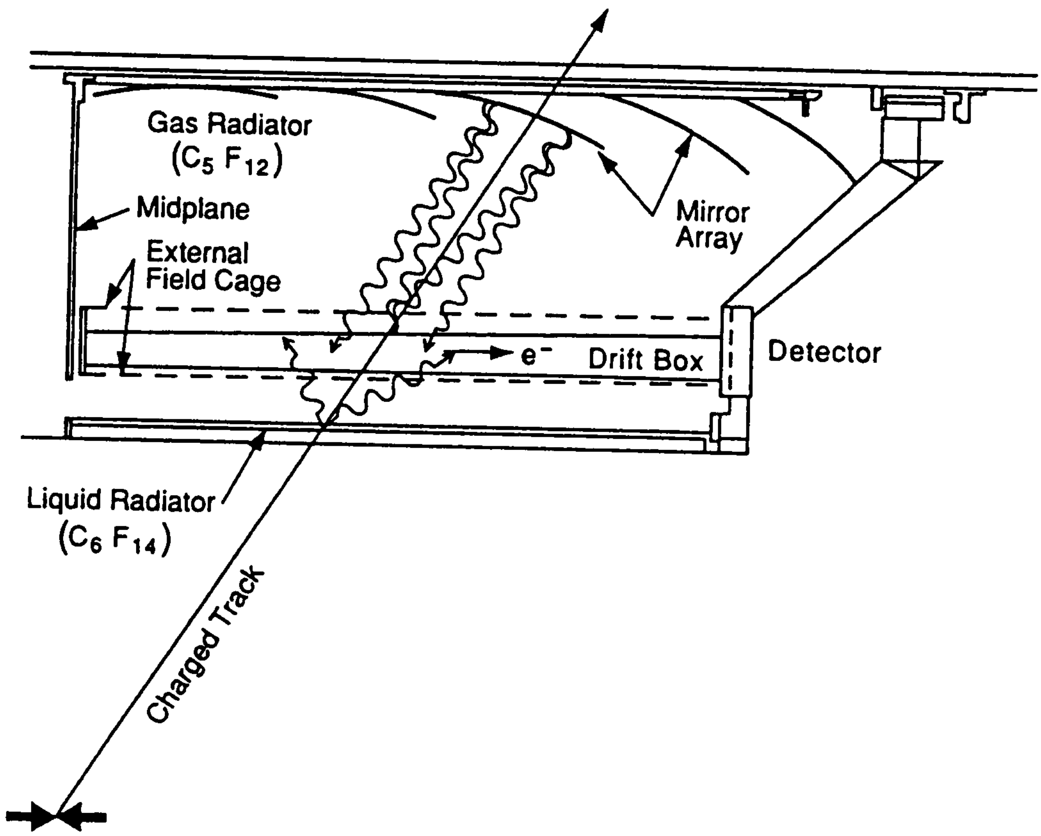

Figure 11: Schematic of barrel CRID components.

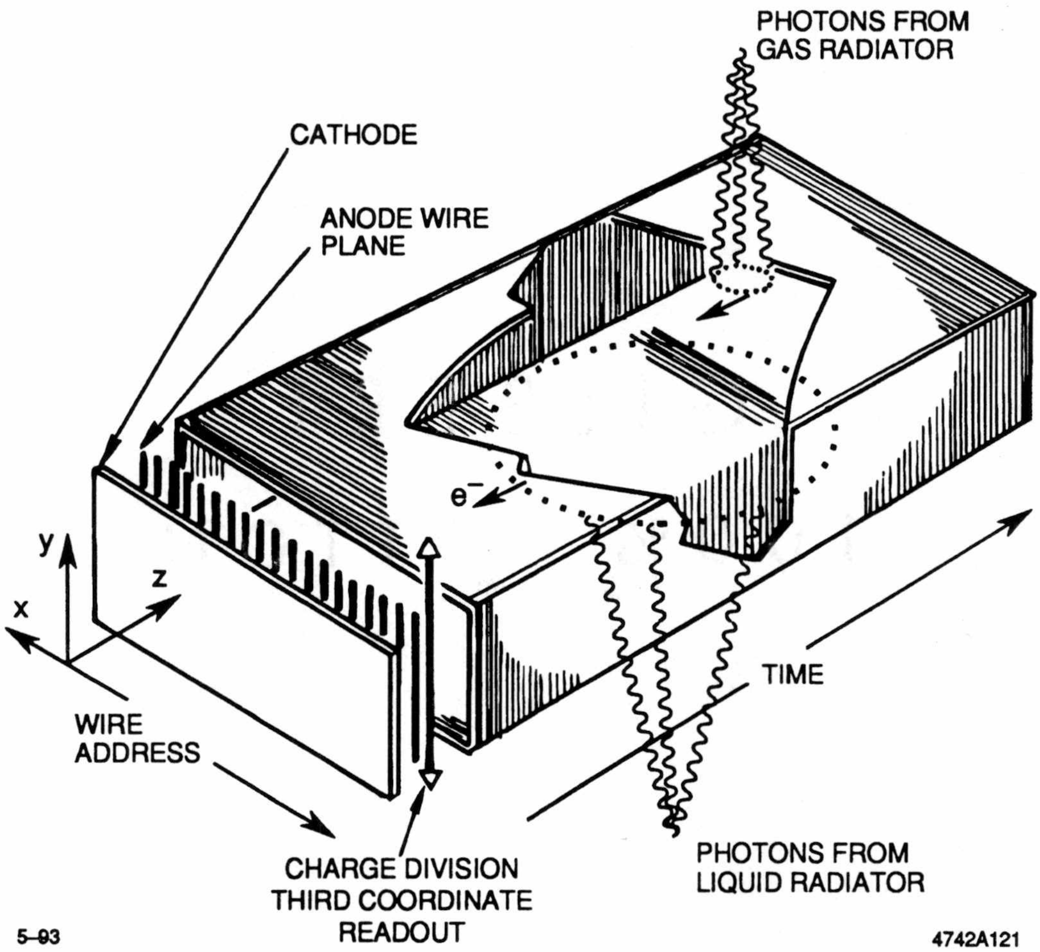

Figure 12: Barrel CRID drift box.

vides particle ID for over 70% of the solid angle. Endcap CRIDs complete the coverage.

3.3.5 Calorimetry

The calorimetry system for SLD consists of the Liquid Argon Calorimeter (LAC), the Warm Iron Calorimeter (WIC), the Luminosity Monitor Small Angle Tagger (LMSAT) and the Medium Angle Silicon Calorimeter (MASiC). Most electromagnetic and hadronic energy measurements are done with the LAC, which is composed of a barrel and two endcap sections. The endcap LAC covers the region from $8^\circ < \theta < 35^\circ$, and the barrel LAC $\theta > 33^\circ$, so the two together provide coverage for about 98% of the solid angle. The WIC measures hadronic energy that leaks out of the LAC. The LMSAT and MASiC provide electromagnetic coverage at smaller angles, $28\ \text{mrad} < \theta < 190\ \text{mrad}$. The LMSAT and MASiC are silicon tungsten sampling calorimeters and will be described in detail in Chapter 4.

Liquid Argon Calorimeter

The LAC [41, 42] is a liquid argon-lead sampling calorimeter. An ionization sampling calorimeter in general consists of alternating layers of an active material where ionization is detected, and a high Z absorber/radiator material where particles shower and lose energy. A liquid argon-lead calorimeter was chosen to provide uniform and stable energy response. It is radiation hard, can be operated close to the beamline and inside the 0.6 T magnetic field, and permits fine segmentation. It also provides partial equalization of response from electromagnetic and hadronic showers (compensation) [43, 44].

The barrel LAC is 6 m long with an inner radius of 1.8 m and an outer radius of 2.9 m. It contains 288 modules, each of which contain alternating planes of lead plates and lead tiles with the space in between filled with liquid argon. The lead plates and tiles are 2 mm thick in the electromagnetic (EM) section and 6 mm in the hadronic (HAD) section and the liquid argon gap in each is 2.75 mm.

The lead plates are held at ground and the lead tiles are held at -2000 Volts and serve as the charge collecting electrodes. The tiles are sized to form projective towers as successive layers are ganged together. The EM section of the barrel is divided into 192 azimuthal towers, each $\approx$ 33 mrad wide, 34 polar sections on each side of the midpoint, and two radial sections, EM1 (6 radiation lengths) and EM2 (15 radiation lengths). The HAD section towers have half the number of polar and azimuthal divisions. The HAD section is also divided into two sections radially, HAD1 (one absorption length) and HAD2 (one absorption length). Figure 13 shows LAC barrel EM and HAD modules, and Figure 14 shows plate and tile detail of a LAC barrel HAD module.

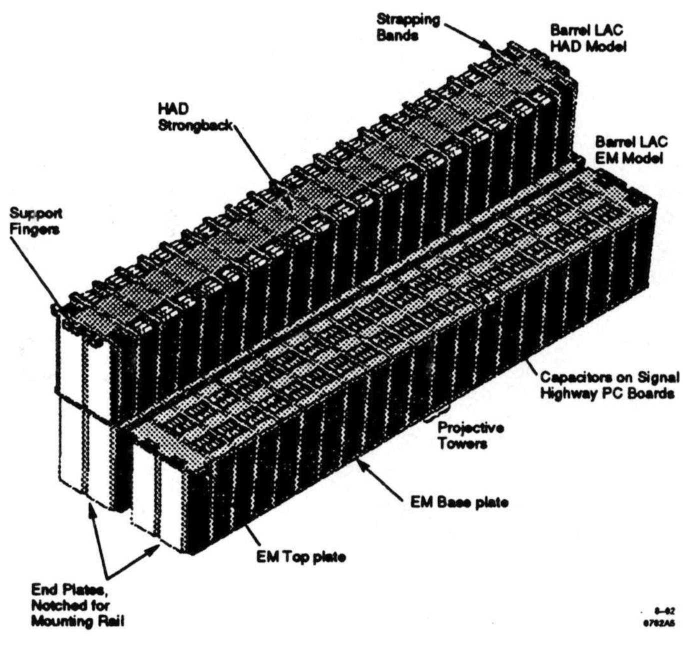

Figure 13: LAC Barrel EM and HAD modules.

The endcap LAC consists of 16 wedge shaped modules. The overlapping region of the barrel and endcap is at $33° \pm 2°$ and has about 5 radiation lengths of dewar and support material in front of the calorimeter so the calorimeter performance is degraded in that region [45]. The transverse segmentation is such that the towers are a continuation of the projective tower patterns of the barrel LAC.

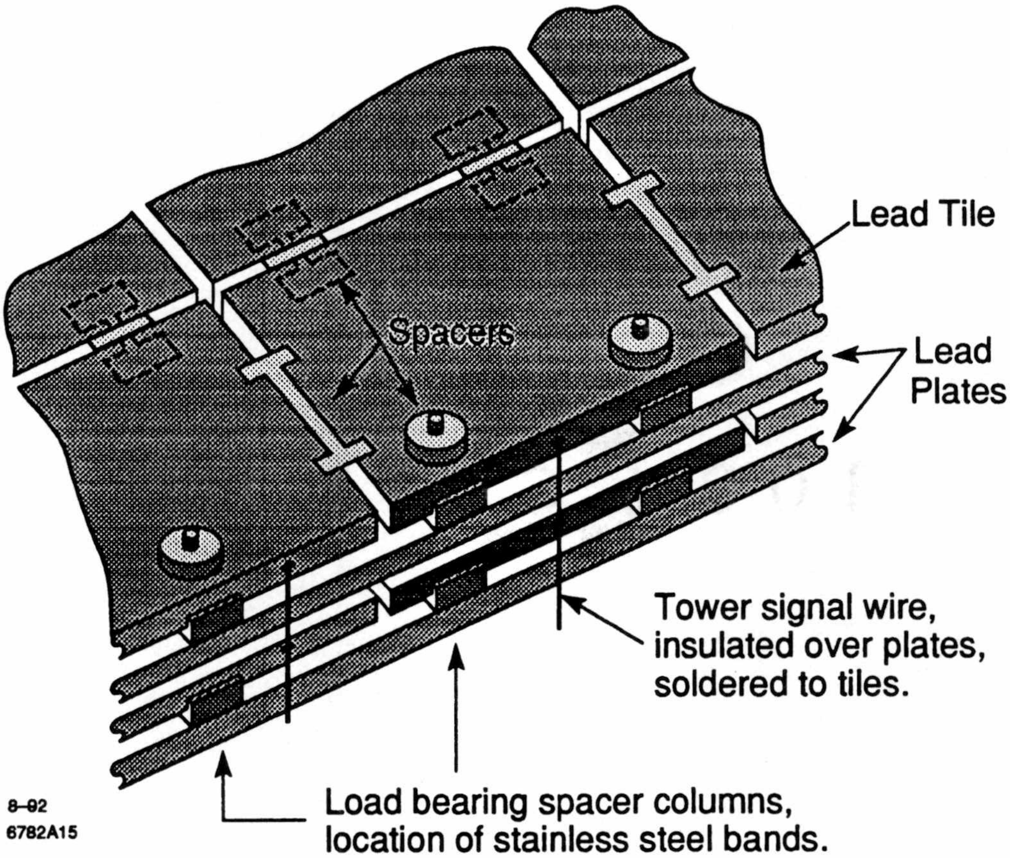

Figure 14: Plate and tile detail of a LAC barrel HAD module.

Warm Iron Calorimeter

The EM and HAD sections of the LAC have a combined thickness of 2.8 absorption lengths, which is sufficient to contain 80-90% of the energy of a hadron shower. The remaining energy is measured by the WIC [46, 47]. In addition to acting as a "tail catcher" to measure energy from hadronic showers, the WIC also provides muon identification and tracking. The WIC is a limited streamer tube calorimeter with iron absorber, consisting of 14 layers of 5 cm steel plates alternating with 3.2 cm spaces which are filled with Iarocci tubes operated in limited streamer mode. The WIC has both a barrel and two endcaps, which together cover almost the complete solid angle. The barrel WIC consists of 8 sections which form an octagonal shaped structure around the magnet coil. The WIC provides the flux return system for the magnet coil and also provides a superstructure for the SLD detector. The barrel is 6.8 m long with an inner radius of 3.3 m and an outer radius of 4.5 m. The Iarocci tubes are gas filled (25% argon, 75% isobutane) square plastic tubes coated with varnish containing graphite, and with a wire down the middle of each tube held at 4.7 kVolts. In addition to the plastic streamer tubes in the space between layers of steel, strips of electrodes are mounted on opposite sides of each tube, to provide muon tracking information. The strips are made of Glasteel, a material similar to G-10, with copper laminated on the surface. In most layers, one electrode is a long narrow strip parallel to the streamer tube and of the same width, whereas the electrode on the opposite side is divided into pads, sized to continue the projective tower geometry of the LAC. Pads are joined together in successive layers to form projective towers. Two of the fourteen layers also contain strips perpendicular to the streamer tubes, to improve muon tracking. Figure 15 shows detail of a WIC section.

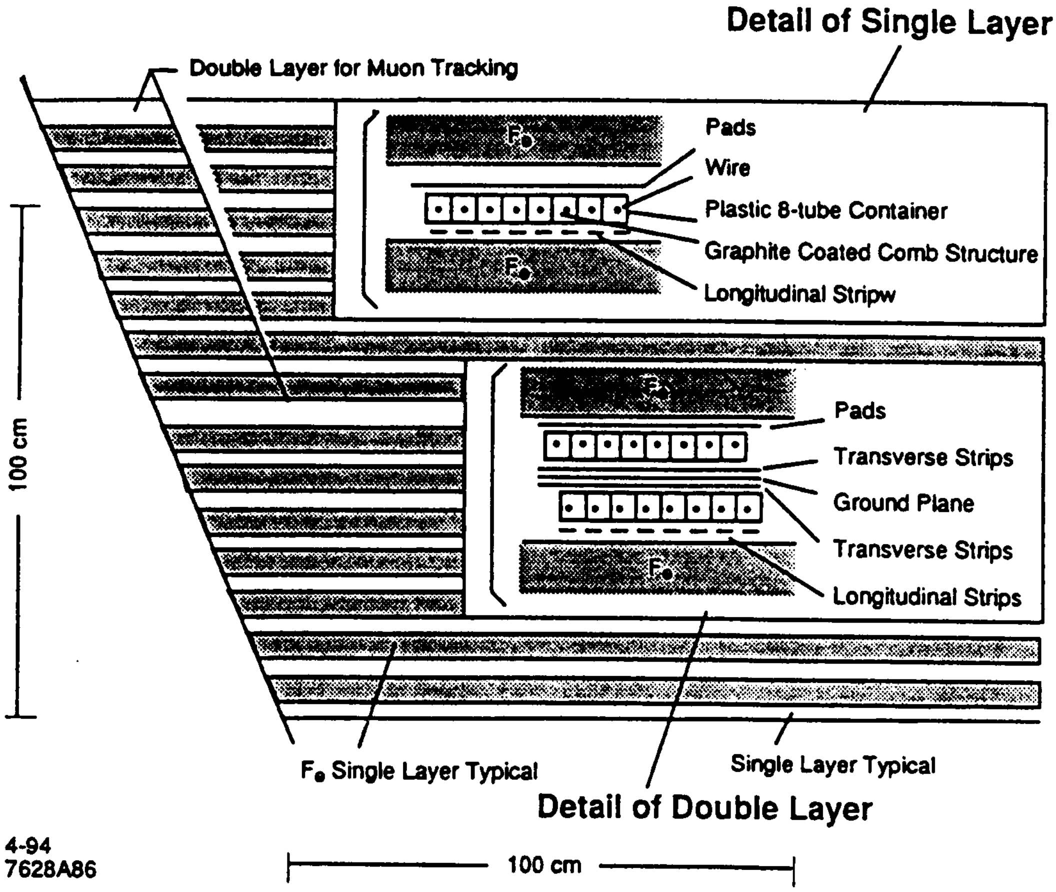

Figure 15: WIC section detail.

Chapter 4

SLD Luminosity Monitor

4.1 Introduction

The small angle electromagnetic calorimetry at SLD consists of a set of calorimeters employing silicon diodes as the sampling medium. The luminosity monitor small angle tagger (LMSAT) consists of 23 layers of silicon diodes separated by tungsten alloy radiator plates and provides coverage from 28 to 68 mrad. The medium angle silicon calorimeter (MASiC) provides coverage from 68 to 190 mrad. These detectors and their operation are described in some detail in references [48], [49], [50]. Silicon tungsten calorimetry has several advantages over other types of detectors considered for use at these small angles, for example, a liquid argon luminosity monitor. The spatial constraints are rather severe, and silicon tungsten calorimeters can be made very compact. They operate at room temperature so no cryogenics are required. The fine transverse segmentation possible in silicon diode detectors makes it possible to measure the position of the particles entering the detector without having to use another detector for tracking. Background from SLC makes it difficult to operate a conventional PWC or drift chamber at low angles near the interaction point. Silicon calorimeters are easily calibrated, extremely stable in operation, and undamaged by synchrotron radiation from SLC.

SLD pioneered the use of silicon calorimetry as a luminosity monitor technique, and two of the four major LEP experiments subsequently replaced their original luminosity monitors with similar silicon tungsten calorimeters.

4.2 Operating Principles of Silicon Detectors

The silicon diodes in the luminosity monitor and medium angle silicon calorimeter are high resistivity n-type semiconductors with p-type ion implantation on the front surface to form the junction diode [49]. When a charged particle passes through the field region, one electron hole pair is produced for each 3.6 eV of deposited energy. Silicon detectors have excellent resolution due to the large number of charge carriers for a given amount of energy loss, which reduces statistical fluctuations. Electrons and holes move across the detector in the presense of an applied electric field and induce a current pulse at the electrodes. The detectors are operated in reverse bias mode, and are fully depleted, meaning that the depletion region extends throughout the full volume of the silicon wafer. They are operated at a voltage well in excess of that required for full depletion to ensure full charge collection. In the depletion region the concentration of electrons is very low, and as the passage of radiation through this region causes the creation of electron hole pairs, they are swept out of the region by the electric field. The total current is proportional to the amount of energy lost as the incident radiation passes through the silicon. A more detailed description of silicon detectors can be found in [51].

4.3 Luminosity Monitor Design

Two complete luminosity monitors were built for SLD. The original beampipe design at the final focus called for a 16 mm radius, and the LMSAT and MASiC, which fit closely around the beampipe, were designed accordingly. The construction of the original LMSAT (LMSAT-16) was well underway at the University of

Tennessee when the experience of running SLC for Mark II raised serious concerns about synchrotron radiation backgrounds in the central drift chamber. The beampipe was then redesigned to be 25 mm in radius, and the original luminosity monitor would no longer fit around the new beampipe. The silicon wafers already in hand could not accommodate the larger diameter, since the inner edge of the LMSAT forms a cylinder that fits closely around the beampipe. Nevertheless, construction was completed on LMSAT-16 and it is a fully functional detector. A module of LMSAT-16 was tested in a beam test at Brookhaven National Lab in 1989, but LMSAT-16 was not installed in SLD. At the time the decision was made to increase the beampipe size, the MASiC construction was also almost complete, but with some compromises it was possible to modify its design, since the inner edge formed a conical shape. The front half, which no longer fit around the beampipe, was removed. The tungsten radiators were doubled in thickness to 1.73 radiation lengths (X_0) and only half the original number of silicon layers were used. The MASiC construction was completed at the University of Tennessee and it was installed in SLD. A second luminosity monitor, LMSAT-25, with a modified design which would fit around the larger beampipe was constructed at the University of Oregon and this device operates in SLD. For the rest of this dissertation the term LMSAT refers to this second design.

A LMSAT module consists of 23 layers, each layer containing 0.85 X_0 tungsten alloy radiator and 300 micron thick silicon as the active element, and is deep enough to fully contain electromagnetic showers at SLC energies ($\approx$ 50 GeV). Figure 16 shows a side view of the luminosity monitor and the medium angle silicon calorimeter. The LMSAT consists of four module halves, each covering 180° in azimuth. Two such module halves encircle the beampipe to provide 360° coverage on each side of the interaction point. These two sides will often be referred to in this dissertation as "North" and "South" since the beampipe at SLD runs approximately in the North - South direction, with the electron beam traveling South and the positron beam traveling North. The halves are joined in

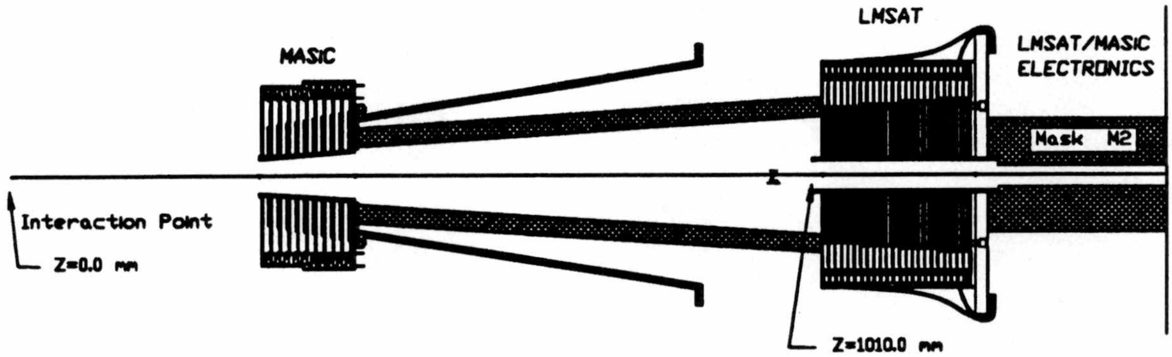

Figure 16: Side view of luminosity monitor (LMSAT) and medium angle silicon calorimeter(MASiC) assembly.

the vertical plane with a 1 mm offset in the active region on both sides of vertical. This creates a two mm gap in active coverage by the silicon, but electrons shower in the tungsten, which does not have a gap in coverage. Since the Moliere radius of a 45 GeV electron shower in tungsten is about 1 cm, the shower will extend beyond the gap and enter the active silicon region on either side, causing about 70% of the energy to be detected in the silicon. Bhabhas striking this region are detected with good efficiency but with degraded energy. Figure 17 shows one plane of the LMSAT.

The front face of each LMSAT module is nominally 101 cm from the interaction point. The SLD coordinate system is defined with the positive z axis in the direction of the positron motion, which is approximately North. The x and y coordinates are defined to form a right-handed coordinate system, with positive y pointing up, and θ and ϕ are the usual polar coordinates, with theta measured from the positive z axis. The LMSAT inner acceptance boundary of 28 mrad is defined by a tungsten snout. The outer acceptance of 68 mrad is defined by the inner edge of the MASiC. The silicon extends to about 84 mrad so that a shower resulting from a particle striking the LMSAT just below the 68 mrad acceptance boundary will be fully contained.

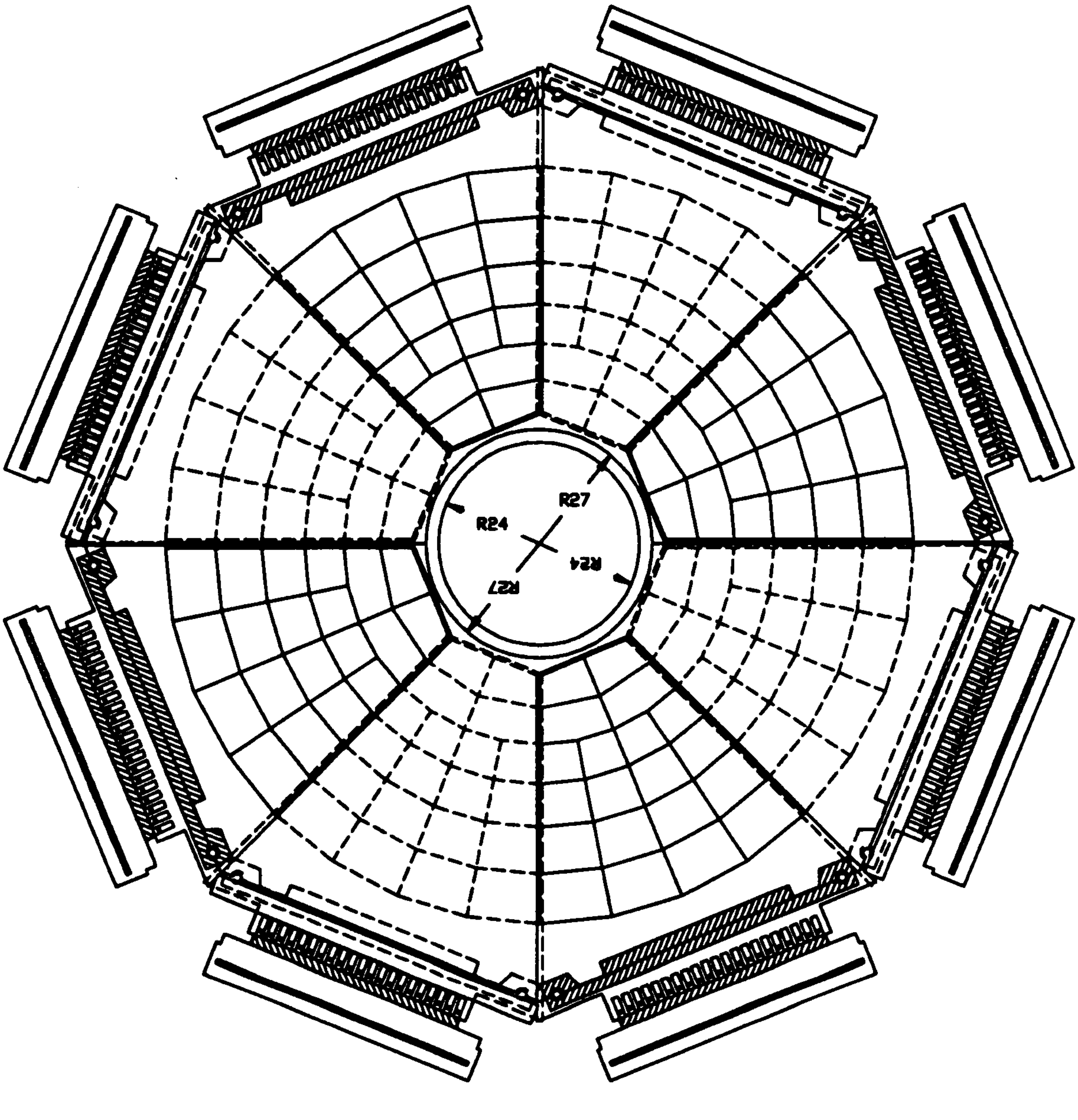

Figure 17: Front face of one plane of the LMSAT.

Each layer of a LMSAT module half consists of four silicon wafers, each providing 1/8 of the total azimuthal coverage. Each wafer consists of 300 μm thick silicon mounted on 0.08 cm FR-4, standard printed circuit board material. Electrical connections are made with conducting epoxy. The wafers were manufactured by Hamamatsu Photonics. The circuit boards are mounted onto the radiator plates, machined from a tungsten alloy of 90% tungsten, 6% copper, and 4% nickel. The wafers are mounted with the FR-4 side (the side opposite the ground plane) of adjacent wafers alternating between facing toward or away from the interaction point. Figure 17 indicates this by showing alternating wafers with dotted lines. The radiator plates are 3.5 mm thick (.85 X_0). A summary of the components of each layer of the LMSAT is given in Table 1 [52].

Table 1: Properties of the materials making up the LMSAT/MASiC

Material	ρ $\frac{g}{cm^3}$	X_0 $\frac{g}{cm^2}$	X_0 cm	$\frac{dE_{minI}}{dx}$ $\frac{MeV}{cm}$
Tungsten	19.3	6.76	0.35	22.39
Copper	8.96	12.86	1.43	12.9
Nickel	8.902	12.7	1.43	13.44
W95Cu5	18.11	6.92	0.382	21.26
W90Cu6Ni4	17.18	7.09	0.413	20.46
Air	0.00121	36.66	30420.	0.0022
Silicon	2.33	21.82	9.36	3.87
FR-4	1.7	33.0	19.4	3.18

The transverse segmentation of each silicon wafer is shown in Figure 18. Each wafer is divided into twenty trapezoidal cells, forming six radial rings. The inner two rings are divided into two segments azimuthally, each covering 22.5°, for a total of 16 cells per layer, per ring. The outer four rings on a wafer are divided into four azimuthal segments, each covering 11.25°, for a total of 32 cells per layer in each ring. Such wafers will be referred to as "wedges" or octants later in the text. The signals from each cell on the wafer are ganged longitudinally to form projective towers. Each tower is segmented longitudinally into two parts for

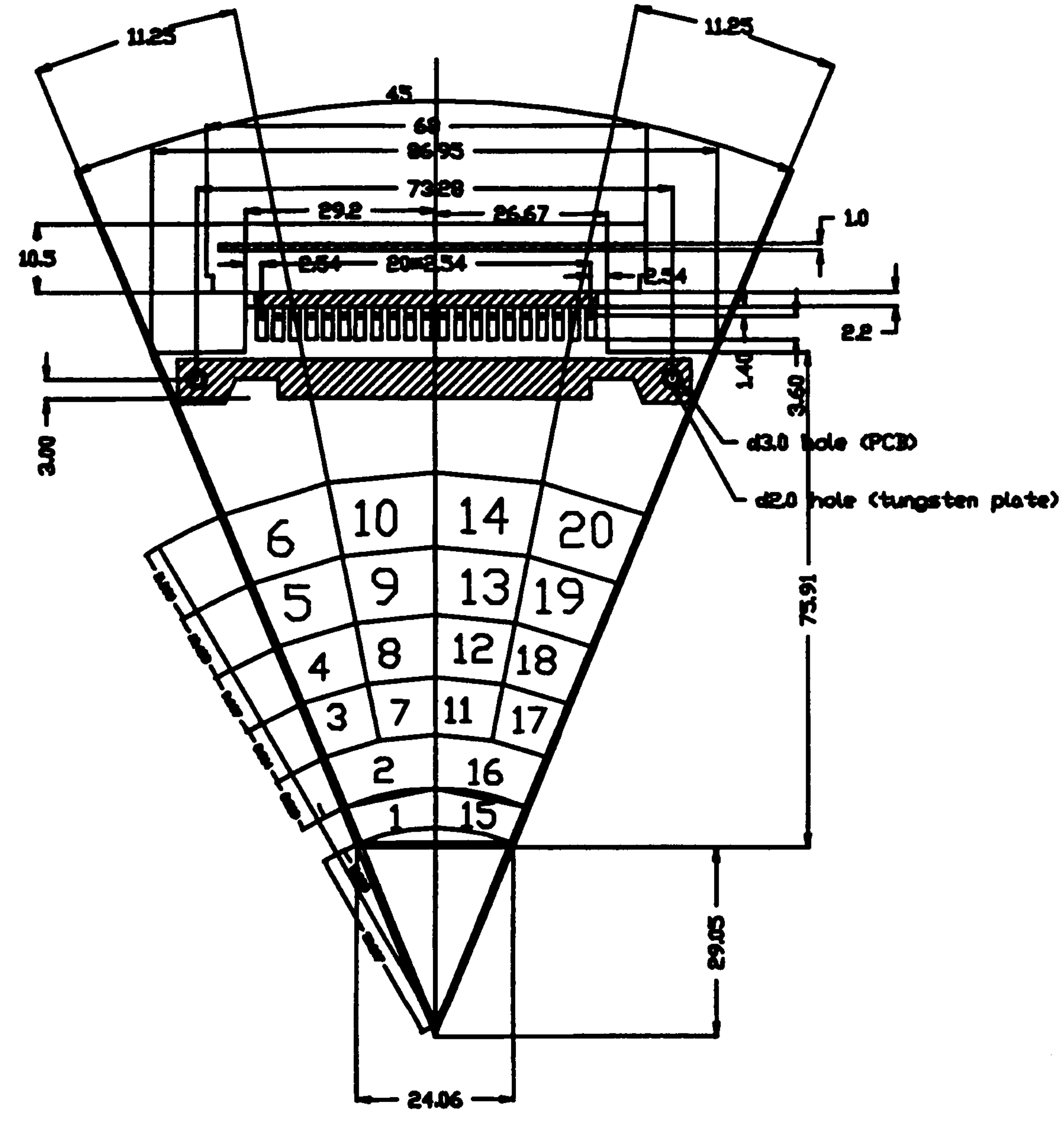

Figure 18: A single silicon wafer from the LMSAT.

readout purposes. The first six layers are ganged together to form EM1, and the remaining seventeen layers form EM2, with a total of 160 towers in each of the two segments. Thus EM1 has a depth of 5.13 X_0 and EM2 has a depth of 14.53 X_0. To conform with the SLD tower numbering convention, the rings are numbered from 51 to 56 starting with the outermost ring and counting inward, as shown in Figure 19.

Ideally, to form fully projective towers the silicon wafer in each layer should increase in size with increasing distance from the interaction point. However, such construction would have been prohibitively expensive, so the chips were manufactured in four different sizes to form approximately projective towers. These four sizes are designated as L1, L2, L3, and L4 with the cell sizes in the L1 design the smallest and L4 the largest. EM1 is composed of 6 layers of L1 wafers, and EM2 has 6 layers of L2 wafers, 6 layers of L3 wafers, and 5 layers of L4 wafers. Figure 18 shows the L1 design. A typical electromagnetic shower is 87% contained in the tower initially struck and the immediately contiguous towers. The silicon diodes are operated in a reverse biased mode, with an operating voltage of -75 Volts so that they are fully depleted. A typical diode becomes fully depleted at about -20 Volts so normal operation involves considerable overbias for full charge collection.

The MASiC is similar in design to the LMSAT. Modifications required for the increased beampipe size included doubling the thickness of the tungsten alloy plates and using fewer layers. Therefore the MASiC consists of ten silicon-tungsten layers, each with a total of 1.74 X_0. The tungsten alloy plates are 0.66 cm thick, and are a slightly different alloy than was used for the redesigned LMSAT. The MASiC radiator plates are 95% tungsten and 5% copper. Two module halves encircle the beam pipe on each side of the interaction point and each module half consists of four silicon wafers as in the LMSAT. These wafers are segmented into only twelve cells, however, with only four rings instead of six. Azimuthal segmentation is identical to the LMSAT, with the inner two rings divided into two segments and the outer two rings divided into four segments. The first three layers of the

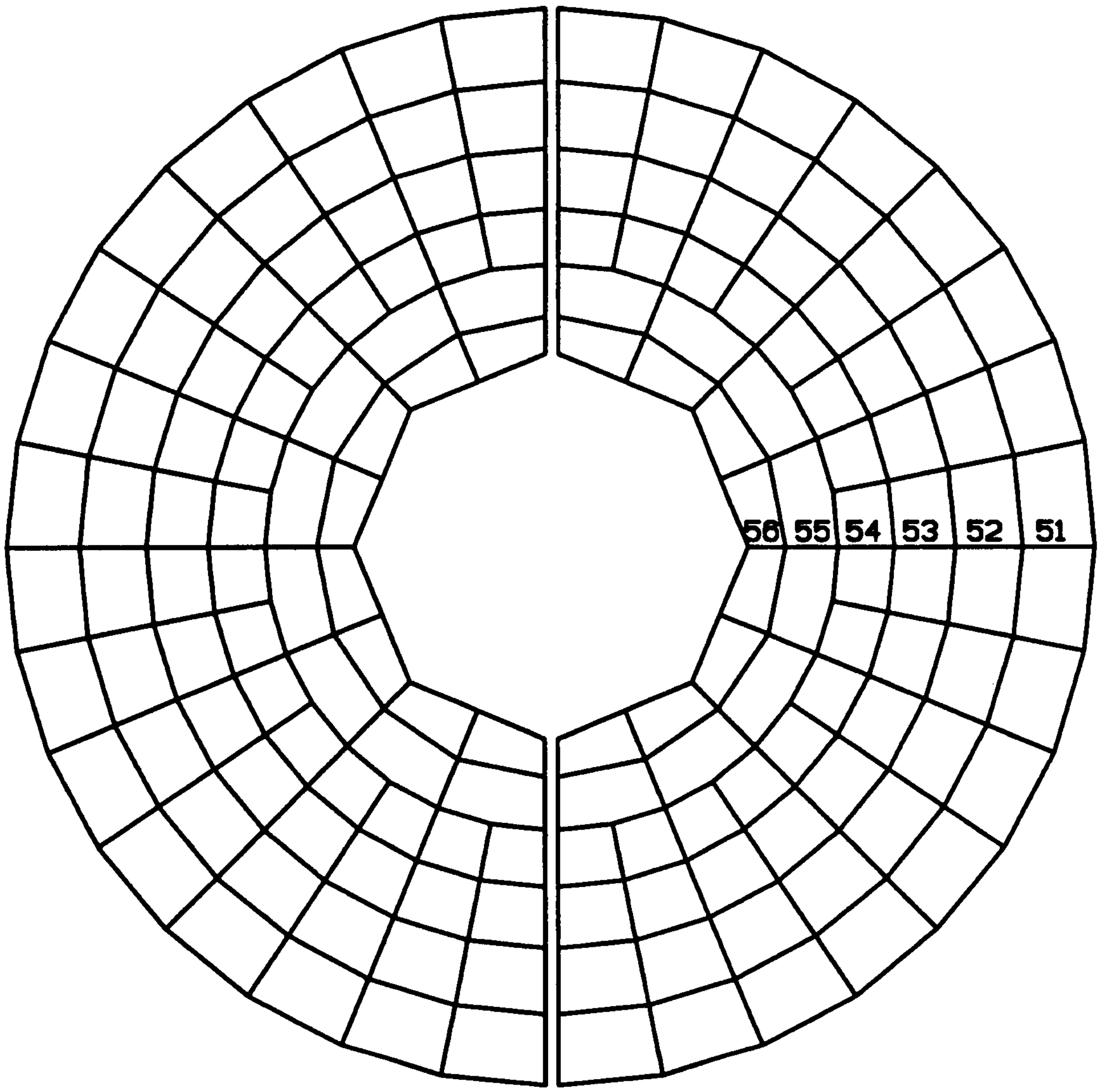

Figure 19: Front face of LMSAT showing SLD tower numbering for rings in theta.

MASiC are ganged together to form EM1 and the last 7 are ganged together to form EM2. Only two sizes of silicon wafers were used after the redesign, one for EM1 and one for EM2. The front face of the MASiC is located 31 cm from the interaction point, one module on each side. The small angle calorimetry was split between two sets of detectors, the LMSAT and MASiC, so that the MASiC, located closer to the interaction point, could serve as a mask for scattered radiation. This radiation would cause undesirable high backgrounds in the central drift chamber. The MASiC also extends electromagnetic coverage to 190 mrad, where the endcap LAC begins. Table 2 shows the thicknesses of materials used in the LMSAT and MASiC [52].

Table 2: Materials making up the LMSAT/MASiC

Material	LMSAT Thickness		MASiC Thickness	
	cm	X_0	cm	X_0
Tungsten Alloy	.35	0.85	.66	1.73
Air	.24	7.89×10^{-6}	.25	8.2×10^{-6}
Silicon	.03	.00321	.03	.00321
FR-10	.08	.00412	.16	.00825
Total/cell	.70	0.855	1.10	1.74
cells/device	23		10	
Total/device	16.1	19.66	11.0	17.39

4.4 Luminosity Monitor Performance

Important characteristics of a sampling calorimeter used as a luminosity monitor are energy and angular resolution. In this section the performance of the luminosity monitor with respect to these characteristics is discussed.

4.4.1 Energy Resolution

For a monoenergetic particle, the spread in energies measured in a sampling calorimeter form a Gaussian distribution, with width determined by sampling statistics. The energy resolution of the calorimeter is usually expressed in terms of the standard deviation, σ, of the distribution divided by the average energy E. Shower fluctuations create an intrinsic limitation on the resolution, and in a sampling calorimeter where only a fraction of the total energy is deposited in the active medium, there are additional sampling fluctuations. In practice several other characteristics of a calorimeter will affect the resolution, and while it is not critical for the luminosity measurement at SLD to achieve optimal energy resolution, one strives to make σ/E as small as possible. Energy resolution is affected by such design characteristics as longitudinal and transverse containment of showers, the selection of the active medium and radiator material, and the sampling fraction. The channel-to-channel uniformity in gains of the readout electronics, the accuracy with which the gains are known, and their stability over time also contribute to the overall energy resolution. Detector segmentation is significant, as is the contribution of background noise. Operationally, a "cluster" size is chosen to contain a shower as completely as possible without the addition of unnecessary channels which might contain noise. The segmentation is chosen so that reasonably sized clusters can be formed.

Except for a short beam test of LMSAT-16 in 1989, no beam tests were possible for the SLD luminosity monitor. In the absence of test beam information, the Bhabha events are used to measure the energy resolution. Ideally one would include only the non-radiative events, which deposit the full beam energy in each side of the luminosity monitor to measure the resolution, but in practice radiative events contribute to the measured energy spread. Figure 20 shows the cluster energy distribution of all Bhabha events from the 1993 run used to measure the luminosity. Cuts used to select these events will be discussed in Chapter 5. In this plot events near the gap between the detector halves and radiative events, both of which have reduced energy in the main cluster, have not been excluded. The presence of such events can be observed in the low energy tail of the distribution. Fitting a Gaussian

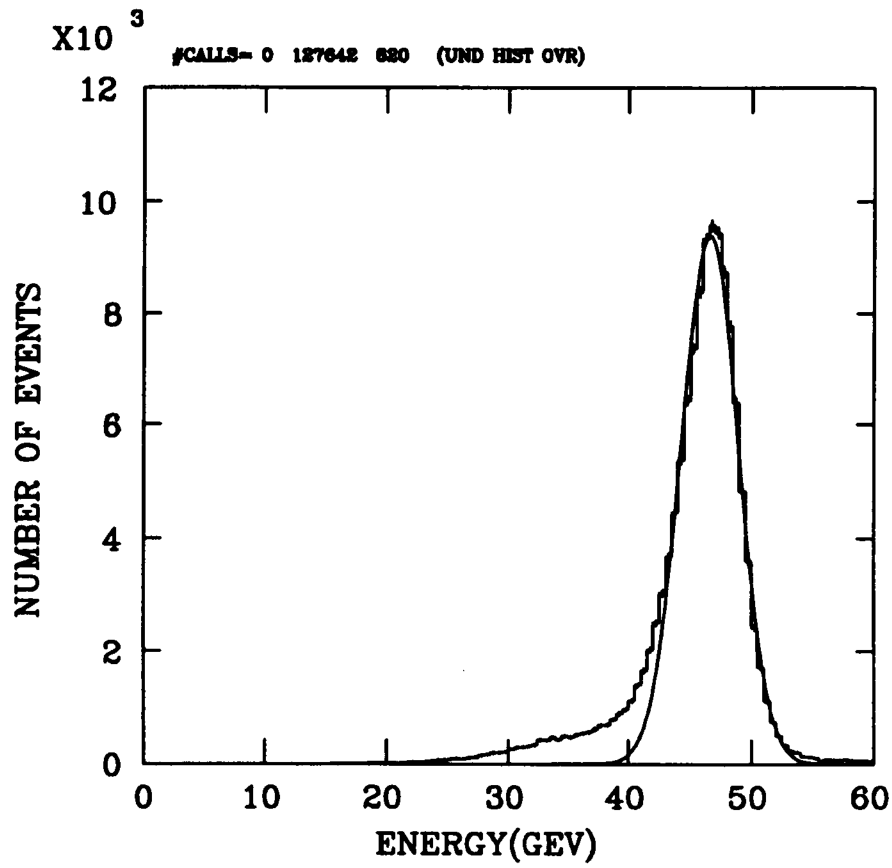

Figure 20: Energy distribution for South LMSAT, using all Bhabhas used for luminosity measurement. A Gaussian fit gives σ/E=4.99%.

to this distribution between 42.5 and 51 GeV gives a resolution of σ/E=4.99%. Figure 21 shows the distribution with a subset of the events shown in Figure 20, where events with one end in the inner ring are excluded, as well as events located near the gap between the two LMSAT halves and identified radiative events. A similar fit of this distribution to a Gaussian yields an energy resolution of σ/E= 4.85%. The resolution is further improved by a correction for a known design feature that affects the energy response. As pointed out in Section 4.3, alternate octants have a different configuration of tungsten absorber, silicon, FR-4, and air. A thin layer of a low Z material such as FR-4 placed adjacent to the silicon has been observed in previous experiments to affect the energy response due to the local hardening effect [53, 54, 55, 56]. The original LMSAT for the 16 mm beampipe was constructed with FR-4 always on the same side of the silicon, but because of spatial constraints, the redesigned LMSAT-25 was required to be somewhat more compact, leading to the adoption of the alternating octant design. The effect of having FR-4 next to the silicon is to cause a small reduction in energy response, but the magnitude of the response depends on whether the FR-4 is in front of, or behind the silicon, with respect to the incoming particles. Without correction this different response of alternate octants degrades the energy resolution. An approximate correction can be made, by treating alternate octants as having different absolute gain. The average energy for each octant is computed using only events with clusters completely contained in that octant. This energy is then normalized to the nominal beam energy, so that the result is eight correction factors, one for each octant. Application of these correction factors results in improvement in the energy resolution for the luminosity monitor. Figure 22 is a scatterplot of E vs. the azimuthal angle ϕ for a subset of the data, prior to the correction, and the effect of the FR-4 in alternating octants is apparent. Figure 23 shows the same set of events after the correction factors have been applied. Figure 24 shows the full energy distribution of all Bhabhas, as in Figure 20, after the correction factors are applied. The resulting resolution is σ/E=4.34%. Figure 25 shows a subset of events

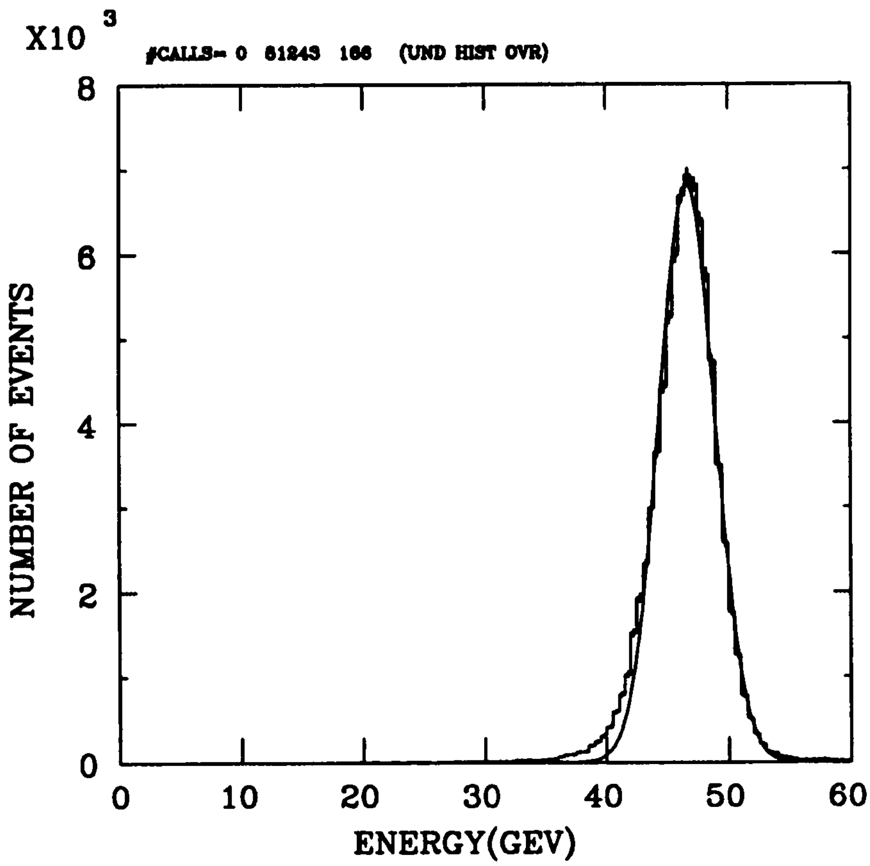

Figure 21: Energy distribution for South LMSAT, using only precise-precise events, and excluding identified radiative events and events near the gap between LMSAT halves. A Gaussian fit gives σ/E=4.85%.

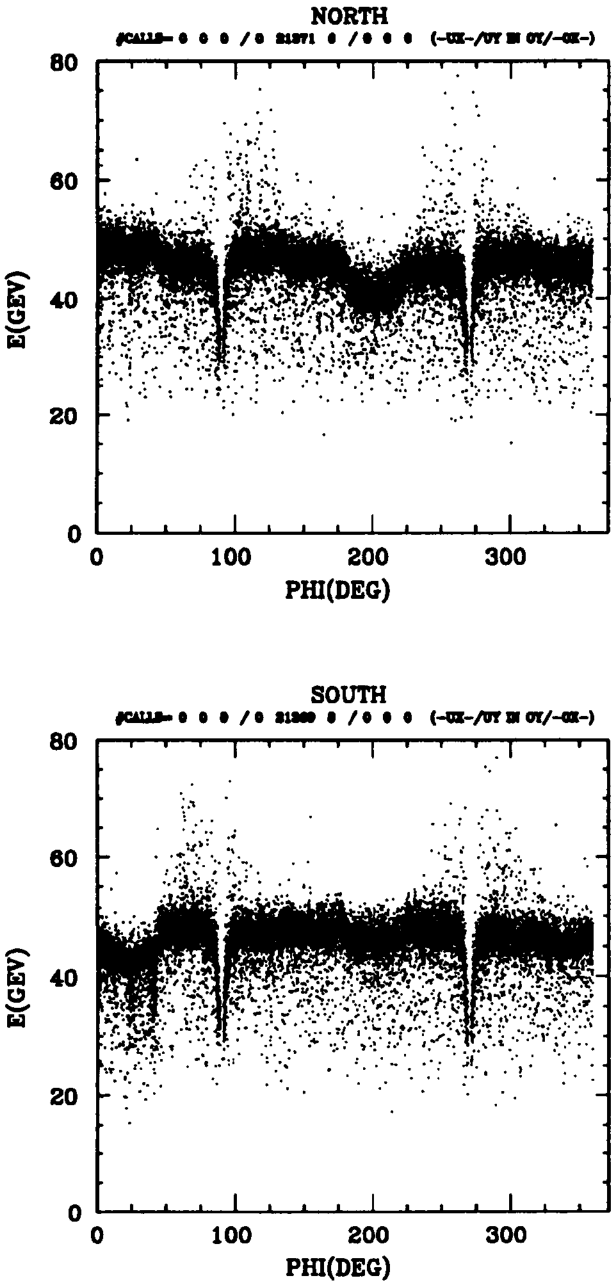

Figure 22: Energy vs. phi before correction for local hardening effect. The top figure is North, the bottom figure is South.

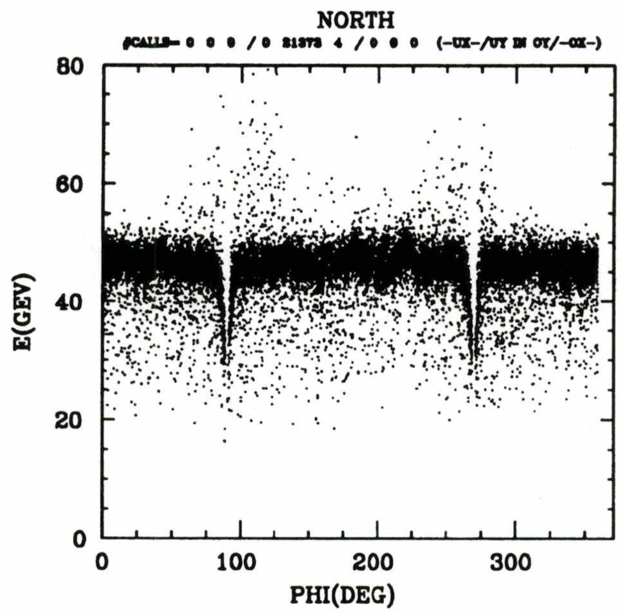

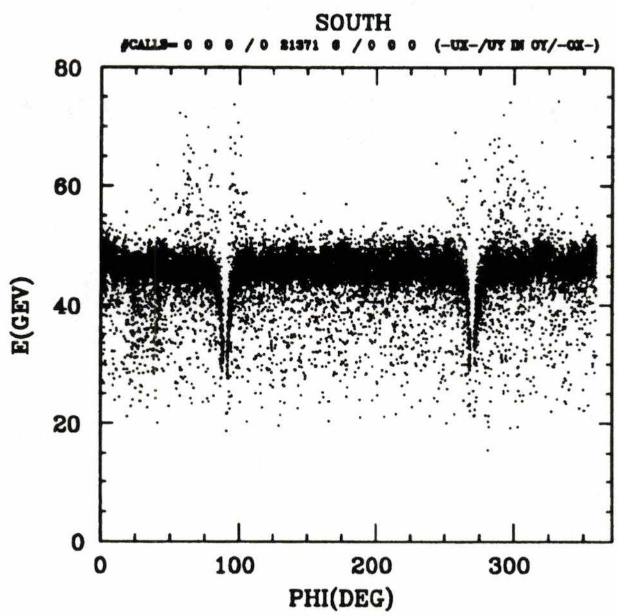

Figure 23: Energy vs. phi after correction for local hardening effect. The top figure is North, the bottom figure is South.

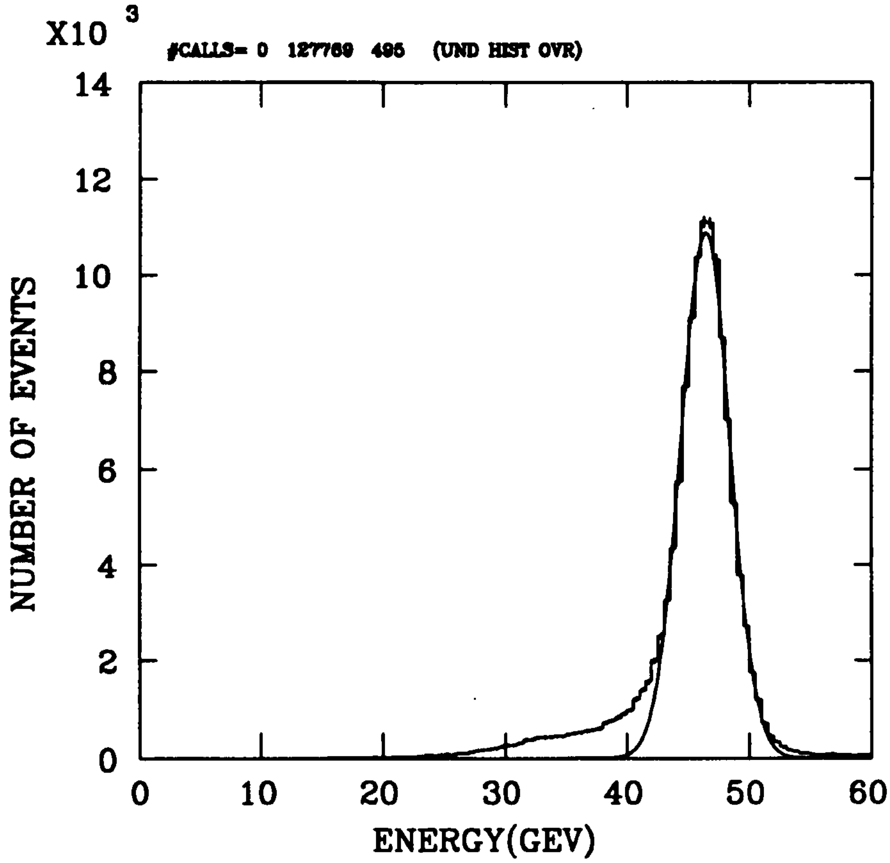

Figure 24: Energy distribution of all Bhabhas in South LMSAT after correction factors are applied. A Gaussian fit gives σ/E=4.34%.

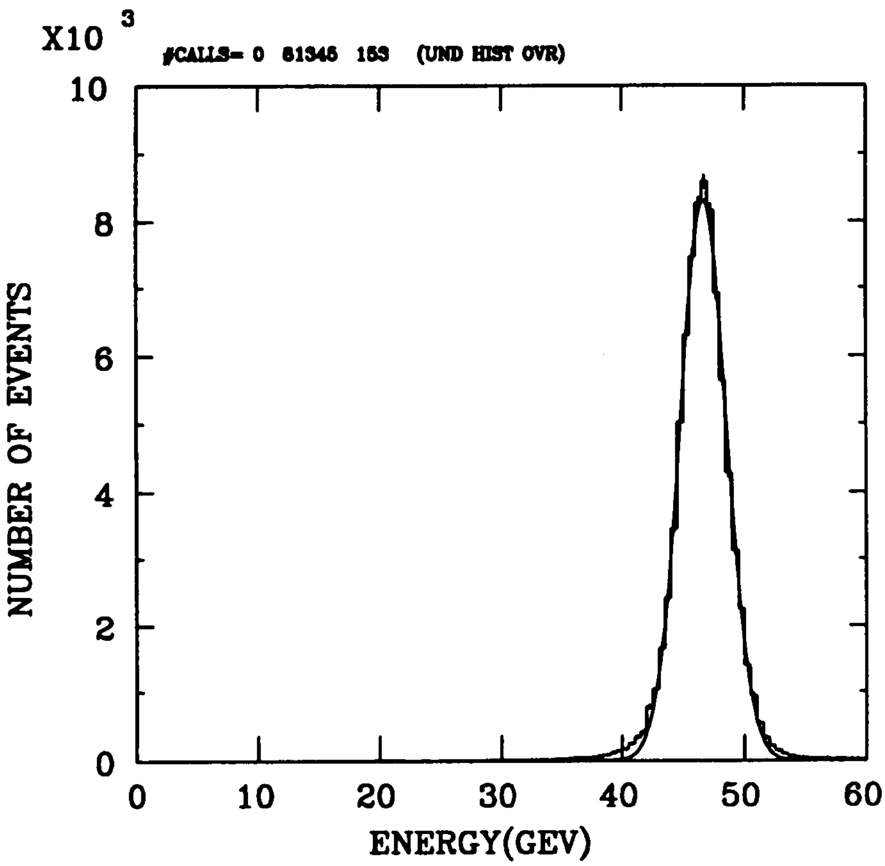

Figure 25: Energy distribution of Bhabhas excluding events with one end in inner ring, events near the gap, and radiative events, after correction factors are applied. A Gaussian fit gives σ/E=4.0%.

with the octant correction factors applied. Events which are obviously radiative are removed, as well as events near the gap and events with one end in the inner ring. The resolution is 4.0% (compare with Figure 21). These distributions can be compared with results from full shower Monte Carlo events, where Bhabha events from the BHLUMI 1.12 generator have been processed through the full shower and detector simulation. The local hardening effect is somewhat exaggerated in version 3.11 of Geant but similar corrections can be made, and the results are shown in Figure 26 and Figure 27. Figure 26 contains all Bhabhas with the same cuts used with data in Figure 24, and Figure 27 excludes radiative events, events near the gap, and inner ring events with the same data cuts used to generate Figure 25. The resolution obtained from these Monte Carlo energy distributions are 3.98% and 3.67% respectively.

Several qualitative observations can be made in examining the distributions in Figure 23 for example. For clarity in plotting only every sixth event was plotted. Some effects to be noted are: 1) The loss of energy for showers near the gap at 90° and 270° is apparent, characterized by events with energy less than $\approx$ 45 GeV. 2) SLC noise is also apparent in the excess of events with energy $>\approx$ 50 GeV in the vertical regions near 90° and 270°. 3) Radiative events with energies less than 40 GeV are clearly indicated.

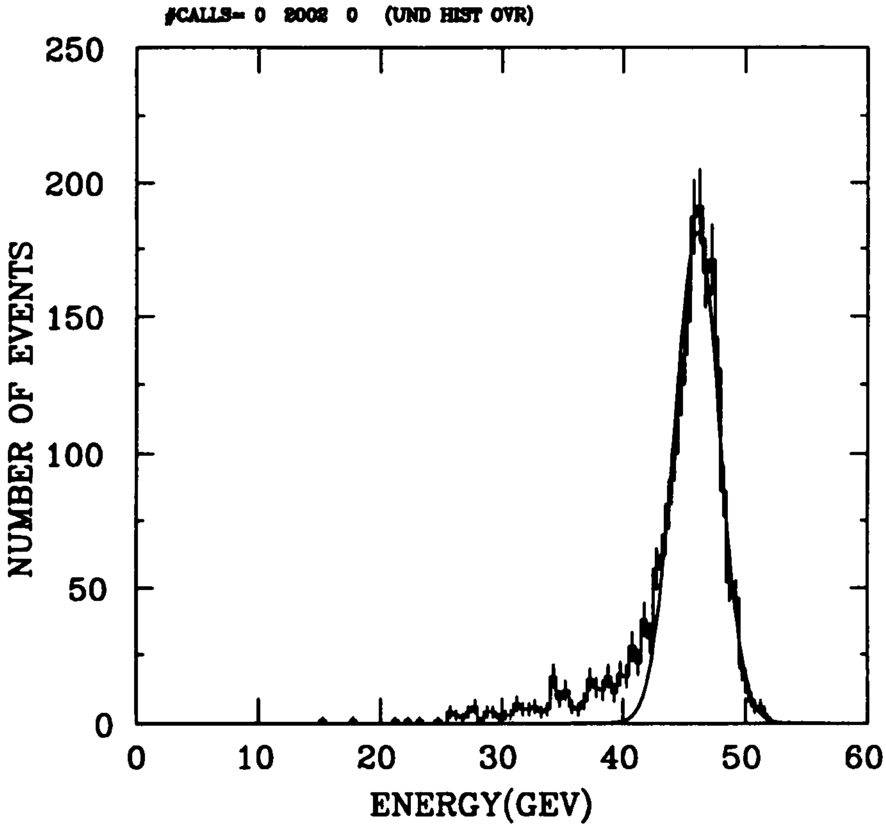

Figure 26: Energy distribution of Monte Carlo Bhabhas using all events. A Gaussian fit gives σ/E=3.98%.

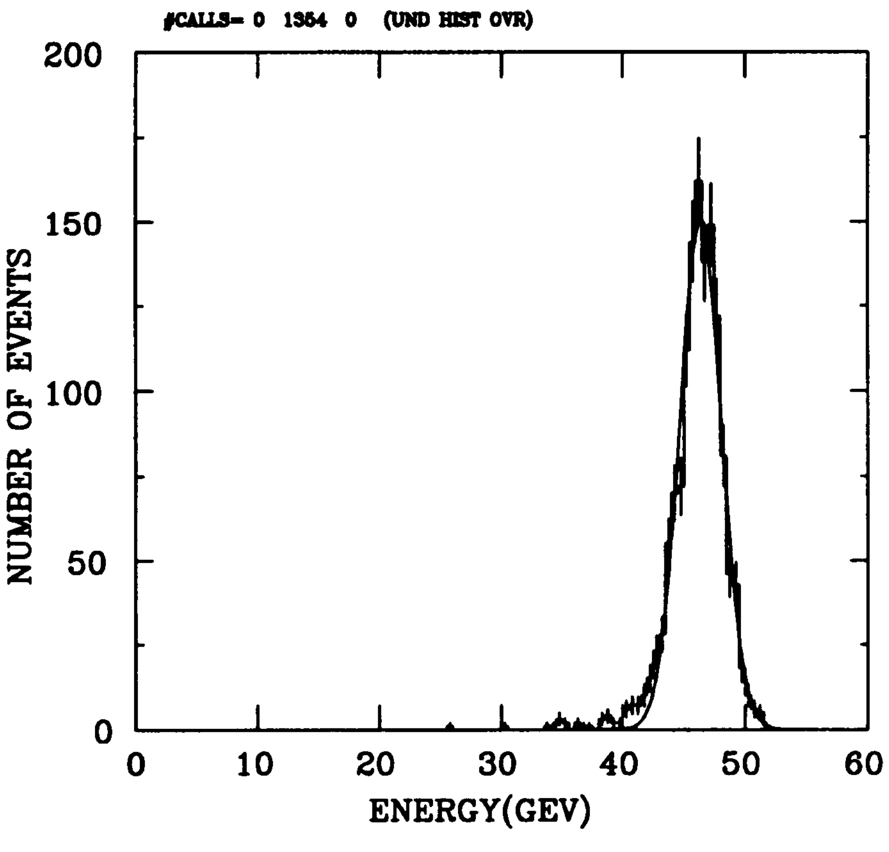

Figure 27: Energy distribution of Monte Carlo Bhabhas excluding events with one end in inner ring, radiative events, and events near the gap. A Gaussian fit gives σ/E=3.67%.

4.4.2 Resolution in θ and ϕ

The measurement of the exact spatial position of an electromagnetic shower in the luminosity monitor is not necessary to classify Bhabha events for measurement of the luminosity, as will be discussed in Chapter 5. The location of Bhabha events for the luminosity measurement and the radiative Bhabha sample is based on the tower with maximum energy. However, the determination of the shower position with precision is important for the study of the characteristics of radiative Bhabha events.

To obtain the shower position for studying radiative events the following method is adopted. A first order position algorithm is a simple energy weighted mean. The coordinates of the central point of each tower is weighted by the energy present in that tower, and all towers in the cluster are summed in this way and the mean calculated. The energy weighted mean theta coordinate is given by:

$$\theta_{EWM} = \frac{\Sigma\theta_i E_i}{\Sigma E_i}$$

where the sum over i is the sum over all towers in the cluster. Similarly, the energy weighted mean phi coordinate is given by:

$$\phi_{EWM} = \frac{\Sigma\phi_i E_i}{\Sigma E_i}.$$

As the showers are narrower than the pad size, this method gives too much weight to the central tower, yielding the theta distribution shown in Figure 28, for data and full shower Monte Carlo events that satisfy the cuts used in the luminosity determination. Clearly this method shows a distinct hump associated with each theta ring but boundaries between rings are well defined.

The energy weighted mean values are then corrected using a technique developed by Bushnin et. al. [57]. Figure 29 shows scatter plots of the calculated theta value vs. the true theta value, using full shower non-radiative BHLUMI events. The top plot shows the energy weighted mean and the bottom plot shows corrected values. The shape of these scatterplots lend themselves to a description

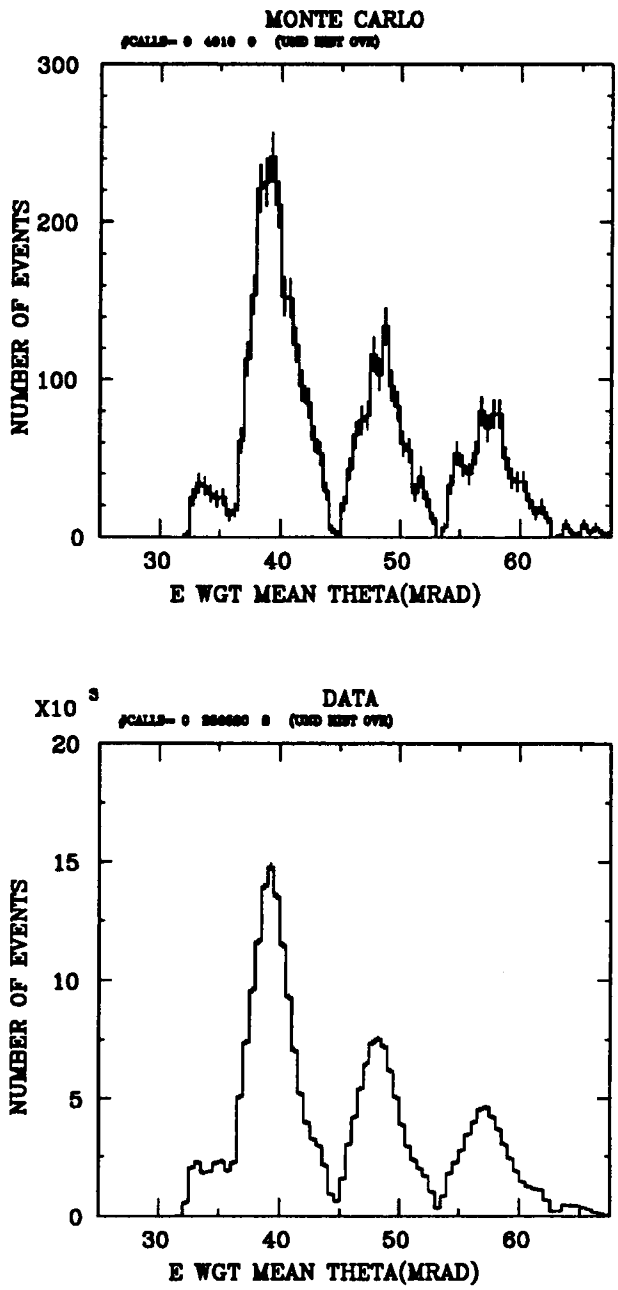

Figure 28: Theta distribution using energy weighted mean for Monte Carlo in top figure and data in bottom figure.

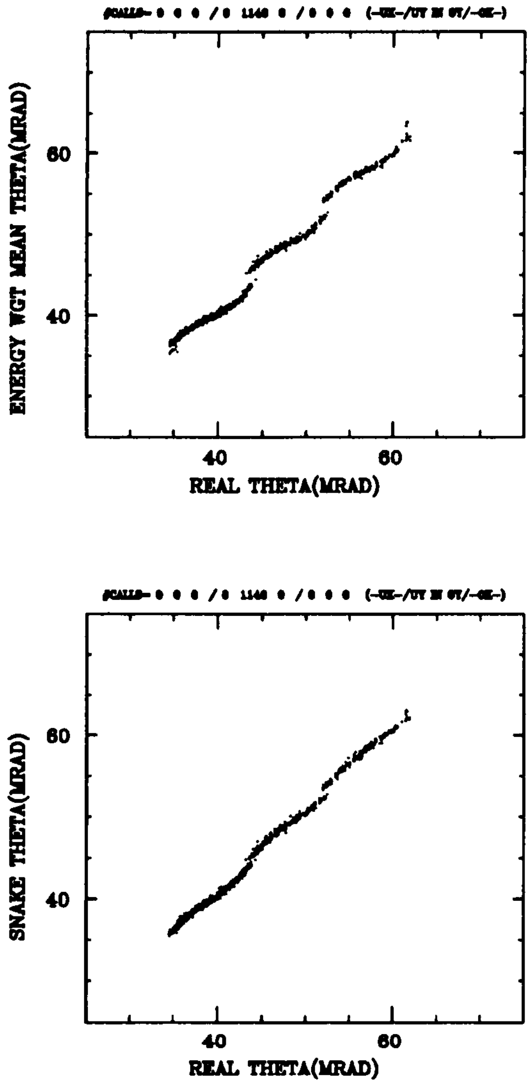

Figure 29: Top plot shows energy weighted mean theta vs. real theta from Monte Carlo, and bottom plot shows "snake" corrected theta vs. real theta from Monte Carlo.

of the Bushnin correction technique as the "snake" correction. The code used to make the snake corrected theta values was implemented in SLD software by Kevin Pitts [58]. Figure 30 shows the theta distribution of Bhabha events after "snake" correction. Although considerably better than the energy weighted mean, improvement on this correction is clearly desirable. Figure 31 shows a scatter plot of the difference between the real theta and corrected theta, vs. real theta, for BHLUMI full shower non-radiative events which satisfy the luminosity cuts described in Chapter 5. Ideally this scatterplot would be nearly flat with the points

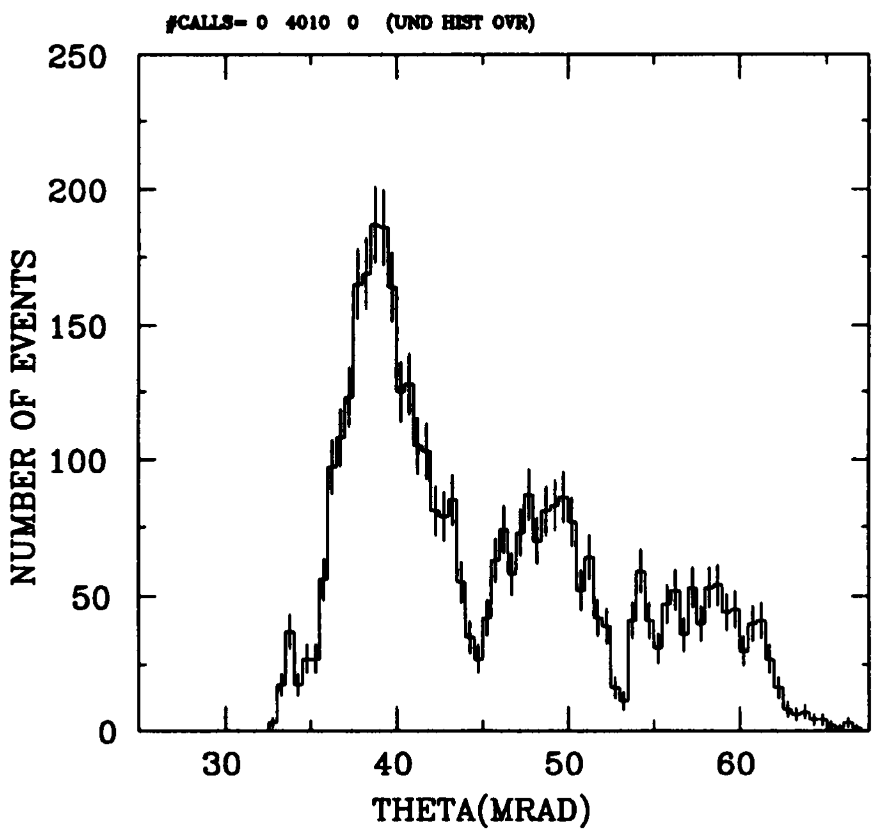

Figure 30: Theta distribution after "snake" correction for Monte Carlo events.

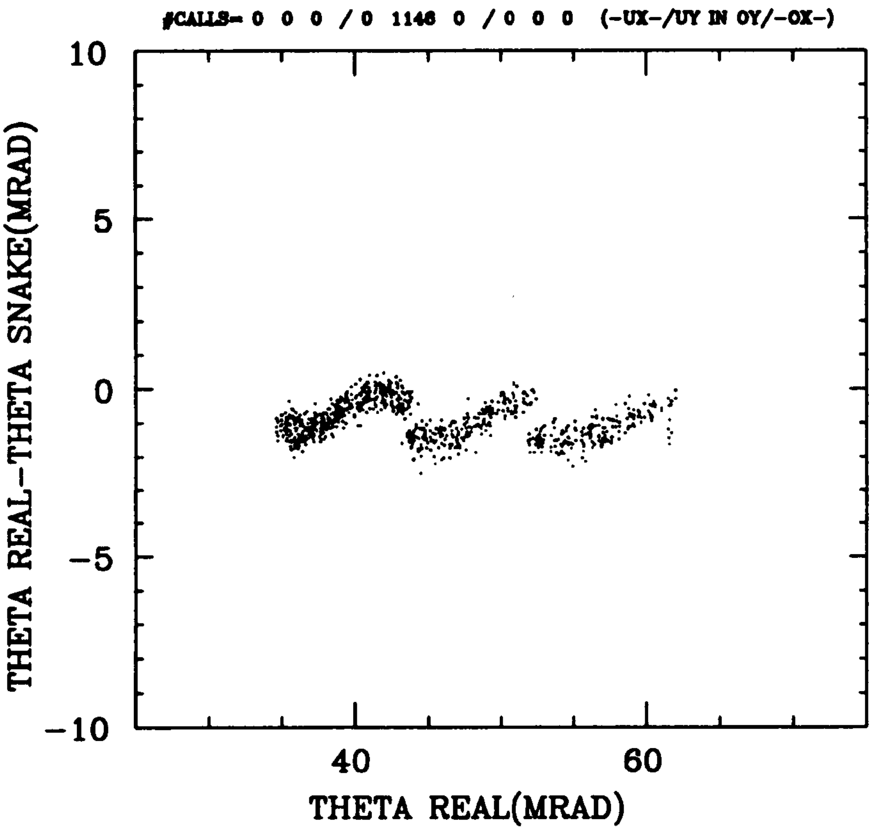

Figure 31: Real theta - snake corrected theta, Monte Carlo events.

distributed closely around zero. In fact it is not flat, and systematically underestimates the actual theta value. The error has a regular pattern, and may be divided into three sections for the events centered in the central three rings. The pattern suggests that further correction is possible.

These Monte Carlo full shower events are used to make a second order, empirical parameterized correction. The shape of the distribution suggests that the points in each of the three regions can be fit to a sinusoidal function, and each point corrected. The method can be extended to rings 52 and 56 by adding radiative BHLUMI events. These events are included in Figure 32. The events in ring 56 are corrected by fitting the distribution with a quadratic and the events in ring 52 are fit to a straight line. The corrections to be applied to the snake corrected theta for each ring are as follows:

$$\text{for } 28 \text{ mrad} < \theta_{\mathrm{SN}} \leq 36.5 \text{ mrad (Ring 56)}:$$

$$\theta_{corr} = 393.2 + 34.1(\theta_{SN} - 28.) - 0.2638(\theta_{SN} - 28.)^2$$

$$\text{for } 36.5 < \theta_{\mathrm{SN}} \leq 45.0 \text{ mrad (Ring 55)}:$$

$$\theta_{corr} = -0.6411 + .58555 \sin[0.739(\theta_{\mathrm{SN}} - 36.5) - 2.3745]$$

$$\text{for } 45.0 < \theta_{\mathrm{SN}} \leq 53.0 \text{ mrad (Ring 54)}:$$

$$\theta_{corr} = -1.0329 + .55237 \sin[0.785(\theta_{\mathrm{SN}} - 45.0) - 2.9884]$$

$$\text{for } 53.0 < \theta_{\mathrm{SN}} \leq 62.5 \text{ mrad (Ring 53)}:$$

$$\theta_{corr} = -1.1680 + .41447 \sin[0.661(\theta_{\mathrm{SN}} - 53.0) - 2.6936]$$

$$\text{for } \theta_{\mathrm{SN}} > 62.5 \text{ mrad (Ring 52)}:$$

$$\theta_{corr} = -1.131 + 0.0409(\theta_{SN} - 62.5)$$

The scatterplot of the difference in the corrected values of theta and the real theta, vs. the real theta, for Monte Carlo, is shown in Figure 33. Figure 34 shows the second order corrected theta vs. the actual theta. The resulting overall theta distribution for the full shower Monte Carlo events using the new correction is

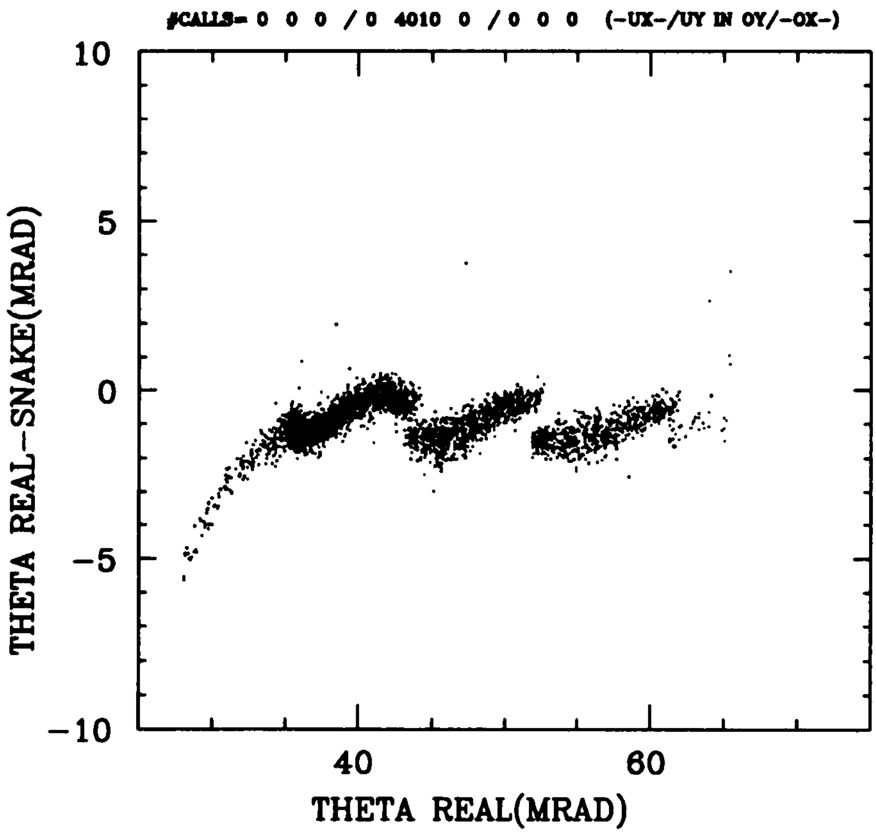

Figure 32: Real theta - snake corrected theta, vs. snake corrected theta.

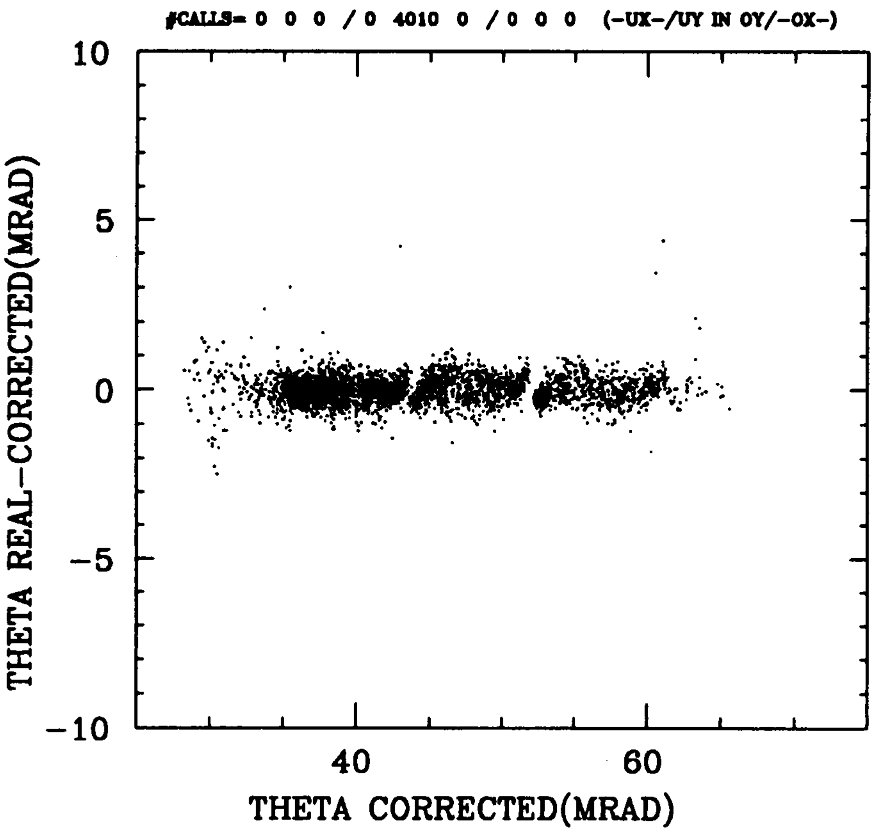

Figure 33: Real theta - corrected theta using second correction, vs. corrected theta.

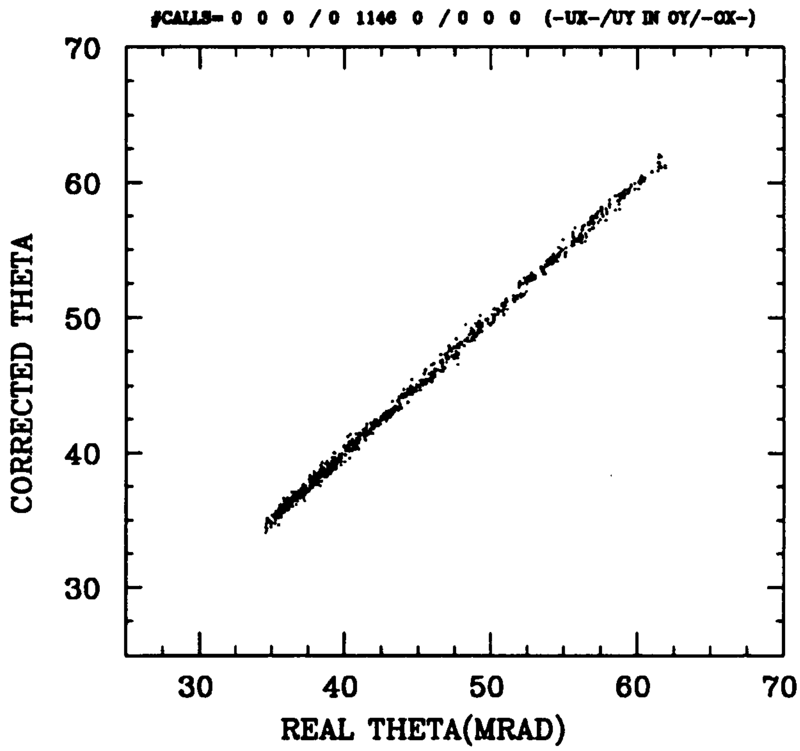

Figure 34: Second order corrected theta vs. actual theta.

shown in Figure 35, which also contains a similar plot for real data. Small peaks appear in the boundary regions between rings 53 and 54, and 54 and 55. This is a residual effect of the discontinuity in corrected theta values near the ring boundaries.

The overall resolution using each of the three methods, energy weighted mean, snake correction, and second order correction, is given by the width of the distribution of the real theta minus the corrected theta from BHLUMI events, shown in Figure 36. The values for the standard deviation for each distribution are $\sigma = 0.79$ mrad for the energy weighted mean, $\sigma = 0.55$ mrad for the snake corrected distribution, and $\sigma = 0.35$ mrad for the second order correction.

Although the snake correction for phi also shows definite structure, no further correction is made. Figure 37 shows a scatterplot of the snake corrected value of ϕ vs. the real value. Figure 38 shows the difference between the real and snake corrected value vs. the real value. The phi coordinates corrected only by the snake correction will be used in the analysis of radiative events. Figure 39 shows an overall phi distribution for BHLUMI events corrected using the snake correction in Monte Carlo and in data. The resolution in phi is determined from a distribution of the corrected phi minus the real phi. Figure 40 shows this distribution separately for the double width phi bins, in rings 55 and 56, and the single width phi bins, in rings 52-54. The distributions are fit to Gaussians. The sigma for the distribution for rings 52-54 is 0.92°, and the sigma for the distribution for rings 55 and 56 is 1.4°.

In summary, the LMSAT measures energy with a 4.0% error at 45 GeV, and it measures theta with a resolution of 0.35 mrad and phi with resolutions of 0.92° and 1.4° for single and double width bins, respectively.

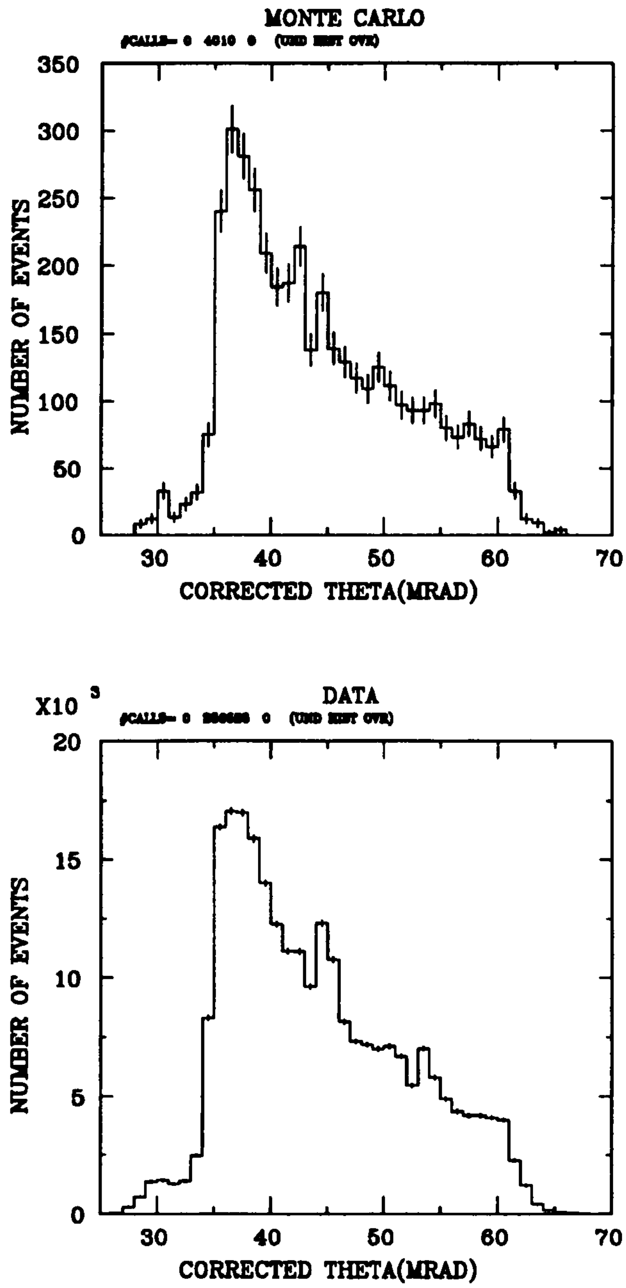

Figure 35: Top plot shows Monte Carlo theta distribution for theta corrected using second correction, bottom plot is the same distribution for data.

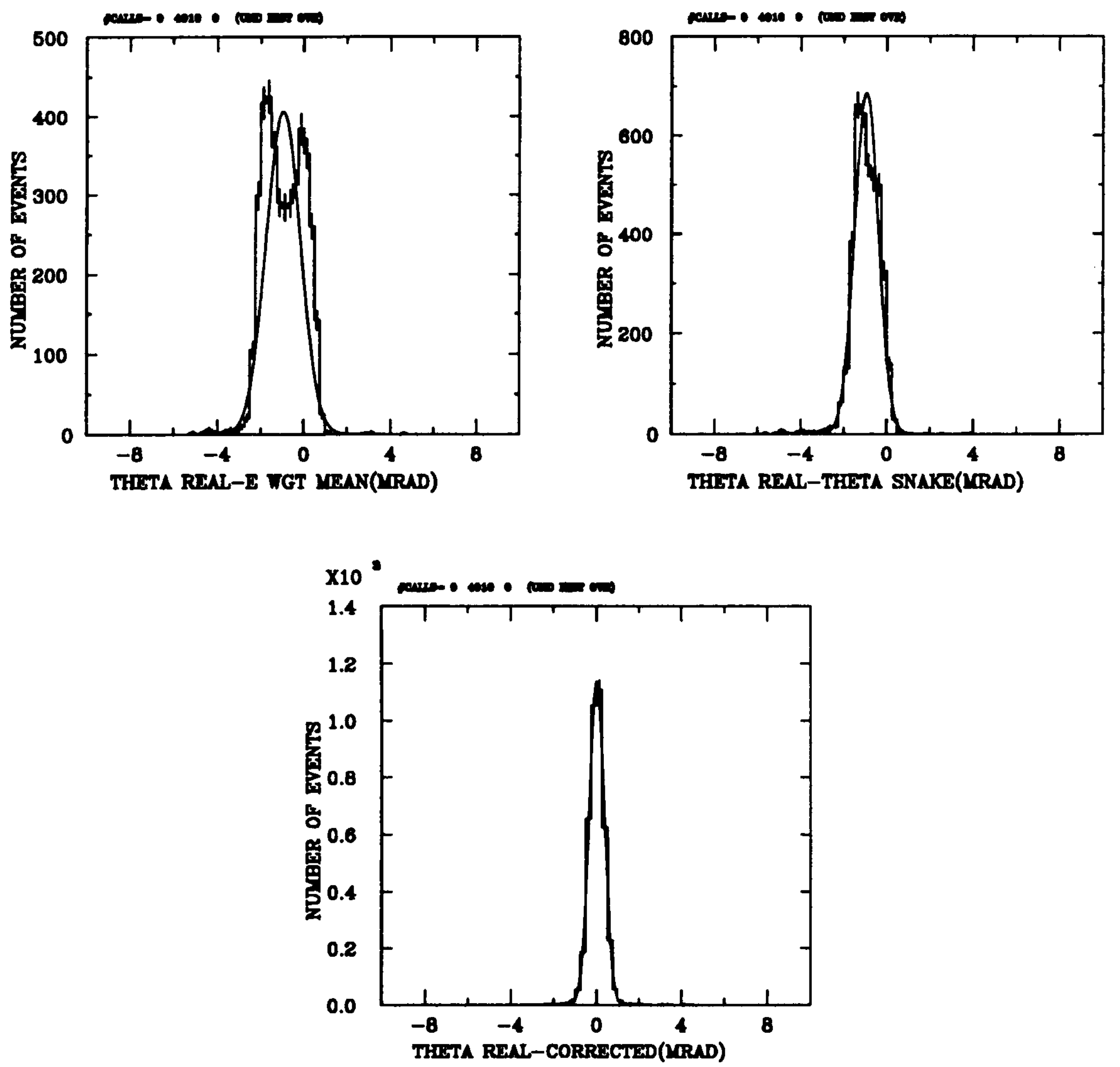

Figure 36: Distributions of real theta minus corrected theta where the corrected theta is energy weighted mean (top left), snake correction (top right), and second order correction (bottom). All distributions are fit to a Gaussian distribution, and the standard deviations are $\sigma = 0.79$, 0.55, and 0.35, respectively.

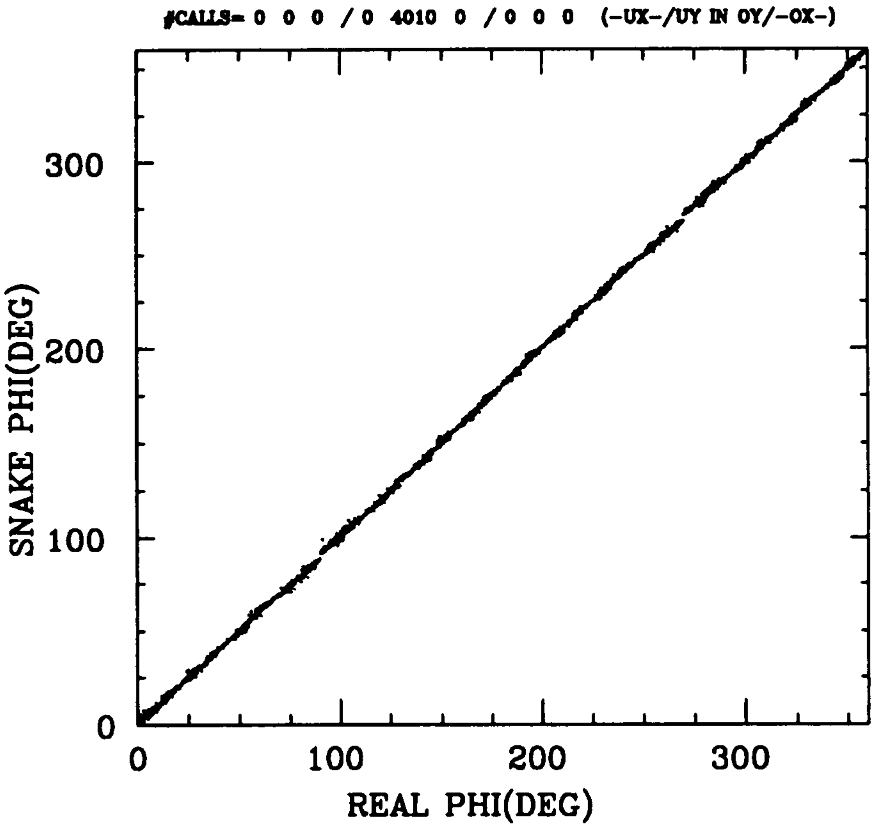

Figure 37: Snake corrected phi vs. real phi, Monte Carlo

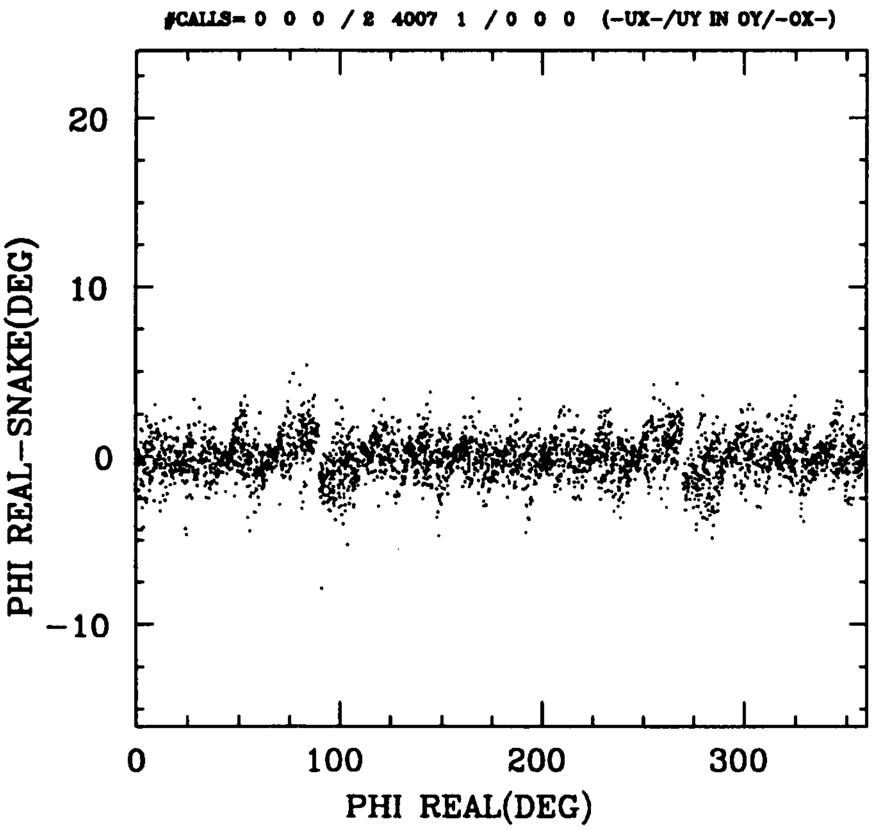

Figure 38: Difference between actual phi and snake phi, vs. actual phi, Monte Carlo.

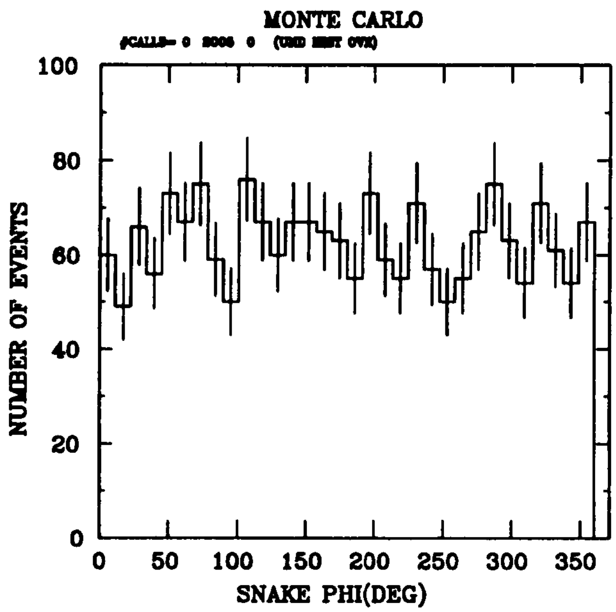

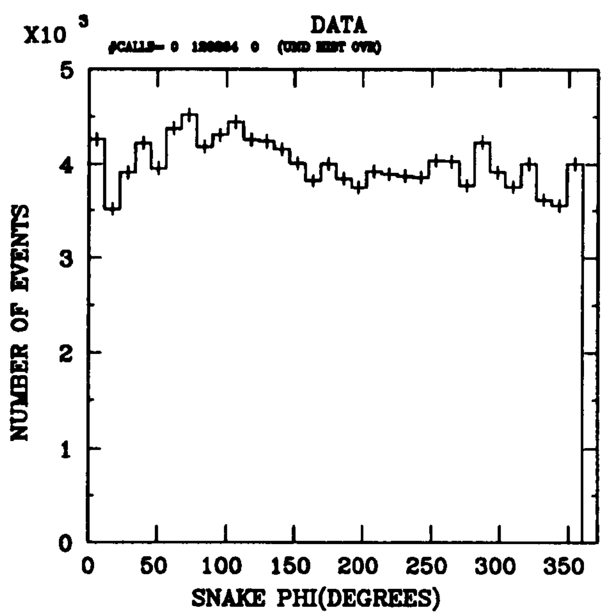

Figure 39: Phi distribution using snake correction in Monte Carlo in top plot and data in bottom plot.

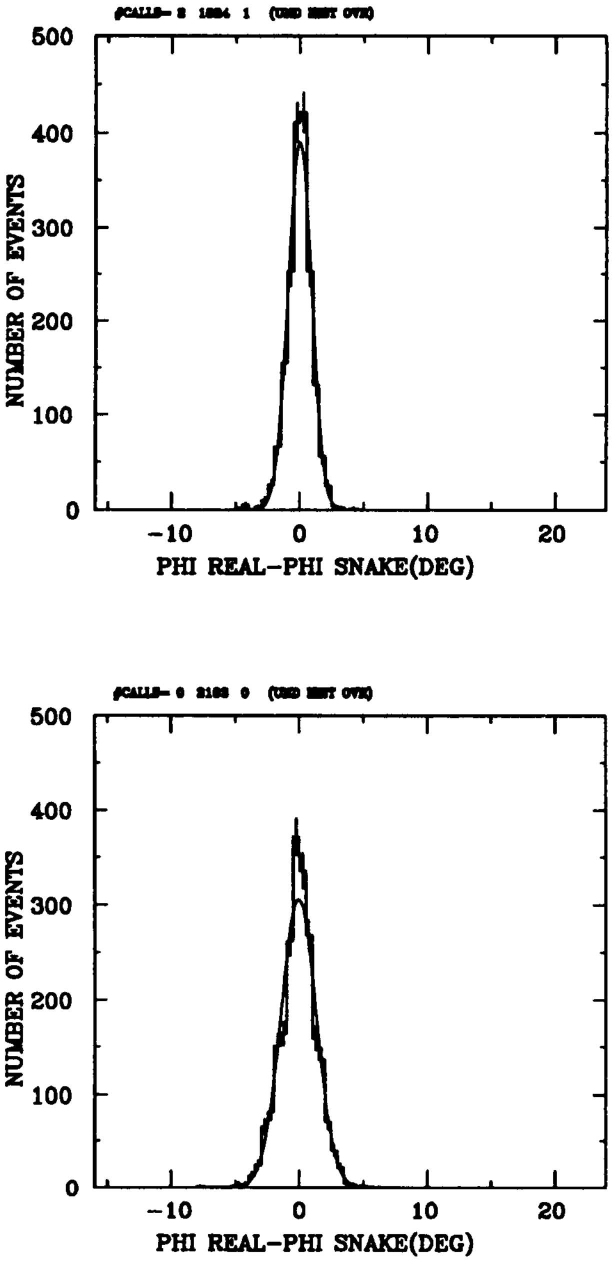

Figure 40: Distribution of snake corrected phi minus actual phi, Monte Carlo. Top figure is for single width phi bins, rings 52-54, fit to a Gaussian distribution with $\sigma = 0.92°$. Bottom figure is for double width phi bins, rings 55 and 56, fit to a Gaussian with $\sigma = 1.4°$.

Chapter 5

Luminosity Measurement

5.1 Introduction

The luminosity at e^+e^- accelerators is determined by measuring the rate of Bhabha scattering, $e^+e^- \rightarrow e^+e^-$, at small angles. The t channel photon exchange process dominates at these angles (less than 10°), with virtually no interference from the Z^0, and the cross section can be calculated from pure QED to great precision. The luminosity $\mathcal{L}$ is given by $\mathcal{L} = N/\sigma$, where N is the number of Bhabha events measured in a high precision luminosity monitor with well understood acceptance and efficiency, and σ is the calculated cross section for that acceptance. For any other process X, where N_x events are measured we can then calculate the cross section for that final state, after the luminosity has been measured, from:

$$\sigma_x = N_x/\mathcal{L}\epsilon_x$$

where ϵ_x is the efficiency for measuring that final state. This chapter will present the measurement of the luminosity for the 1993 SLD run.

5.2 Principles of Luminosity Measurement

The luminosity is measured by identifying Bhabha scattered electrons and positrons in a detector with well understood acceptance and efficiency, at small angles with respect to the beamline. The cross section for Bhabha scattering varies rapidly with polar angle θ ($\approx 1/\theta^3$), so it is important to have a device with precisely defined angular acceptance. SLD chose a silicon-tungsten sampling calorimeter, the LMSAT described in Chapter 4, to measure the rate of Bhabha scattering. The cross section must of course also be calculated to high precision. A Monte Carlo program based on precise QED calculations is used to calculate a cross section for Bhabha scattering between a given set of angles and to generate a large number of Bhabha events. To understand the response of the detector to Bhabhas, these Monte Carlo events are simulated with an electromagnetic shower program, such as GEANT [59] or EGS [60]. Cuts identical to the cuts applied to data are applied to these fully simulated events. The Monte Carlo total cross section and the generated events with cuts applied are used to determine the Bhabha cross section for the acceptance region of the detector employed.

5.3 Method

Bhabha events are identified in the luminosity monitor by their unique signature of a pair of high energy clusters, that are predominantly collinear. Additional clusters may exist for hard photons from radiative events, but multiple hard photons in the luminosity monitor are rare. For non-radiative events, the sum of the cluster energies in the luminosity monitor will be near the center of mass energy. When an e^+, e^- or photon (γ) enters the luminosity monitor, an electromagnetic shower is initiated. The radius of typical showers in tungsten is roughly comparable to the LMSAT pad size, about 1 cm. Due to the tightness of the shower, the energy is well determined by choosing the tower with the maximum energy and summing its energy with the energy in all adjacent towers, as discussed in Chapter 4. Larger clusters are not used, in order to minimize the inclusion of spurious SLC noise. Events are classified by the location of the tower with the maximum energy. Thus the tower boundaries operationally define the fiducial region used in the detector to measure the luminosity. This selection criteria has been studied extensively using Monte Carlo events with Geant simulation of the detector, and more detail will be given on the event selection in Section 5.4.

The Monte Carlo program used for the cross section determination and to generate events is BHLUMI 2.01 [9]. A description of the use of BHLUMI to determine the cross section is given in section 5.6.

Since the Bhabha cross section decreases rapidly with angle ($\approx 1/\theta^3$), the measurement of luminosity is sensitive to displacements of the two LMSAT halves parallel or perpendicular to the beam axis. Displacements can occur from misalignment between the two halves as installed, or from small movements of the final focus magnets to which the LMSAT assembly is attached. Displacement of the interaction point where the e^+ and e^- beams collide from its nominal position has the same effect as physical displacement of a LMSAT half with respect to the nominal interaction point. Such displacements can remove or add events to the fiducial region.

The luminosity has been studied here in two independent ways, with two somewhat independent measurements of the luminosity with different systematic errors. These techniques are labled as the "gross-precise" and "precise-precise" methods. With the gross-precise method [61, 62, 63, 64], the data are analyzed in a way that is insensitive to small displacements. It is based on the fact that if one requires the Bhabha cluster on one end to be in a narrow or "precise" fiducial region, but in a wider or "gross" fiducial region on the other end, the effects of small displacements can be made to cancel to first order. A weighting scheme is used where events with both ends in the narrow region are given a weight of 1.0 and events with only one end in the narrow region are given a weight of 0.5. A displacement can cause an event which should have had both ends in the narrow region to be outside the narrow region on one side, but by allowing a larger acceptance region on one side, most of these events are then retained in the sample.

In the precise-precise method, only the events with both ends in the narrow region are counted. The displacement of the modules is measured from asymmetries in the data, and Monte Carlo events are used to find the correction to the luminosity necessary to compensate for the effect of the displacement. The application of these techniques to the SLD luminosity measurement is described in sections 5.4 and 5.5.

5.4 Event Selection

In order to obtain the sample of Bhabha events used to measure the luminosity, events passing the Bhabha trigger are passed through a set of relatively straightforward cuts. The trigger and these cuts are described in the following sections.

5.4.1 Trigger

For the 1993 run, the SLD Bhabha trigger required an energy of 12.5 GeV in both the North and South LMSAT modules. In forming the energy sum, only EM2 towers containing at least 1.25 GeV were used. EM1 was not included in the trigger energy sum for the 1993 run, since the signal/noise ratio due to SLC beam background is lower in EM1, and experience in the early part of the 1992 run showed that inclusion of EM1 greatly increased the number of false triggers, although these false events were removable by subsequent cuts. EM1 contains on average about 20% of the shower energy. Figure 41 shows the distribution of the energy as it would be seen by the trigger for North and South using full shower Monte Carlo events. The events in the plots are not required to pass the trigger, but are required to pass subsequent cuts identifying them as Bhabhas. These cuts are described in the next section. Events that fail the trigger but which would pass subsequent Bhabha cuts, represent a trigger inefficiency. A single tower, an

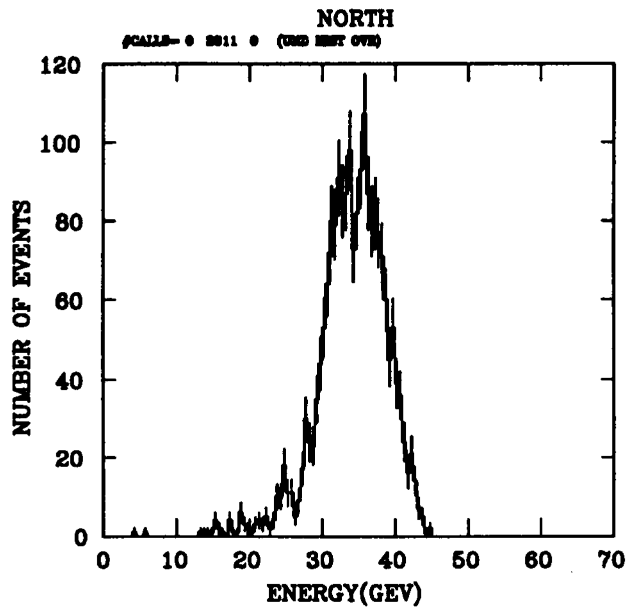

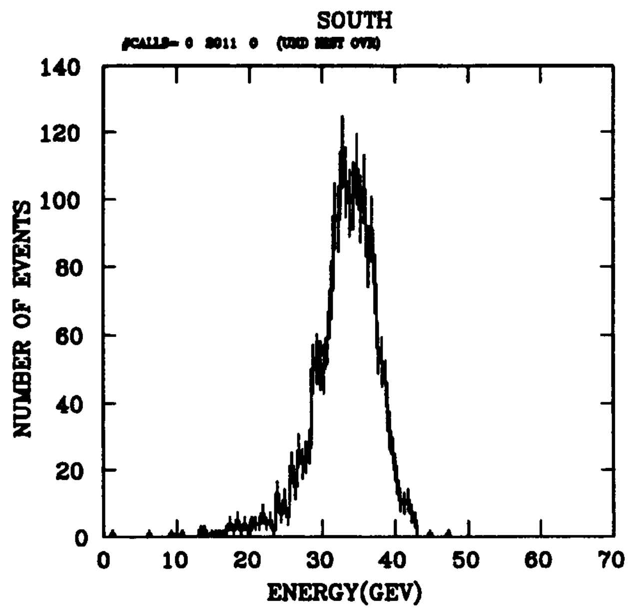

Figure 41: Distribution of energy as seen by the trigger for full shower Monte Carlo events.

EM2 tower on the South side in the innermost ring, was dead for the 1993 run. The presence of the dead tower also decreases the efficiency of the trigger slightly. By including the effect of the dead tower, Monte Carlo simulations show that this trigger is greater than 99.9% efficient for precise-precise events, and is 96.7% efficient for gross-precise events.

5.4.2 Event Classification

Bhabha event selection for luminosity measurement is fairly simple, due to their unique signature of back-to-back high energy clusters in the North and South ends of the luminosity monitor. Clusters are formed around the towers with maximum energy in both the North and South luminosity monitors and the following cuts are applied to all events passing the Bhabha trigger:

$$E_N + E_S \geq 35 \ \text{GeV} \tag{2}$$

$$E_N \geq 15 \ \text{GeV} \quad \text{and} \quad \mathrm{E_S} \geq 15 \ \text{GeV} \tag{3}$$

$$E_N \leq 125 \ \text{GeV} \quad \text{and} \quad \mathrm{E_S} \leq 125 \ \text{GeV} \tag{4}$$

$$\Delta\phi_{N-S} \leq 1 \ \text{tower} \tag{5}$$

The energy cuts of 35 GeV on the total energy and 15 GeV per side are designed to reject low energy background events. Figure 42 shows a plot of the North cluster energy vs. the South cluster energy for a portion of the 1993 Bhabha sample. Most of the events lie in the middle area with energy close to 45 GeV on each side. The lower left hand quadrant contains the radiative events, where a photon is radiated on one or both ends and the full energy is not contained in the primary cluster. The two stripes extending above and to the right of the main concentration of events are events where noise is present along with a Bhabha on one end. Very few events have substantial noise on both ends. Radiative events also may have noise on one end, which account for the events in the lower right and upper left quadrants. Figure 43 shows the cluster energy vs. the polar coordinate θ, and Figure 44 shows

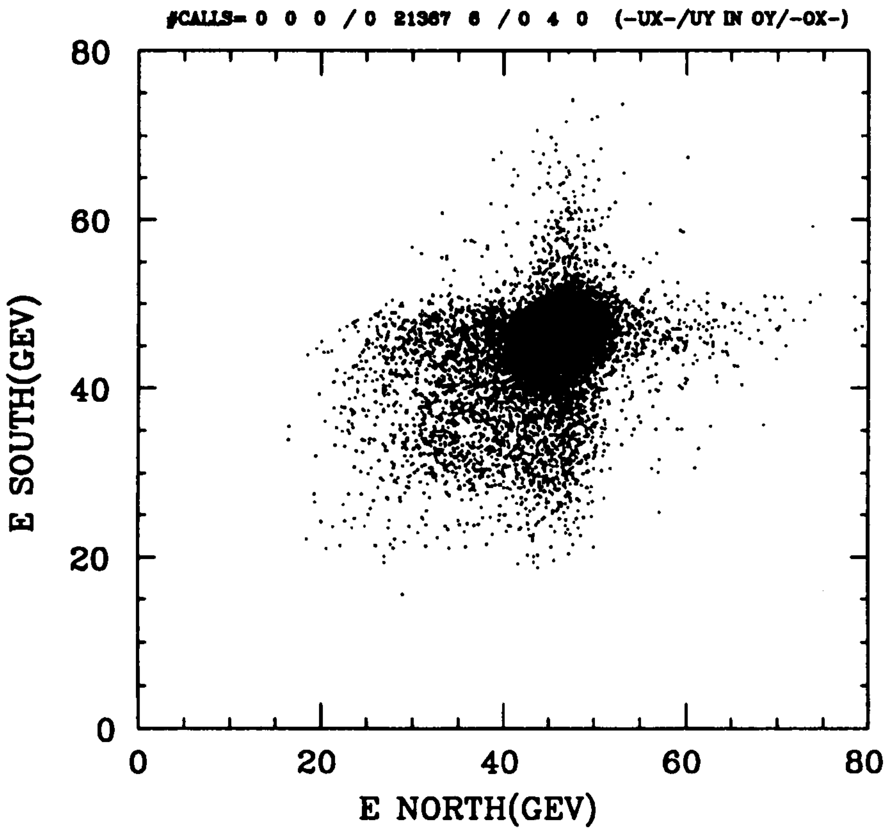

Figure 42: North vs. South cluster energies for a sample of the 1993 Bhabha events.

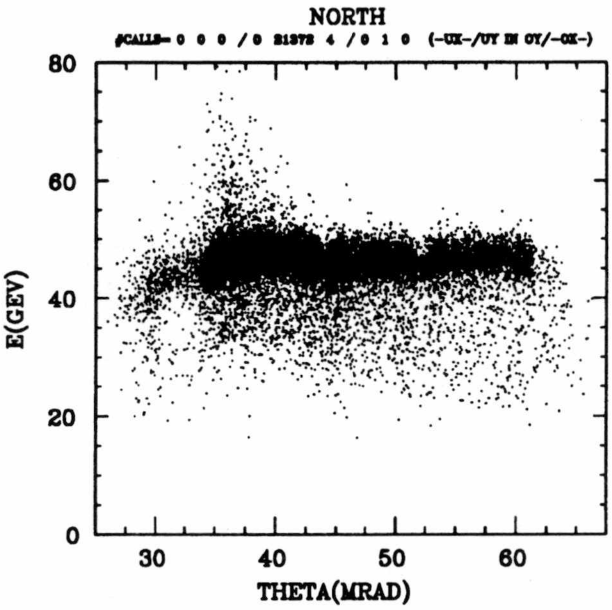

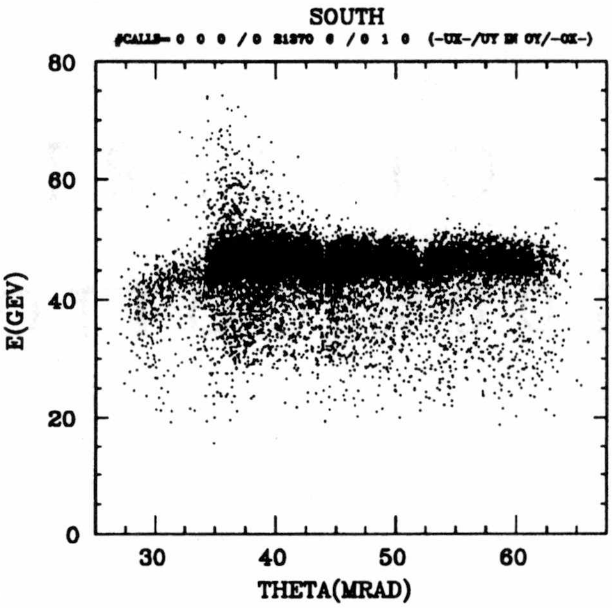

Figure 43: Energy vs. theta for North LMSAT in the top picture and for the South LMSAT in the bottom picture.

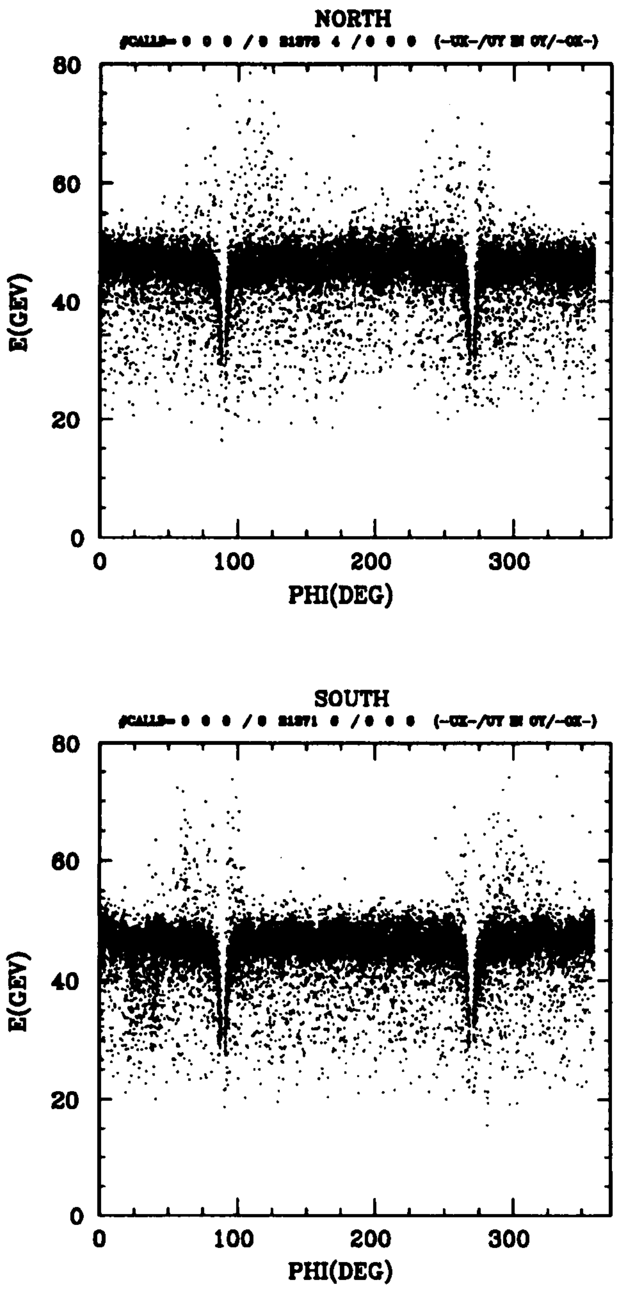

Figure 44: Energy vs. phi for North LMSAT in the top picture and for the South LMSAT in the bottom picture.

the cluster energy vs. the azimuthal coordinate ϕ. For clarity in presentation, the entire data sample is not shown. There is almost no physics background in the luminosity monitor, the primary concern being beam related background. The theta distribution shows that most of the noise is concentrated in the inner ring, as evidenced by the excess of high energy clusters in the low theta region. The phi distribution shows that the noise is also concentrated mainly in the vertical region, near 90° and 270°. The phi distribution also shows that events near the gap along the vertical lose energy in the gap. Both plots show low energy events spread uniformly in theta and phi, which are radiative events with appreciable energy outside the primary cluster. The upper limit of 125 GeV is imposed to reject triggers that occur under poor beam conditions, when many of the luminosity towers are saturated and false clusters of high energy can be formed. A unique feature of SLC noise is the existence of "flyer" events, where beam control is lost on a single pulse. While such events occur relatively infrequently on an absolute scale, they are very likely to satisfy the LMSAT energy trigger. The $\Delta\phi$ cut helps cut out higher energy background events, since they will not typically be in a back-to-back configuration. Although highly radiative events may deviate substantially from the back-to-back configuration, and fail the $\Delta\phi$ cut, the loss of events is small; 0.3% for precise-precise events and 3.5% for gross-precise events. The luminosity analysis is not degraded since similar events are also excluded by $\Delta\phi$ cuts applied to the Monte Carlo events when obtaining the cross section. No explicit cut on the polar angle θ is used, other than the use of the tower with maximum energy to define the fiducial region and classify the clusters as gross or precise.

As mentioned in section 5.2 two acceptance regions are defined in the LMSAT. The narrow or "precise" acceptance region consists of the third, fourth, and fifth rings, counting from the outermost ring, (rings 53, 54, 55 in the SLD tower numbering scheme, see Figure 19 in Chapter 4). This region avoids the inner calorimeter edge, where leakage and/or excess beam noise are significant and also the outer boundary imposed by the Medium Angle Silicon Calorimeter (MASiC) at 68 mrad. A wider or "gross" region is also defined, which includes the entire luminosity monitor, with the exception of the outermost ring which is shielded from incoming particles by a tungsten mask. Ring 52 is included although it is partially shielded from incoming particles by the MASiC. Events with the maximum energy tower in the narrow region in both the North and South luminosity monitors are classified as precise-precise and events with one end outside the narrow region are classified as gross-precise events. Clearly identifiable Bhabha events exist that do not fit either of these classifications, e.g., events with the maximum energy tower in the innermost ring on both ends, but these events are not used for measurement of the luminosity. Events in the innermost ring are less easily separable from beam noise, since the beam noise is most intense at the lower polar angles. Events in this region are also more seriously affected by detector displacement and energy leakage from showers close to the inner edge of the luminosity monitor.

To apply the cuts the Bhabha filtering routine first defines the cluster to be used by selecting the tower with maximum energy in EM1 and EM2 in each of the North and South luminosity monitors, a total of four towers. Clusters are then formed around each maximum tower, using all towers adjacent to it. The maximum energy towers in EM1 and EM2 on a given side (North or South) are usually within one tower of being directly aligned. The Bhabha energy is then determined by adding the EM1 and EM2 cluster energy.

Special treatment is required for events with maximum energy towers in different locations in EM1 and EM2 in a given LMSAT module, that is, towers not directly aligned or within a tower of being directly aligned. The mismatched EM1 cluster is often a false cluster due to beam noise since EM1 contains only about 20% of the total shower energy, but this is less frequently true in EM2, since at that depth in the calorimeter a true Bhabha generally deposits more localized energy than typical noise from SLC. Occasionally a mismatch in the EM1 and EM2 maximum energy towers is due to a radiative event with a separate photon cluster, which may happen to have more EM1 energy than the e^+ or e^- cluster but less

EM2 energy. To make a decision on where to locate and classify an event with mismatched EM1 and EM2 clusters, the algorithm forms two new clusters, one in EM1 and one in EM2, corresponding to the original EM2 and EM1 maximum energy towers, respectively. Two pairs of clusters are formed; the original EM1 cluster with a new EM2 cluster directly behind it, and the original EM2 cluster with a new EM1 cluster directly in front of it. The algorithm then chooses which to use for the "true" Bhabha cluster candidate, based on the fact that for a real Bhabha, EM2 usually has more energy than EM1. The average ratio of the EM1 energy to the EM2 energy is $\frac{E_{EM1}}{E_{EM2}}$=0.27. The $\frac{E_{EM1}}{E_{EM2}}$ ratio is computed for each pair of clusters and the one with $\frac{E_{EM1}}{E_{EM2}} < 1$ is selected as the real Bhabha cluster candidate. If both ratios are less than or greater than one, the algorithm chooses the cluster associated with the original tower with maximum energy in EM2. The effect of this selection on luminosity has been studied by superimposing random noise events on the full shower Monte Carlo sample.

An additional correction is made for events near the dead tower. The dead tower is in the inner ring in EM2 (ring 56), and if an event has its maximum tower for EM1 directly aligned with the dead tower, and the maximum tower for EM2 is adjacent to the dead tower, it is assumed that the event hit the dead tower and the cluster is adjusted to be centered there. If this is not done, a cluster will often be incorrectly classified as being in the precise region, in ring 55 instead of ring 56. Once the clusters have been specified and the energy summed for each, the energy cuts are applied. The 1993 run consisted of 110,360 precise-precise events and 17,904 gross-precise events passing these cuts.

5.5 Gross-Precise Method

In this method Bhabha events in the luminosity monitor are identified as gross-precise or precise-precise events, and an effective number of events is calculated using:

$$N_{eff} = N_{PP} + w \cdot N_{GP},$$

where N_{PP} is the number of precise-precise events, N_{GP} is the number of gross-precise events, and w is the weight given to the gross-precise events. This scheme was originally developed for some of the early experiments at e^+e^- storage rings [61, 62, 63, 64], and is widely used with weight w=0.5 for luminosity measurements to cancel the effects of small displacements. Monte Carlo studies using BHLUMI events indicate that the weighting factor of 0.5 is appropriate for minimizing the error due to displacement. With small displacements of the LMSAT, parallel or perpendicular to the beam axis, the sum of the precise-precise events plus 0.5 times the gross-precise events is close to the number it would have been if the LMSAT were not displaced, although the individual totals of the precise-precise and gross-precise events with and without displacement differ. To check the weighting factor w, events generated by BHLUMI were systematically displaced by known distances in the x, y, and z directions and the number of events classified as precise-precise or gross-precise were compared with those prior to displacement. The weighting factor w is selected by solving for w in the equation

$$(N_{PP} + wN_{GP})_{undisplaced} = (N_{PP} + wN_{GP})_{displaced}.$$

As an example, Table 3 shows results for various z displacements, with x and y displaced as they were in the real data. The last entry corresponds to no displacement in x, y, and z. The optimal value for w is seen to be near 0.5 for realistic displacements in x,y, and z. Moreover, it can been seen in Figure 45 that the error in the luminosity using the gross-precise method, $\Delta\mathcal{L}/\mathcal{L}$, is below 1% until the displacement grows to 4 mm in the radial direction and a few cm in the z direction, values which considerably exceed the actual displacement, as will be demonstrated later in this chapter.

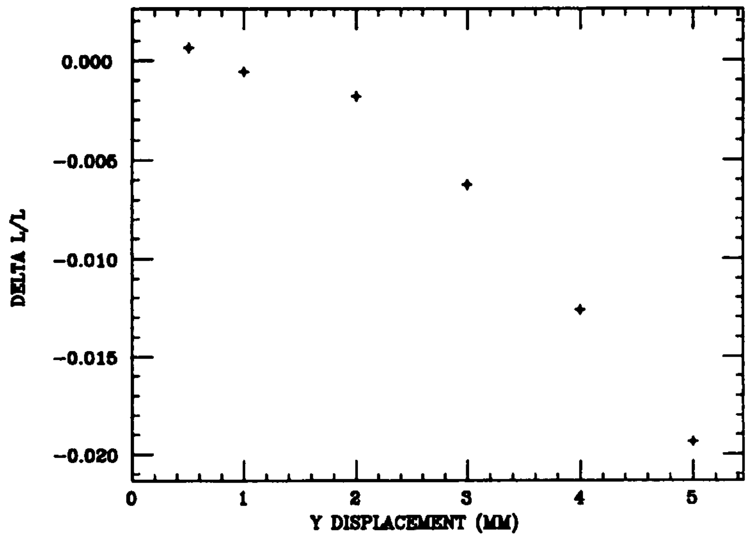

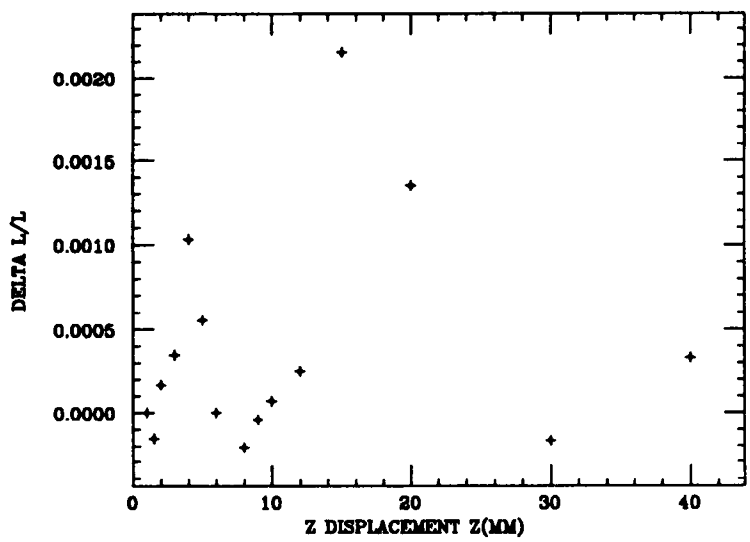

Figure 45: Fractional change in luminosity with y displacement in the top picture and fractional change in luminosity with z displacement in the bottom picture, using the gross-precise method.

Table 3: Number of PP and GP events and the weighting factor resulting from solving $(N_{PP} + wN_{GP})_{undisplaced} = (N_{PP} + wN_{GP})_{displaced}$ for w.

z(mm)	PP	GP	w
0.	33451	4976	.4922
1.	33469	4958	.5000
1.5	33462	4983	.4961
2.	33444	4996	.5042
3.	33400	5071	.5083
4.	33333	5156	.5233
5.	33337	5182	.5124
6.	33325	5246	.5000
8.	33267	5377	.4958
9.	33218	5463	.4992
10.	33141	5609	.5012
12.	32956	5966	.5038
no x,y,z dis	34163	3570	-

5.6 Precise-Precise Method

An alternative technique for dealing with LMSAT displacements, is to measure the displacements from the data, and explicitly correct the luminosity for this effect. This method uses the precise-precise events to calculate the luminosity, with the advantage that events in this region are not affected by some of the systematic errors affecting the events with one end in the inner ring. All events, both gross-precise and precise-precise, are used to determine the displacement. The luminosity measurement is sensitive to displacements of the North and South luminosity monitor with respect to each other, and with respect to the interaction point. The method of measuring the luminosity using only events in the precise region on both sides, requires that the displacement be measured and the luminosity corrected for it. In this section the method of measuring the displacement and making the luminosity correction is described.

Displacements of a luminosity monitor module can be either perpendicular to or parallel to the beam axis. A displacement in the radial direction, perpendicular to the beam, causes an asymmetry in the azimuthal distribution of the Bhabhas. A displacement along the beam axis, the z direction, causes an asymmetry in the number of gross-precise events with their precise side on the North vs. the number with their precise side on the South. These effects can be exploited to measure the displacement. Monte Carlo is used to determine the relationship between the asymmetry in the Bhabha distribution and the displacement. Monte Carlo also shows that for small displacements, the displacements parallel and perpendicular to the beam axis can be treated independently. After measurement of the displacement from the data, Monte Carlo is again used to determine the correction to the luminosity.

Displacements perpendicular to the beam will be addressed first. If the LMSAT modules were perfectly aligned with respect to each other and the beam line, and also if there were no gap between the two halves of each module, the azimuthal (phi) distribution of Bhabha events would be flat. The 2 mm gap between the halves, gives rise to an excess in the phi distribution at 90° and 270°, when plotting phi by towers even in the absence of displacement. This is because events hitting the gap will still shower in the tungsten and will have their maximum tower associated with one of the towers next to the gap, thus increasing the effective area of these towers. If there is radial displacement of a LMSAT module, additional asymmetries will appear in the azimuthal distribution of the Bhabhas in that module. The $\approx 1/\theta^3$ distribution of Bhabhas will cause the side of the LMSAT along the direction of displacement to move from a more densely populated region to a less densely populated region, giving rise to a dip in the azimuthal distribution. It is important to note that the events used to make the phi distribution for a given LMSAT module, are all events in the precise region in that module, with the opposite end either in the gross or precise region.

Monte Carlo studies demonstrate that the phi distribution can be parameterized by a function of the form $dN/d\phi$= A + B $\cos(2\phi$ + C) + D $\cos(\phi$ +E). Figure 46 shows the phi distribution for BHLUMI events with no displacement, and also

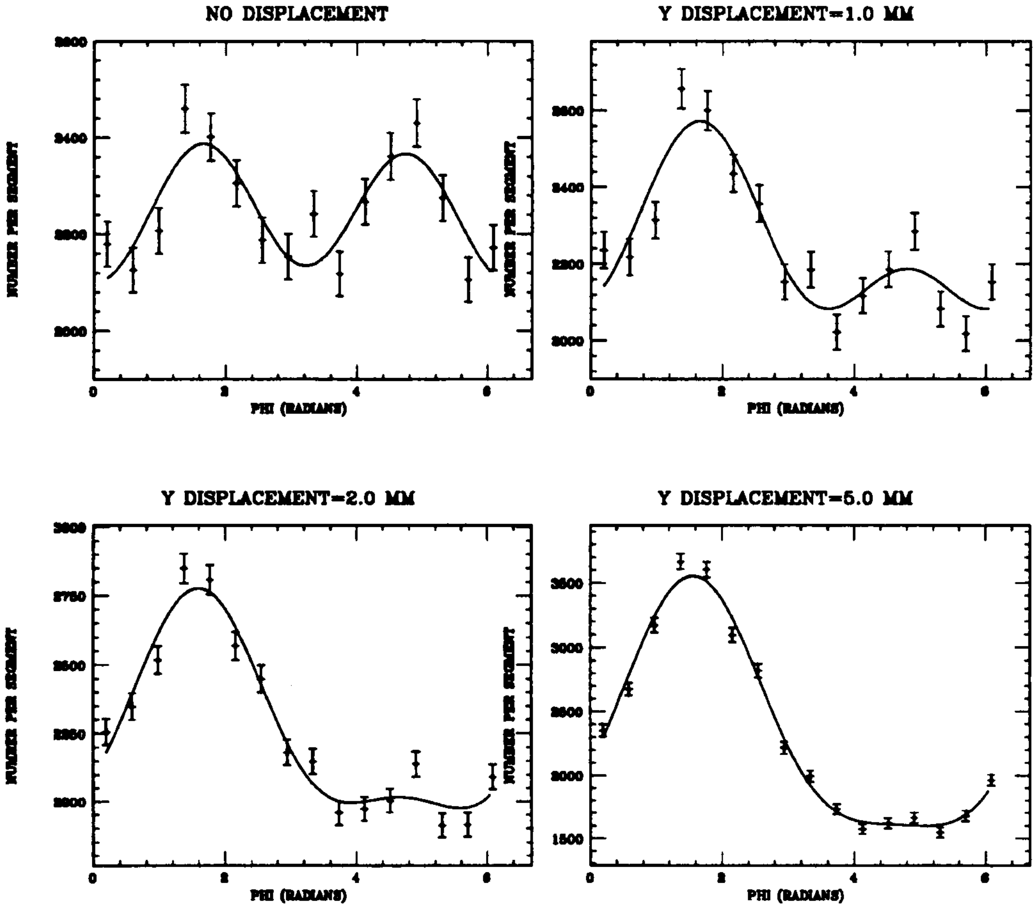

Figure 46: Monte Carlo phi distribution with no displacement, and y displacements of 1 mm, 2 mm, and 5 mm.

for displacements in the y direction of 1, 2 and 5 mm.

The second term in the parameterization describes the effect at 90° and 270° of an undisplaced module due to the gap, while the third term describes the effect of the displacement. The fit parameter "E" gives the direction, in radians, of the line of displacement. Monte Carlo shows that D/A can be related to the magnitude of the displacement, d, by fitting to $D/A=ad+bd^2$. To find the relationship between the magnitude of displacement d and D/A, a series of runs are made using Monte Carlo data with various displacements. Figure 47 shows d vs. D/A for these runs, for displacements in the x direction. The resulting curve fits well to the function $D/A=ad+bd^2$, with the fit parameters $a=0.0765 \pm 0.004$ and $b=0.00111 \pm 0.00095$. These studies were done for 100,000 BHLUMI events by displacing the vector for the e^+ or e^- and studying the phi distributions as a function of displacement. The azimuthal distributions from data for the North and South luminosity monitor were fit to the above equation and the displacement in the radial direction was determined. After determination of the direction and magnitude of the displacement, this displacement is inserted in the Monte Carlo, and the number of events in the precise-precise region before and after the displacement is determined. The difference in the number of events is used to compute a correction factor and thus the effect on luminosity for this displacement is determined. The azimuthal distributions for the data in the North and South LMSATs are shown in Figure 48. The results of the fit indicated that the North LMSAT was displaced by:

$$0.23 \text{ mm} \pm .06 \text{ mm along the direction } \phi = 199° \pm 13.4°$$

and the south LMSAT was displaced by:

$$0.79 \pm .06 \text{ mm along the direction } \phi = 262° \pm 3.4°.$$

The perpendicular displacement was relatively stable over the entire run period. This was determined by dividing the run into blocks of 20,000 events and determining the displacement for each block separately. The results indicated that there was no significant change in the displacement over time.

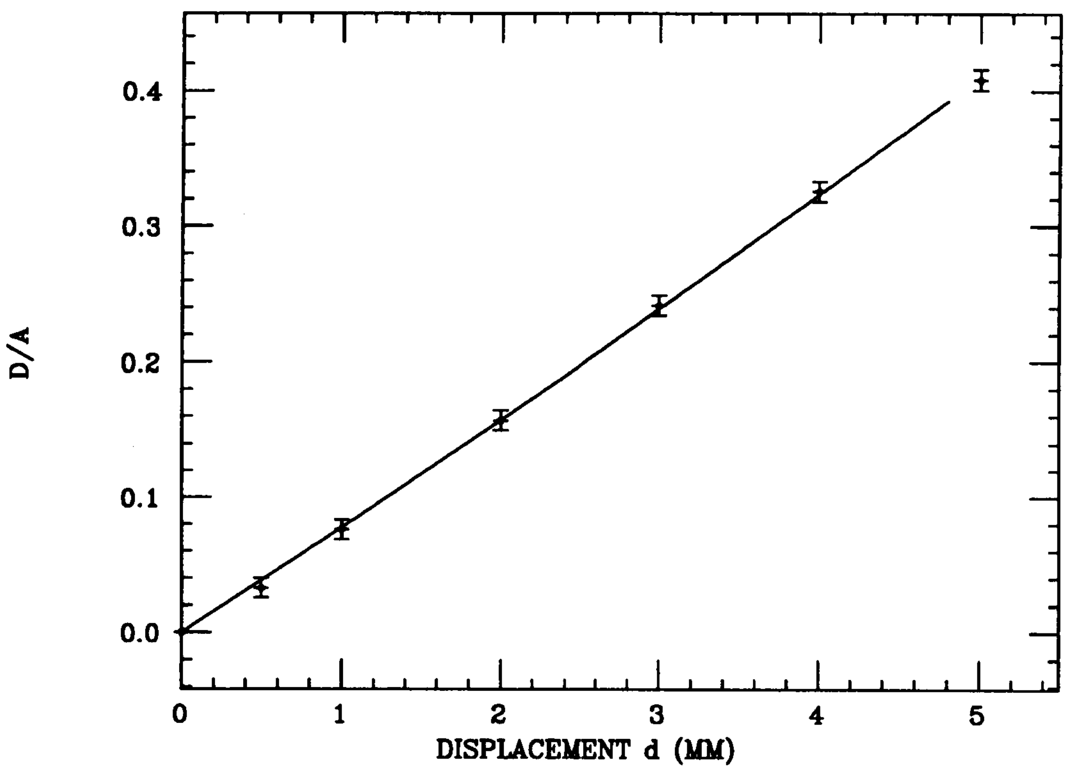

Figure 47: Fit of D/A to d, the displacement in the x direction for Monte Carlo events.

SOUTH

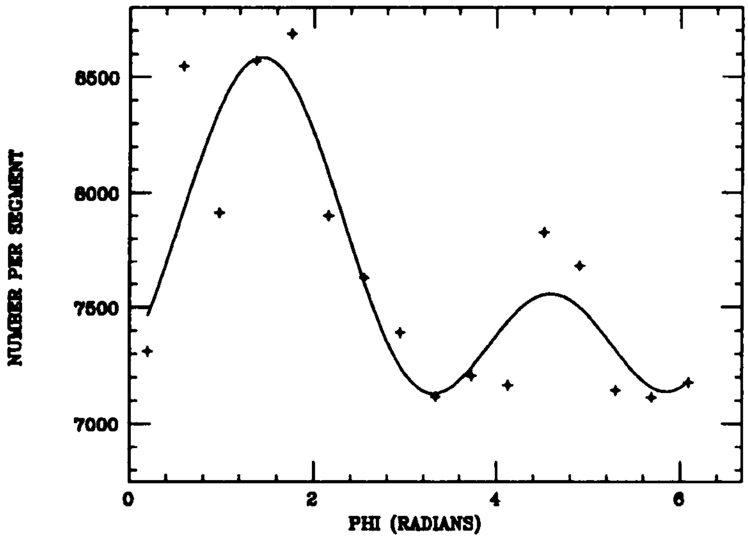

NORTH

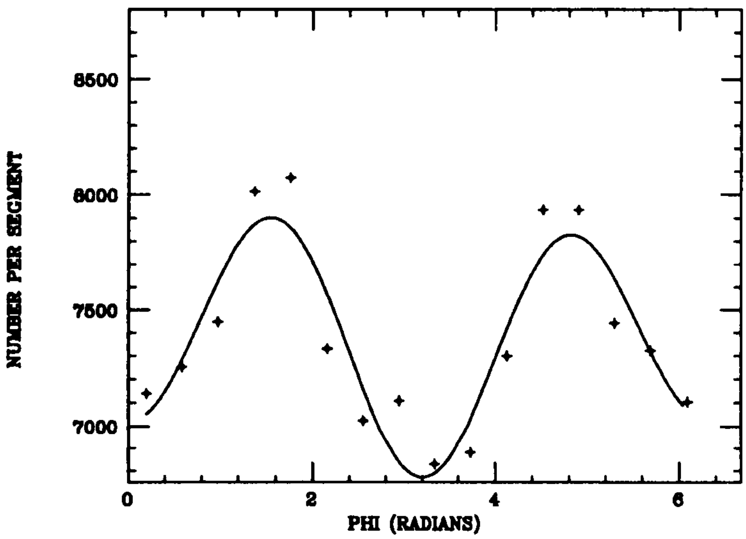

Figure 48: Distribution of phi of maximum tower for all 1993 data events, South (top) and North(bottom).

It is also clear from the data that in addition to displacement of each LMSAT module perpendicular to the beam, the interaction point was not centered between the two modules. This displacement along the z axis is indicated by the imbalance in the number of gross-precise events with the North end in the precise region (7,364) vs. the number with the South end in the precise region (10,614). The ratio between these in the data remained 0.69 after correction for radial displacement. With no displacement, this ratio would be 1:1. When the measured perpendicular displacements were inserted in the Monte Carlo, the ratio between the number of gross-precise events with precise side North and the number with precise side South was 0.996, compared to 0.69 in the data. To utilize the imbalance in the ratio of gross-precise events to measure the z displacement, we define an imbalance I:

$$I = \frac{N_{precise\ S} - N_{precise\ N}}{N_{precise\ S} + N_{precise\ N}}$$

where, for example, $N_{precise\ S}$ means the number of events in the precise region in the South LMSAT with the North end in the gross or precise region. I should be zero if the interaction point is centered between the two luminosity monitor halves. Monte Carlo data with several displacements of the interaction point in z is used to relate I to the displacement Δz of the interaction point. For small displacements it is an almost linear relationship of the form I=aΔz + bΔz^2, the quadratic term being quite small. Figure 49 shows I vs. Δz and the fit, where the fit values were a=0.00199 $\pm$ 0.00024 and b=$-0.9501 \times 10^{-5} \pm 0.255 \times 10^{-4}$. Given I from the data, which was 0.01362, the effective amount of displacement of the interaction point Δz, can be determined. Since the distance between the North and South LMSAT modules is known to an accuracy of about 1 mm, we assume that this distance is fixed and the effective interaction point is off centered. For the 1993 data set, the effective interaction point was closer to the North LMSAT by:

$$\Delta z = 7.1\ \text{mm} \pm 0.5\ \text{mm}\ .$$

When this displacement and the radial displacement are included in the Monte

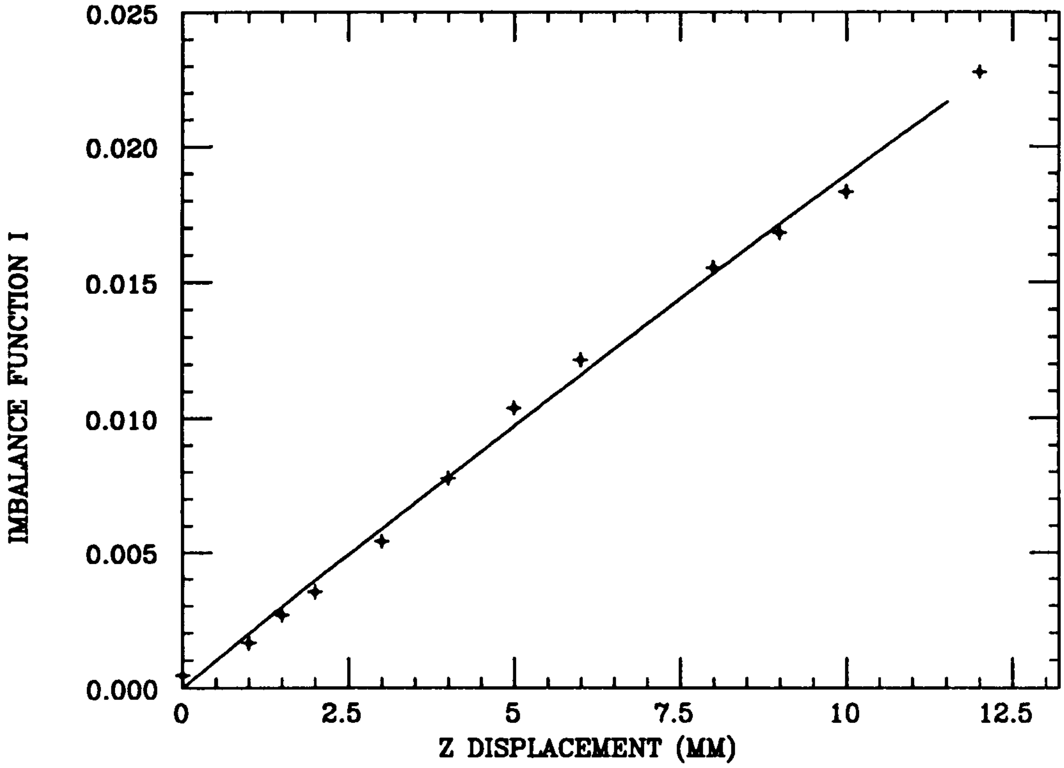

Figure 49: Fit of the function F vs. the z displacement.

Carlo, it is determined that an overall correction to the luminosity of 2.55% $\pm$ 0.23% is required. This is equivalent to the addition of 2810.9 $\pm$ 254.0 events to the precise-precise sample.

For the gross-precise method, small displacements of the order measured cancel to first order; however, a small error in the luminosity is still introduced due to the displacement. The procedure described above is used for inserting the displacement in the Monte Carlo, but only the number of gross-precise weighted by one half plus precise-precise events is compared before and after the displacement. The resulting small effect is treated as an uncertainty. This uncertainty is 0.062% of the total precise-precise plus half the gross-precise events, or 74.2 events.

A further check of how well the Monte Carlo, with the displacements, compares with the data can be made by looking at the ratio of the total number of gross-precise to the total number of precise-precise events in the Monte Carlo with the displacements included. The Monte Carlo result is 0.160, and for the actual data this ratio is 0.163. With no displacement at all a ratio of 0.124 is predicted. With no displacement, gross-precise events are due only to radiative events, and the ratio results from the number of radiative events predicted from QED and the geometry of the acceptance regions. Non-radiative Bhabhas are collinear, i.e. theta and phi are the same on both North and South, so that a Bhabha which does not have both ends in the same theta ring is either a radiative event, or a result of LMSAT displacement, or both. Displacements can cause events which would originally have been a precise-precise event, to become a gross-precise event. Thus a deviation of the ratio of gross-precise to precise-precise events from 0.124 is a good indicator that displacement is present.

5.7 Cross Section Determination

BHLUMI 2.01 is used to calculate the Bhabha cross section in the acceptance region of the SLD luminosity monitor. The BHLUMI Monte Carlo program is described in more detail in Chapter 3. BHLUMI is used to generate Bhabha events in a region larger than the angular acceptance region of the luminosity monitor and also the cross section corresponding to these events. Cuts similar to those used with data are then applied to the four vectors to determine the number of events passing the data cuts and the corresponding cross section for the fiducial region used. BHLUMI explicitly generates multiple photons for the radiative events. Given unlimited computer resources, one would ideally run all BHLUMI events through the full detector simulation program, GEANT 3.11, and apply cuts identical to those used for the data sample. This is a very CPU intensive operation, requiring approximately 90 CPU minutes of IBM 3090 time to simulate a single event.

We have studied the detailed full shower detector simulation for a sample of 4552 events acquired over a period of several years and have used this sample of events to develop a set of acceptance cuts which, when applied directly to the four vectors of the BHLUMI events, approximate well on an event by event basis the results obtained for the full shower events. The fully simulated events were generated using BHLUMI 1.12, but the use of an earlier version of the program does not affect the comparison of vector and full shower cuts. These four vector cuts then permit improved statistical accuracy in the determination of the cross section, as acquisition of a large number of events at the four vector level is feasible.

To determine suitable four vector cuts, we study the 4552 events for which we have both the vector and full shower information. This set contains 1784 events classified as precise-precise events when the data cuts are applied to the full shower events and 221 classified as gross-precise events. The remaining events are events with both ends in the inner ring or events which fail one or more of the cuts such as the energy cut or $\Delta\phi$ cut. The vector cuts are simplest when there are no radiated photons in the luminosity monitor, since then one need only consider one vector per side in the luminosity monitor, corresponding to the e^+ and e^-. If photons are present, the following algorithm is used. If a photon is within 15 mrad of the e^+ or e^- vector, the vector for this photon is combined with the e^+ or e^- vector, and their momenta are added vectorially. A photon 15 mrad from the e^+ or e^-, approximately within one tower, would create a shower which would overlap with the primary shower for the e^+ or e^- and be difficult or impossible to distinguish as a separate shower. If more than one photon meets the criteria, a cumulative sum is done. If the photon is well separated from the e^+ or e^-, it is distinguishable as a second cluster, and the decision on which vector to use to classify the event as gross or precise is based on the particle with the higher energy.

After the vectors are combined, the luminosity monitor tower that the vector intersects is determined. Since the shower does not achieve its maximum energy longitudinally until it has traveled several radiation lengths into the luminosity monitor, it is therefore possible for the tower with maximum energy to be different from the tower the incident e^+, e^- or γ hit on the front face. The initial vector, projected throughout the length of the luminosity monitor, may intersect different towers at different depths due to the non-projective tower structure. The optimum value of z (which measures depth into the LMSAT) was chosen to minimize differences between vector and full shower predictions. A nominal depth was chosen to give the closest agreement on an event by event basis between the vector tower prediction and the tower with maximum energy in the full shower version of the event. The best results were obtained for z=108.0 cm, which is on average near the point in the luminosity monitor where the shower achieves its maximum longitudinal energy deposit. Table 4 shows the results for the number of events classified differently by the vector and full shower cuts for three values of z. Note that z=108.0 cm results in the lowest net difference in classification of precise-precise events, as well as the smallest total number of events which disagree in classification. Although this cut allows a larger net difference in classification for gross-precise events, it minimizes the overall number of disagreeing events. Therefore z=108.0 cm is chosen to evaluate where the four vectors intersect the luminosity monitor.

Table 4 shows that when z=108.0, for the precise-precise events, there was a net

Table 4: Classification of events for full shower vs. vector cuts for a total sample of 4552 events.

z(cm)	PP full shwr not vector	PP vector not full shwr	Net change	GP full shwr not vector	GP vector not full shwr	Net change
106	71	32	+39 FS	43	37	+6 FS
108	8	8	0	38	1	+37 FS
110	83	40	+43 FS	50	40	+10 FS

classification difference of zero events, with a total of 16 events that were differently classified. That is, 8 events were classified as precise-precise using the full shower cuts but not by the vector cuts, and 8 events were classified as precise-precise by the vector cuts but not the full shower cuts. For the remainder, out of 1784 classified by the full shower cuts as precise-precise, the vector cuts also classified them as precise-precise. Thus there was a disagreement in classification of $\frac{0}{1784}$ with an error of 0.2% which will be taken into account when determining the Monte Carlo cross section. For the gross-precise events, the agreement is less satisfactory, with a net difference of 31 events out of 190 that disagreed in classification, for a total of 37 such events. For these 37 events, 34 events were classified as gross-precise events by the full shower cuts but not the vector cuts, and 3 events are classified as gross-precise by the vector cuts but not the full shower. This is a disagreement of $\frac{31}{190}$, or 0.16 ± 0.03 for the gross-precise events, with an excess of events in the full shower sample. Since the cuts applied to full shower events treats the Monte Carlo events like data, when the vector cuts are used on a high statistics sample of Monte Carlo vector events to determine the cross section, the number of passing events must be corrected upward by the percentages given above. Failure to make this correction would lead to an 0.8% error in the luminosity.

To determine the cross section corresponding to our acceptance, we generated three samples totalling 1,682,707 BHLUMI 2.01 events, and the total BHLUMI cross section associated with these events. Applying the vector cuts to the events and determining the fraction of the total number of generated events lying in the fiducial region, we obtain the cross section for Bhabha events in our acceptance region. For 1,682,707 BHLUMI events generated at E_{CM}=91.26 GeV and θ_{min}=25.5 mrad, 545,316 are classified by the vector cuts as precise-precise events, and 58,378 are classified as gross-precise events. The correction of 0.0% $\pm$ 0.2% due to the disagreement between full shower and vector cuts is made to the precise-precise events, causing an error of $\pm$ 122.3 events. For the gross-precise events, the correction of 16.32% $\pm$ 3.2% adds 9525.0 $\pm$ 1868.5 events (this number is before weighting the events by 0.5). These results and the total cross section from BHLUMI of σ_{tot}=202.68 $\pm$0.0987 nbarn, yield the cross section for the precise-precise region:

$$\sigma_{PP} = 65.68 \pm 0.18 \text{ nbarn.}$$

The cross section for the precise-precise plus gross-precise region is:

$$\sigma_{GP+PP} = 69.77 \pm 0.21 \text{ nbarn.}$$

However, a further uncertainty is introduced to the Monte Carlo result from the uncertainty in the precise location of the outer acceptance boundary in the luminosity monitor. This boundary is defined by the MASiC, and its position is not known with precision. We take the outer acceptance boundary to be 67 mrad $\pm$ 1 mrad, and take this uncertainty into account by calculating the cross section with an outer acceptance of 66, 67, and 68 mrad. The difference between the cross sections at 67 and 66, and between the cross sections at 67 and 68, contributes an error of .08 nbarn. Combining this error in quadrature with the original error, the final result for the cross section for the precise-precise plus gross-precise region is:

$$\sigma_{GP+PP} = 69.77 \pm 0.22 \text{ nbarn.}$$

It should be noted that the error on the cross section includes the error for the correction for vector cuts vs. full shower cuts.

5.8 Systematic Errors

This section will describe the systematic errors affecting the luminosity measurement. Systematic errors differ for the precise-precise and gross-precise event sample, so the errors for each method will be described separately. The systematic effects have been studied with BHLUMI Monte Carlo events. The corrections described below will be applied to the raw data sample of 110,360 precise-precise events and 17,904 gross-precise events.

5.8.1 Systematic Errors in Gross-Precise Calculation

Dead Tower and Trigger

The effect of the single dead tower in the innermost ring on the South side in EM2 is to cause a slight decrease in the number of events in this region, because an event that hits the dead tower may fail at either the trigger or event selection level. Most events that hit this tower are not lost, as there is sufficient energy in the surrounding towers to allow them to pass the energy cut. The effect of the dead tower was simulated by zeroing out the tower in the full shower events, and recording the number of events lost. In addition, the online trigger code was applied to the full shower BHLUMI events, giving an estimate of the number of Bhabha events lost at the trigger level. The combined effect of the dead tower and trigger loss causes a 2.79% $\pm$ 1.1% loss of gross-precise events and none of the precise-precise events. The correction for this effect is then to add 499.6 $\pm$ 203.9 events to the gross-precise event sample.

Energy Measurement

The energy resolution of the luminosity monitor is described in detail in Chapter 4, section 4.4.1. The effect of the 0.8 mm FR-4 mounting boards in front of or behind the silicon in alternate octants is described in detail, along with the the correction made for the different energy response of the octants of one configuration vs. the other. In addition, one octant in North EM1 had two layers disconnected, which resulted in lower energy in that octant. Events which have low energy and also fall in an octant with a lower energy response, may be lost at the trigger level. This effect is simulated by correcting the full shower Monte Carlo events for the effect of the FR-4 and determining if any additional events then pass the online trigger cuts. We find that $1.41\% \pm .81\%$ of the gross-precise events are lost. This requires the addition of 252.1 ± 145.5 events to the gross-precise sample.

SLC Background

The primary source of background in the LMSAT is the beam noise from SLC. This background is largest at low angles, close to the beampipe, so the fiducial region cut effectively reduces it. The noise is primarily of three types: 1) Bremsstrahlung, where the e^+ or e^- bent by the final focus magnets emit low energy photons, which scatter off elements of the final focus apparatus, 2) beam wall events where the e^+ or e^- interact with the beam pipe, and 3) flyers, a source of background not understood in detail which occur when the beam is missteered. Unlike a storage ring where the beam is injected at the beginning of the fill, with noisy initial conditions which quickly become quieter, at the SLC the beam is effectively injected on every pulse, so typical backgrounds are considerably higher. The effect of this noise on identifying Bhabha events is twofold. One effect is for noise clusters to appear in an energetic back-to-back cluster configuration, and simulate an actual Bhabha. Additionally, noise superimposed on an actual Bhabha can result in its misclassification as precise-precise or gross-precise or cause it to fail the cut requiring the cluster energy to be less than 125 GeV. Figure 50 shows the distribution of total energy in the LMSAT in the North and South, for a set of 45,724 luminosity weighted random events from the 1993 run. These plots of total energy do not indicate whether the noise was concentrated in a localized area, or was spread throughout the LMSAT. Figure 51 shows the distribution of cluster energy, for the same events, where a cluster is formed around the tower with maximum

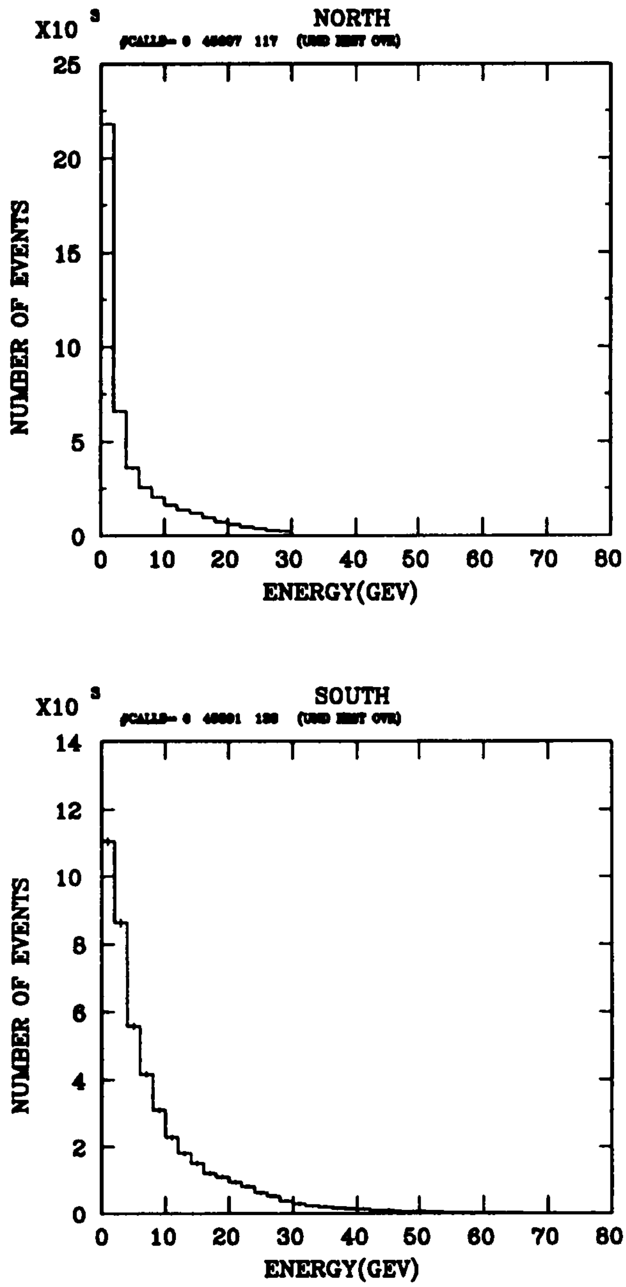

Figure 50: Distribution of total energy in North and South LMSATs for random background events.

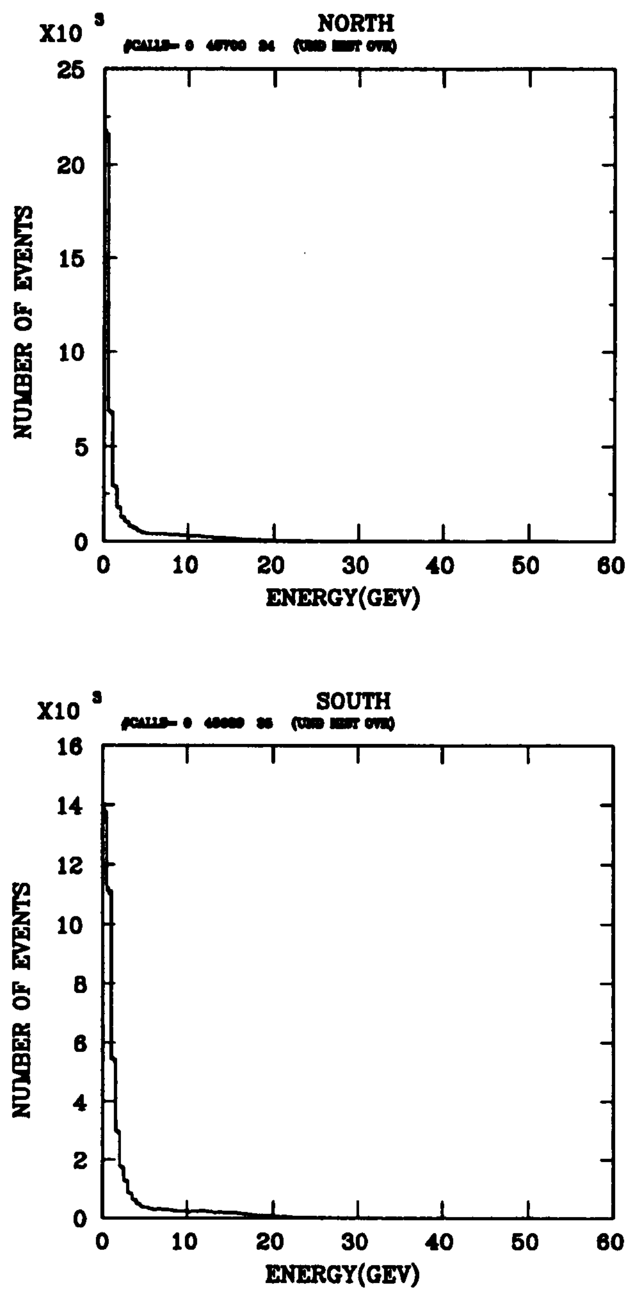

Figure 51: Distribution of cluster energy in North and South LMSATs for random background events.

energy in the same way as for Bhabha clusters, using the maximum energy tower plus adjacent towers. Figure 52 shows a scatterplot of North cluster energy vs. South cluster energy. These plots indicate that about 4% of the random events have a noise cluster greater than 15 GeV. None of these events passes the Bhabha selection cuts, since they fail other cuts besides the cut on energy. In order to see which areas of the LMSAT are most affected by the beam noise, Figure 53 shows a scatterplot of the cluster energy described above vs. the phi coordinate of that cluster. The noise is most predominant along the vertical axis with respect to the beam, near 90° and 270°. The concentration of events in the North monitor near $\phi = 200°$ is due to a subset of channels with small but persistent and uniform electronic noise. Figure 54 shows the theta distribution of the noise clusters, which shows that most of the noise is concentrated in the inner ring. The scatterplots contain only a subset of the random events, for clarity. Every fourth event of the random event sample is plotted.

The effect of noise clusters which simulate Bhabha clusters was examined by studying Bhabha candidates which passed the energy cuts described in section 5.4.2 but were not required to pass the $\Delta\phi$ cut. A different type of $\Delta\phi$ cut was applied, following a technique suggested by Kevin Pitts, which required $\Delta\phi$, measured in towers, to be zero, $\pm$ one tower. This resulted in a small sample which was convenient to hand scan since most real Bhabhas have a $\Delta\phi$ close to 180°, and only a small number of highly radiative events have $\Delta\phi$ close to zero. When radiative events are removed, the remaining events are due to noise. We use this number of noise events to estimate the contamination in the luminosity Bhabha sample from noise events being mistaken for a good Bhabha by assuming that as many noise events had $\Delta\phi = 180° \pm 1$ tower, as had $\Delta\phi=0 \pm 1$ tower. This procedure overestimates the contamination, since the noise location in the North and South LMSATs is either above the beam line on both sides, or below on both sides more often than being 180° apart in phi. Upon hand scanning these events, we find zero false precise-precise events and 39 false gross-precise events. This contributes

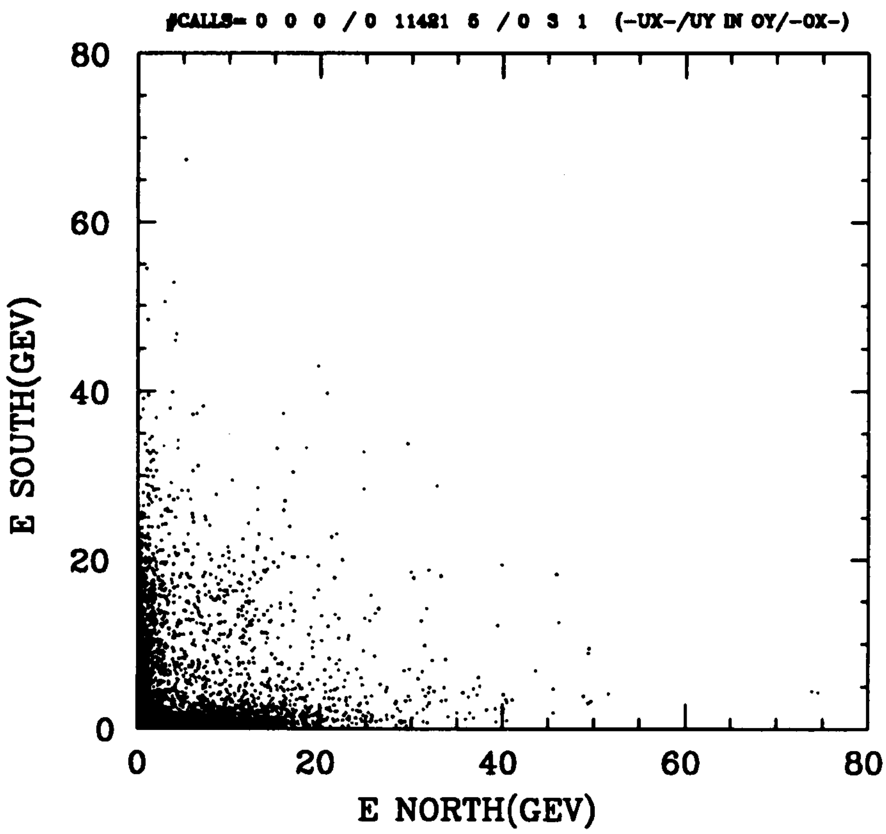

Figure 52: North cluster energy vs. South cluster energy for random background events.

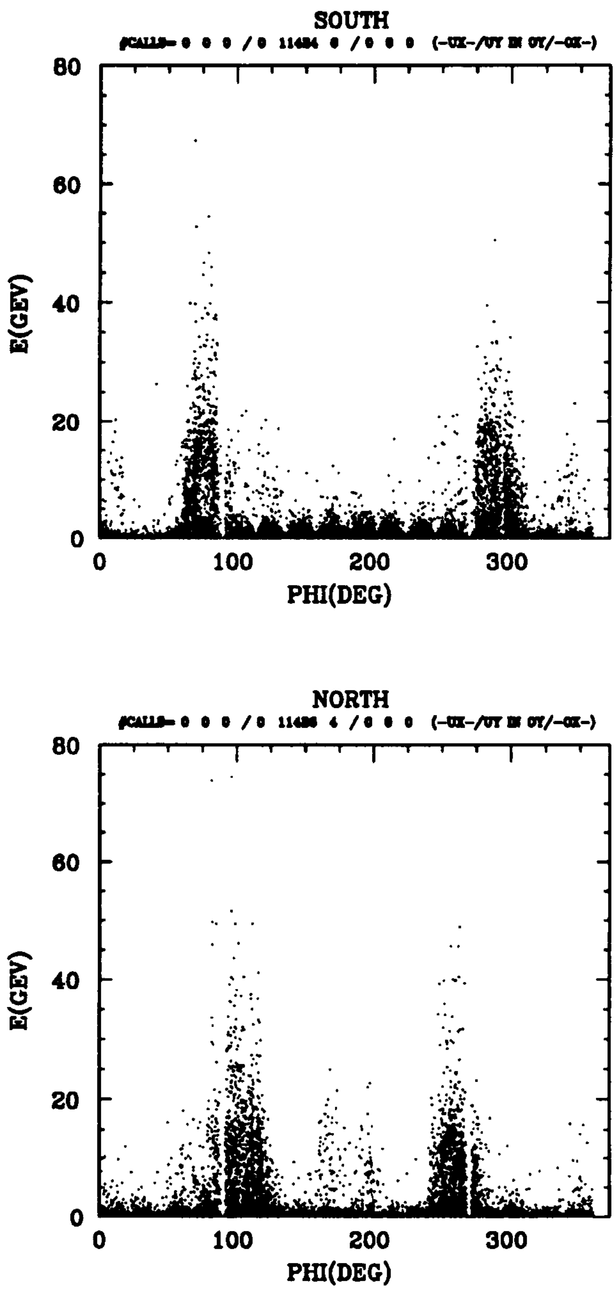

Figure 53: Cluster energy vs. phi in North and South LMSATs for random background events.

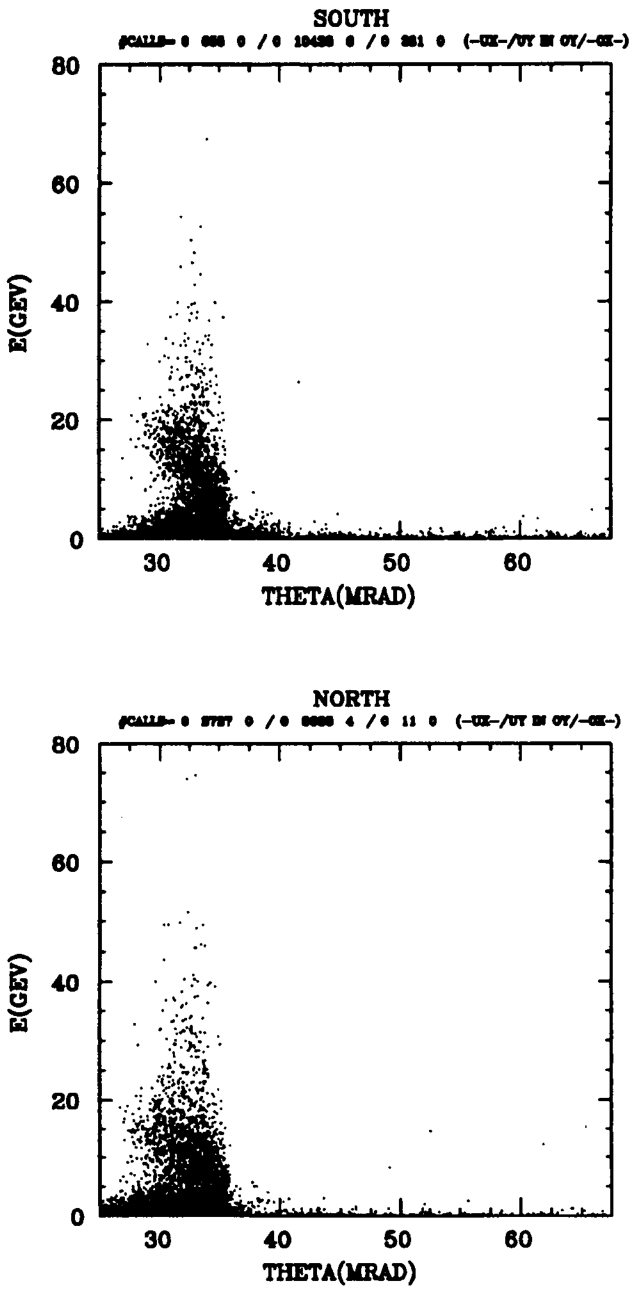

Figure 54: Cluster energy vs. theta in North and South LMSATs for random background events.

a systematic error of $\pm$ 19.5 events to the sample of gross-precise events, since gross-precise events get a weight of 0.5.

Noise can also affect the Bhabha selection if a substantial amount of noise is present with an otherwise good Bhabha. If the true Bhabha cluster is close to the inner ring where noise is present, the noise may cause the tower with maximum energy to incorrectly locate the position of the Bhabha. Thus a good precise-precise event could be classified as gross-precise or perhaps fail the cuts if the maximum towers were shifted to the inner ring on both ends. Similarly a gross-precise event may be misclassified. If the noise cluster is away from the Bhabha cluster and has larger energy so that it is chosen instead of the real Bhabha, the event may fail the $\Delta\phi$ cut, or be misclassified. This effect has been studied by superimposing the luminosity weighted set of random background events recorded during the 1993 SLD run on the full shower BHLUMI events. Since there are many times more background events than full shower Monte Carlo events, we repeatedly overlaid different sets of background events on the Monte Carlo, until all random events were used. The result was a decrease of 0.21% $\pm$ 0.03% in the number of precise-precise events and a 0.130% $\pm$ 0.065% increase in the number of gross-precise events, when compared to the results with no background. Typically noise causes a precise-precise event to be classified as a gross-precise event, and the correction for this effect requires the addition of 230.2 $\pm$ 31.9 events to the precise-precise sample and the subtraction of 23.2 $\pm$ 11.6 events from the gross-precise sample.

Monte Carlo

The cross section calculation from BHLUMI has four possible sources of error. One is the statistical error on the number of events generated which pass the cuts for events lying in our fiducial region. We have generated 1,682,707 events to which we apply the vector level cuts mentioned previously to get the cross section in our fiducial region, and get 545,316 precise-precise events and 58,378 gross-precise events. More significant is the systematic error introduced by using the simplified set of vector level cuts instead of cuts as used for data on the fully simulated events. The correction to the number of events used to get the cross section for our fiducial region is 0.0% ± 0.2% for precise-precise events and 16.32% ± 3.2% for gross-precise events. The technical precision of BHLUMI itself is another source of error. This error is very small, and has been estimated to be less than 0.1%. Another source of error is higher order physics effects not included in the generator, which is also quite small and calculated to be .18%.

Displacement

A complete description of the effect of displacement of the LMSAT on luminosity was given in section 5.5. The gross-precise method cancels the effects of small displacements to first order, so a systematic correction is not required. However the displacement does cause a small uncertainty of .062% in the total number of precise-precise plus one half the gross-precise events, leading to an error of ±74.2 events.

5.8.2 Systematic Errors Affecting the Precise-Precise Method

Dead Tower

No corrections to the precise-precise event sample are necessary for the effect of the dead tower. Since the dead tower is in the inner ring, a precise-precise event cannot have its maximum energy tower there, by definition. Monte Carlo studies using the full shower events have shown that even if the dead tower is part of a cluster centered in the precise region, no precise-precise events fail the energy cut.

Trigger

The method of testing trigger efficiency was described in the previous section. With the full shower BHLUMI event sample of 1784 precise-precise events, no events failed the trigger, even with the dead tower set to zero. Thus we can say that the trigger efficiency for precise-precise events is greater than 99.9% based on the sample of full shower events available. No correction is made to the precise-precise sample.

SLC Background

No correction is necessary for the effect of noise falsifying a Bhabha event in the precise-precise region. A small correction is necessary for the effect of noise overlaid on top of good Bhabhas which changes the classification of some events. As described in section 5.7.1, this effect caused a 0.21% decrease in the number of precise-precise events, requiring 230.2 $\pm$ 31.9 events to be added to the precise-precise sample.

Energy Measurement

Monte Carlo studies were done with the sample of 4552 full shower events corrected for the effect of the FR-4 in alternating configurations. The online trigger cuts were applied and no additional precise-precise events passed. Thus no correction for this effect is made to the precise-precise sample.

Monte Carlo

A correction of 0.0% $\pm$ 0.22% is necessary due to the four vector cuts which do not precisely duplicate the full shower cuts. This correction is included in the cross section calculation.

Displacement

Section 5.5 described the correction of 2.55% $\pm$ 0.23% which must be made to the precise-precise event sample to correct for the effects of small displacements of the LMSAT modules. This requires the addition of 2810.9 $\pm$ 254.0 events to the precise-precise sample.

5.9 Results

All of the analysis necessary to determine the luminosity has now been described. First the luminosity result using the precise-precise method will be presented. Only the events in the precise-precise region are used for this measurement, and the displacement must be measured and corrected for explicitly. The raw number of precise-precise events is 110,360. The corrections for the effect of displacement and the effect of misclassification of events due to noise are summarized in Table 5, given both in number of events and nbarns^{-1}. The corrections in nbarn^{-1} are obtained by dividing the number of events by the cross section from BHLUMI, 65.68 $\pm$ 0.18 nbarn.

Table 5: Corrections to raw number of precise-precise events

Correction Type	Number of Events	Nbarn^{-1}
displacement	2810.9 ± 254.0	42.79 ± 3.87
noise	230.2 ± 31.9	$3.51 \pm .49$
statistical	± 332.2	± 5.06

Therefore, using the precise-precise method, the luminosity is calculated to be:

$$\mathcal{L} = 1726.5 \pm 5.1_{stat} \pm 3.9_{sys} \pm 4.6_{MC} \ \text{nbarn}^{-1}$$

The alternate luminosity measurement uses the gross-precise method. In addition to the precise-precise events, the 17,904 gross-precise events are used, weighted by 0.5, so the total raw number of events is 119,312.0. The corrections to the raw number of events are summarized in Table 6, where the corrections in nbarn^{-1} are obtained by dividing the number of events by the cross section from BHLUMI for events in the gross-precise plus precise-precise region, 69.77 $\pm$ .22 nbarn. The numbers which only affect the gross-precise sample are shown already weighted by 0.5. The result then for the luminosity is:

$$\mathcal{L} = N/\sigma = 1718.5 \pm 5.0_{stat} \pm 2.2_{sys} \pm 5.5_{MC} \ \text{nbarn}^{-1}$$

Table 6: Corrections to raw number of precise-precise + $\frac{1}{2}$ gross-precise events

Correction Type	Number of Events	nbarn^{-1}
trigger + dead tower	249.8 ± 101.95	3.58 ± 1.46
local hardening	126.05 ± 72.8	1.81 ± 1.04
misclassification	218.6 ± 32.4	$3.13 \pm .46$
noise	± 19.5	$\pm .28$
displacement	± 74.2	± 1.06
statistical	± 345.4	± 4.95

The luminosity measured using the two different methods agrees well within errors. It should be reiterated that the error labeled MC includes the BHLUMI error, the statistical error for the number of BHLUMI events used, and the error for the correction for the difference in vector and full shower cuts.

Chapter 6

Small Angle Radiative Bhabha Scattering

6.1 Introduction

Radiative corrections must be taken into account for a precise calculation of the Bhabha cross section. The precision of luminosity measurements depends crucially on the precision of the theoretical prediction for the cross section, and the BHLUMI Monte Carlo is used at both SLC and LEP for calculation of the Bhabha cross section at low angles. Since BHLUMI explicitly generates multiple photons, it is possible to make a detailed comparison of the radiative events in data with Monte Carlo predictions. The comparison of cross section and event characteristics provides a detailed probe of the QED radiative corrections as implemented in BHLUMI. In addition to the importance of the radiative corrections for obtaining an accurate cross section, it is also useful to test how well BHLUMI compares with data for an understanding of the radiative events themselves. Radiative Bhabha scattering can be a background to other measurements, such as neutrino counting and two photon physics, or in searches for new physics. In this chapter two types of small angle radiative Bhabha events are studied. One type is events with a photon visible in the luminosity monitor. The other type is events with an undetected photon radiated at low angles, inside the beampipe. Photons at angles greater than 68 mrad are not considered.

6.2 Event Selection for Events with Visible Photons in the LMSAT

To obtain a sample of events with an identifiable photon cluster in the luminosity monitor, preliminary cuts are first applied to all events passing the SLD Bhabha trigger. The cuts are identical to those described in section 5.4.2, with the exception that the $\Delta\phi$ cut is not applied. Radiative events will deviate from collinearity and events with high energy photons can deviate substantially. For this reason no restriction is placed on the phi locations of the clusters. The cuts are:

$$\mathrm{E_N} + \mathrm{E_S} \geq 35 \ \ \mathrm{GeV} \tag{6}$$

$$\mathrm{E_N} \geq 15 \ \ \mathrm{GeV} \quad \text{and} \quad \mathrm{E_S} \geq 15 \ \ \mathrm{GeV} \tag{7}$$

$$\mathrm{E_N} \leq 125 \ \ \mathrm{GeV} \quad \text{and} \quad \mathrm{E_S} \leq 125 \ \ \mathrm{GeV} \tag{8}$$

Fiducial region cuts are applied so that at least one cluster has its maximum energy tower in the precise region. Events with both ends in the gross region are not studied as the SLC noise seriously contaminates this sample. The relaxation of the $\Delta\phi$ cut adds an additional set of radiative events to the luminosity sample, which already included some radiative events. Additional cuts are applied to select the events with an identifiable photon cluster, with sufficient energy and separation from other clusters to be distinguishable as a separate cluster.

Photons radiating at small angles with respect to the outgoing e^+ or e^-, will produce a shower indistinguishable as a separate cluster. Criteria were established to locate secondary clusters in a LMSAT module, and determine if they should be classified as a separate shower. An energy cut is placed on the candidate photon cluster, to avoid accepting small noise clusters as photons. Secondary and tertiary clusters are identified for each event. The primary cluster is defined by locating the tower with maximum energy and forming a cluster around it, using all towers adjacent to the tower with maximum energy. The second cluster is defined by finding the largest energy tower not included in the first cluster. This tower is designated as the central tower of the second cluster. Although the centroid of the second cluster cannot be a part of the first cluster, the edges of the shower can overlap, i.e. some towers can be shared by both clusters. This overlap must be taken into account when partitioning the energy between clusters. As described in Chapter 4, the position of the shower is calculated using the energy weighted mean for each cluster and corrected using the "snake" correction and second order parameterized correction, so the energy weighted mean must be corrected for overlap. For overlapping clusters, a fraction $(E_{\mathrm{max\ EM1}} + E_{\mathrm{max\ EM2}})_{\mathrm{cluster\ 2}}/(E_{\mathrm{max\ EM1}} + E_{\mathrm{max\ EM2}})_{\mathrm{cluster\ 1}}$ is computed, which is the ratio of the maximum tower energies of the second cluster to that of the first cluster. When the cluster energy sum is computed for the second cluster, all towers shared with the first cluster have their energies reduced by this fraction, so that the full energy is not added to the second cluster. This adjusted energy is used when computing the energy weighted mean position coordinates for the second cluster. If the second cluster represents a real photon, then the first cluster should have its energy and position corrected for the overlap. However, since a second cluster is computed for all events and may be due to noise or just the edge of the primary cluster, rather than an actual photon, preliminary cuts are applied to the second cluster to determine if it is potentially due to a photon, before correcting the primary cluster. The preliminary cuts applied to the second cluster are as follows:

$$E_{\mathrm{clus\ 2}} \geq 5 \ \ \mathrm{GeV} \tag{9}$$

$$E_{\mathrm{max\ tower\ cluster\ 2}} \geq 1.25 \ \ \mathrm{GeV} \tag{10}$$

$$\theta_{\mathrm{separation}} \geq 15 \ \ \mathrm{mrad} \tag{11}$$

The cut of 5 GeV is used because photons with smaller energy are difficult to distinguish reliably from beam noise. The cut requiring the maximum energy tower to have at least 1.25 GeV serves to eliminate cases where the second cluster is formed from the edges of the primary shower, when fluctuations cause it to be unusually wide. The cut on $\theta_{separation}$, the space angle between clusters, ensures that the second cluster is far enough from the first cluster to be distinguishable. If the second cluster passes the cuts it is assumed to be a good candidate for a photon, and if it overlaps the first cluster, the energy and position of the first cluster are corrected for the overlap before the final cuts are applied. Energy and position coordinates are recomputed for the first cluster, with the energies of the shared towers now weighted by the appropriate fraction. Thus the energies in the shared towers are divided between the two clusters in proportion to the ratio of the maximum tower energies of the two clusters.

The event is then subjected to a final set of cuts to determine if it will be classified as an event with a distinguishable photon cluster. The final cuts are as follows:

$$E_{clus\ 2} \geq 5 \ \text{GeV} \tag{12}$$

$$E_{max\ tower\ cluster\ 2} \geq 1.25 \ \text{GeV} \tag{13}$$

$$\theta_{separation} \geq 20 \ \text{mrad} \tag{14}$$

$$E_{cluster\ 1} + E_{cluster\ 2} \leq 65 \ \text{GeV} \tag{15}$$

$$\text{acollinearity} > \ 2 \ \text{mrad} \tag{16}$$

$$\text{cluster 2 not in the inner ring (ring 56)} \tag{17}$$

The first three cuts are similar to those previously described, except that the angle of separation between the two clusters is required to be 20 mrad for the final cut. The cut on the energy sum of the first and second clusters helps prevent large noise clusters from being mistaken for a photon. The acollinearity is defined as the complement of the space angle between the vectors in the direction of the primary cluster on each side of the interaction point. Thus a non-radiative event would be back-to-back and have zero acollinearity. Monte Carlo studies show that 97.7%

of all events with a separate photon cluster satisfying the other criteria have an acollinearity greater than 2 mrad. Figure 55 shows the acollinearity distribution of full shower Monte Carlo events which pass all the criteria for having a separate photon, except they are not required to pass the acollinearity cut. This cut also helps eliminate non-radiative events with a noise cluster which might falsify a photon cluster. The requirement that the photon cluster not lie in the inner ring eliminates some good events, but is necessary since beam noise in the inner ring can cause clusters which pass all the other cuts, and appear to be a photon cluster. It should be noted that these cuts are in addition to the initial set of cuts listed at the beginning of this section, which classify the events as gross-precise or precise-precise.

The application of these cuts to the 1993 data sample yields 1045 events with a separate photon cluster of at least 5 GeV. It is important to recognize that it is not possible to distinguish between a photon and an electron or positron cluster in the luminosity monitor, as tracking is not done for particles entering the luminosity monitor. Therefore, the convention is adopted that the smaller of the two clusters found is considered to be the "photon" cluster, even though it may in fact be due to the electron or positron from a highly radiative event where the photon has more energy than the electron or positron. The same convention is applied to the Monte Carlo data, even though in the BHLUMI events the identity of each particle is known.

6.3 Monte Carlo Cross Section for Events with Visible Photons

Having identified the data sample with a distinguishable photon cluster, we compare the data and Monte Carlo predictions. BHLUMI 2.01 was used to generate events and cross sections. The generated events are used to make distributions of acollinearity and photon energy to compare with data. In some instances full

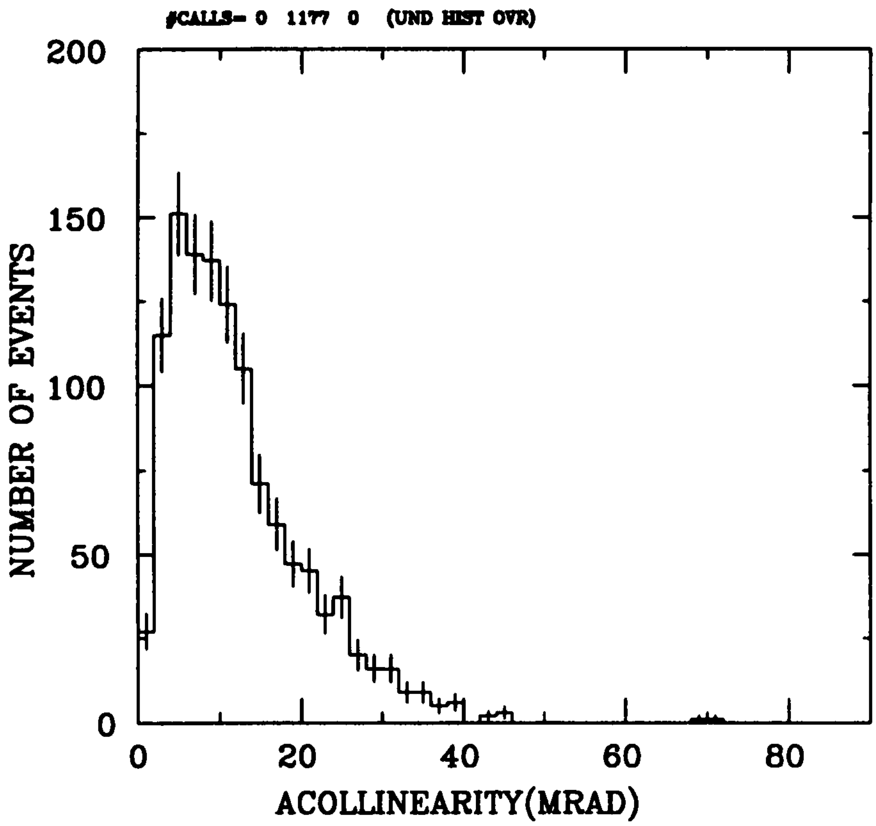

Figure 55: Acollinearity distribution of full shower Monte Carlo events passing all criteria for having a separate photon except for the acollinearity cut.

shower Monte Carlo events are also shown. The full shower events are from BHLUMI 1.12 [11], an earlier version, run with the xmivis setting equal to 0.2, which means that the minimum energy of the electron or positron is 20% of the beam energy.

Computer limitations prevent processing sufficient events through the full shower simulation to get a cross section for this type of event with sufficient accuracy using only full shower events. However, a set of events preselected to have a photon in the luminosity monitor has been processed through the full shower simulation so that vector cuts could be tuned to closely match full shower results, as was done in Chapter 5 for the luminosity measurement. The initial selection applied to the four vectors is described in Chapter 5, except that no cut is placed on $\Delta\phi$. Additional cuts are applied to select events with a well separated photon. For events with photons present, the vectors for all particles within 15 mrad of each other on a given end of the LMSAT are combined into one vector. Vectors more than 15 mrad away from other vectors or combination of vectors are not combined. In the following description of cuts the term vector will be used to refer to the vectors after all necessary combinations are made. The vector with the largest energy on each side of the interaction point is treated as the primary "cluster" and if there is a second vector on a given side it is treated as the secondary "cluster". Particle identification from BHLUMI is not used, since particle identification is not possible in data. Cuts are then applied to the vectors, to select events with a photon that should also be distinguishable if it were a data event. The following cuts are made to the vector events:

$$E_{2nd\text{ ``cluster''}} \geq 5 \text{ GeV} \tag{18}$$

$$\theta_{separation} \geq 20 \text{ mrad} \tag{19}$$

$$\text{acollinearity} > 2 \text{ mrad} \tag{20}$$

$$\text{``cluster'' 2 not in the inner ring} \tag{21}$$

The photon energy may be larger than the electron or positron energy in a highly radiative event. In that case the smaller e^+ or e^- is reclassified as the "photon" cluster, as is done with real data. Therefore the photon energy is always less than half the beam energy using the four vectors, and the same is true for data aside from energy resolution smearing.

A set of 1309 BHLUMI events with a photon at least 15 mrad from the electron or positron, and at least 3.5 GeV in energy, was processed through the full shower simulation, and used to compare the vector cuts and the cuts applied to showers as with data. A comparison of the number of events passing both the vector cuts and the full shower cuts gives a measure of the efficiency of the full shower cuts for detecting the photons. From a sample of 1309 events, 568 pass the four vector cuts, and of these, 486 also pass the full shower cuts. Thus 82 events are lost by the full shower cuts. Of the remaining 741 events that fail the four vector cuts, 45 pass the full shower cuts. These represent a background from non-radiative events or events with a photon too small or too close to the e^+ or e^- to satisfy the vector cuts but which pass the cluster cuts due to position or energy resolution smearing. The net effect of these corrections is that too few events pass the cluster cuts, compared to the results using the vectors, so in order to compare data with Monte Carlo the number of events passing cuts in data must then be corrected upward by 7.0% $\pm$ 2.1%. This correction is independent of background due to beam noise.

The expected cross section based on BHLUMI for events with a separate photon not in the inner ring, is calculated using a set of 1,682,707 BHLUMI 2.01 events, the set used to determine the Bhabha cross section for the luminosity determination. When the four vector cuts for separate photon events were applied to this set of events, 5521 events passed the cuts. In this case, before applying cuts for separate photon events, all vectors were corrected for displacement in the luminosity monitor for the 1993 run. The displacement determination is described in detail in section 5.5.1. The separate photon events are a mixture of gross-precise and precise-precise events and the effect of the displacement must be taken into account. The vector events used to determine the cross section are displaced and the correction for displacement is thus incorporated in the cross section determined from BHLUMI.

The total cross section provided by BHLUMI for the set of 1,682,707 events was $\sigma_{tot} = 202.68 \pm 0.0987$ nbarn. The cross section for the separate photon events is then given by taking the corrected fraction of events passing the separate photon cuts, and multiplying by the total cross section:

$$\sigma_{\substack{\text{sep photon} \\ \text{BHLUMI}}} = 0.665 \pm .009 \ \ \text{nbarn} \tag{22}$$

A further uncertainty is introduced to the Monte Carlo result from the uncertainty in the precise location of the outer acceptance boundary in the luminosity monitor, as described in section 5.7. The uncertainty introduced here is 0.023 nbarn. Combining this error in quadrature with the original error, the final result for the BHLUMI cross section for separate photon events is:

$$\sigma_{\substack{\text{sep photon} \\ \text{BHLUMI}}} = 0.665 \pm .025 \ \ \text{nbarn} \tag{23}$$

6.4 Comparison of BHLUMI With Data for Separate Photon Events

The following sections compare data with BHLUMI predictions for events with a separate distinguishable photon in the LMSAT. Comparisons of cross section, acollinearity distribution, and photon energy distribution are made. The cross section for events with a separate photon in data is given by $\sigma_{sep\ \gamma} = N_{sep\ \gamma}/\mathcal{L}$, where $N_{sep\ \gamma}$ is the number of separate photon events counted in the data and $\mathcal{L}$ is the luminosity. The number of events observed in the data is 1045, and the luminosity from Chapter 5 using the average result from the two methods of luminosity measurement is:

$$\mathcal{L} = 1722.49 \pm 7.79 \ \ \text{nbarn}^{-1}.$$

Some systematic effects affecting the data make corrections necessary before comparison to the BHLUMI predictions. The corrections are described in the following section.

6.4.1 Systematic Effects for Separate Photon Events

Systematic effects affecting the luminosity measurement are present for the radiative Bhabha events, but are not necessarily identical to those for luminosity events, since different cuts are used to obtain the radiative events, e.g., no $\Delta\phi$ cut. The radiative sample contains both precise-precise and gross-precise events, so systematic effects affecting both types of events are relevant here.

Dead Tower and Trigger Efficiency

The combined effect of the one dead tower in the 1993 run and the slight inefficiency of the trigger causes a small decrease in the number of separate photon events detected. This effect was studied by using a sample of 2191 full shower radiative BHLUMI events. The energy in the dead tower is set to zero, and the online trigger is applied, yielding 616 events which pass the cuts compared to 622 when the dead tower is not set to zero and passing the trigger is not required. Thus the trigger and dead tower combine to cause a loss of 1.0% $\pm$ 0.40% of the events. The correction adds 10.2 $\pm$ 4.2 events to the data sample.

SLC Noise

Beam noise mixed with a real Bhabha may cause the event to appear to have a separate photon, if the noise cluster is misidentified as a photon. Excluding events with a photon candidate in the inner ring eliminates much of the effect of noise, but the remaining effect was studied by overlaying a sample of luminosity weighted random events from SLD onto 2191 full shower radiative BHLUMI events before applying the separate photon cuts. The net effect of the noise is to cause extra events which do not really have a separate photon to pass the cuts. The correction required reduces the data sample 2.1 % $\pm$ .13%, which is 21.5 $\pm$ 1.5 events.

Energy Measurement

The data were corrected for the local hardening effect before applying cuts for separate photons, but some events are lost at the trigger stage due to this effect. This effect was studied by using the sample of 2191 full shower radiative events without correcting for the local hardening effect, and flagging the events that fail the trigger. These same events are then corrected for the local hardening effect and the number that pass the trigger and the separate photon cuts after the correction represent the percentage of events lost in data at the trigger stage. This result requires the data sample to be corrected upward by 0.33% $\pm$ 0.23%, which is 3.4 $\pm$ 2.4 events.

Cut Efficiency and Background

The data must be corrected for the net effect of the efficiency of the cuts and background from non-radiative events or events which do not meet the criteria of the vector cuts. The net effect is that too few events pass data cuts compared to vector cuts, so the data must be corrected upward by 7.0% $\pm$ 2.1%, which is 72.8 $\pm$ 22.3 events.

Monte Carlo

As described in Section 6.3, the Monte Carlo cross section was corrected for the effect of displacement and the uncertainty in the outer acceptance boundary.

6.4.2 Results of Cross Section Measurement

The measured cross section for separate photon events is obtained by dividing the corrected number of separate photon events in data by the measured luminosity. The raw number of events is 1045. Table 7 summarizes the corrections made to the data. Using the average luminosity measurement, $\mathcal{L} = 1722.49 \pm 7.79\ \ \mathrm{nbarn}^{-1}$,

Table 7: Corrections to raw number of separate photon events

Correction Type	Number of Events	nbarn
trigger and dead tower	$+10.2 \pm 4.2$	$+0.0061 \pm 0.0024$
local hardening	$+3.43 \pm 2.4$	$+0.0020 \pm 0.0014$
SLC noise	-21.5 ± 1.5	$-.0124\pm 0.00088$
cut efficiency/background	$+72.8 \pm 22.3$	$+0.0423 \pm 0.013$
statistical	± 32.3	$\pm .019$

the cross section for separate photon events is:

$$\sigma_{sep\ photon} = 0.644 \pm .019_{stat} \pm 0.013_{sys} \pm 0.003_{lum} \ \text{ nbarn}.$$

This agrees within errors with the predicted cross section from Bhlumi, which is

$$\sigma_{\text{BHLUMI}} = 0.665 \pm 0.025 \quad \text{nbarn}.$$

6.4.3 Acollinearity

Comparison of the acollinearity distribution for the Monte Carlo and data samples is another test of how well BHLUMI describes the data. Aside from resolution smearing and small displacements of the LMSAT modules, only radiative events are acollinear - that is, the electron and positron do not emerge at the same angles on each side of the interaction point. Figure 56 shows the acollinearity distribution for all events in the data passing the cuts for luminosity Bhabhas. BHLUMI events passing the equivalent four vector cuts are also shown. It is clear that the measured acollinearity distribution is wider than the Monte Carlo and that full shower events do not simulate the distribution well at small acollinearities. The agreement is best for acollinearities above ≈ 5 mrad. For very small acollinearities the position resolution has a greater effect. Figure 57 shows the acollinearity distribution for data and BHLUMI for the events with an identifiable separate photon of at least 5 GeV. Both full shower BHLUMI events and vector events are shown. It can been seen that the BHLUMI distribution reproduces the data distribution rather well for the separate photon events.

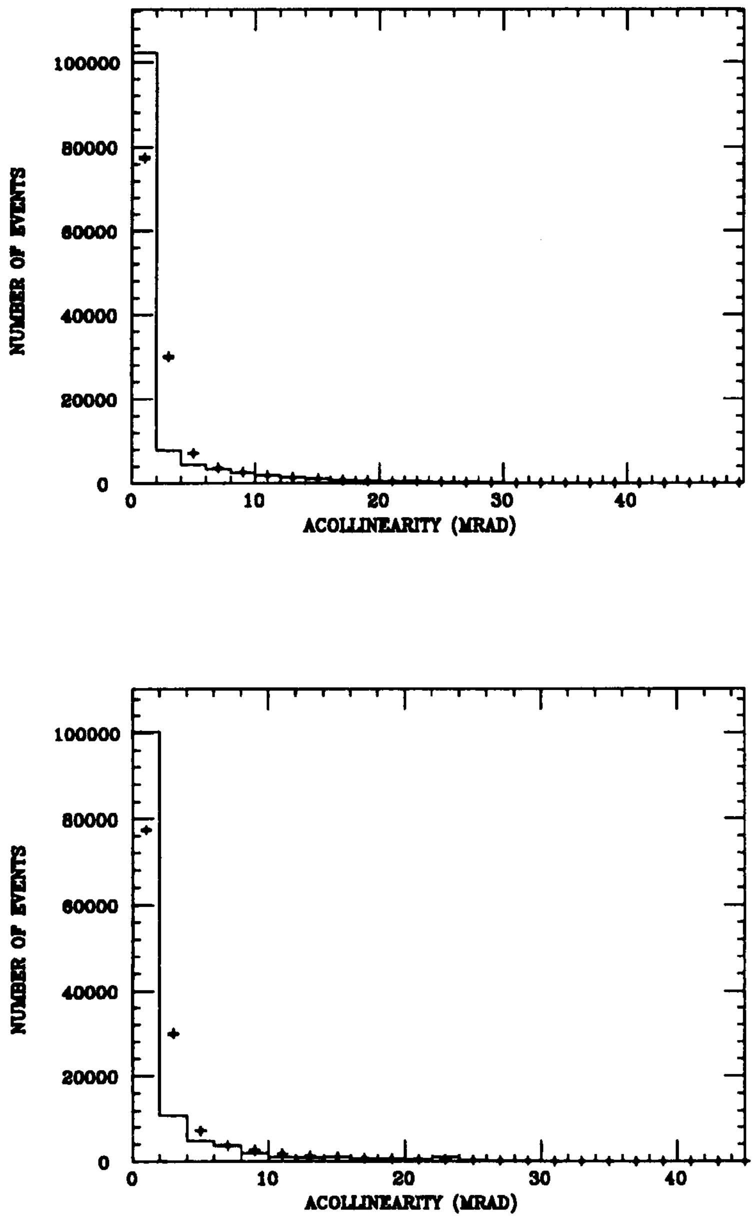

Figure 56: Acollinearity distribution of all luminosity Bhabhas. The histogram in the top figure is Monte Carlo vector events; the points are data. Monte Carlo is normalized to the data, which has 128,264 events. In the bottom figure 2005 full shower Monte Carlo events are shown in the histogram, normalized to data.

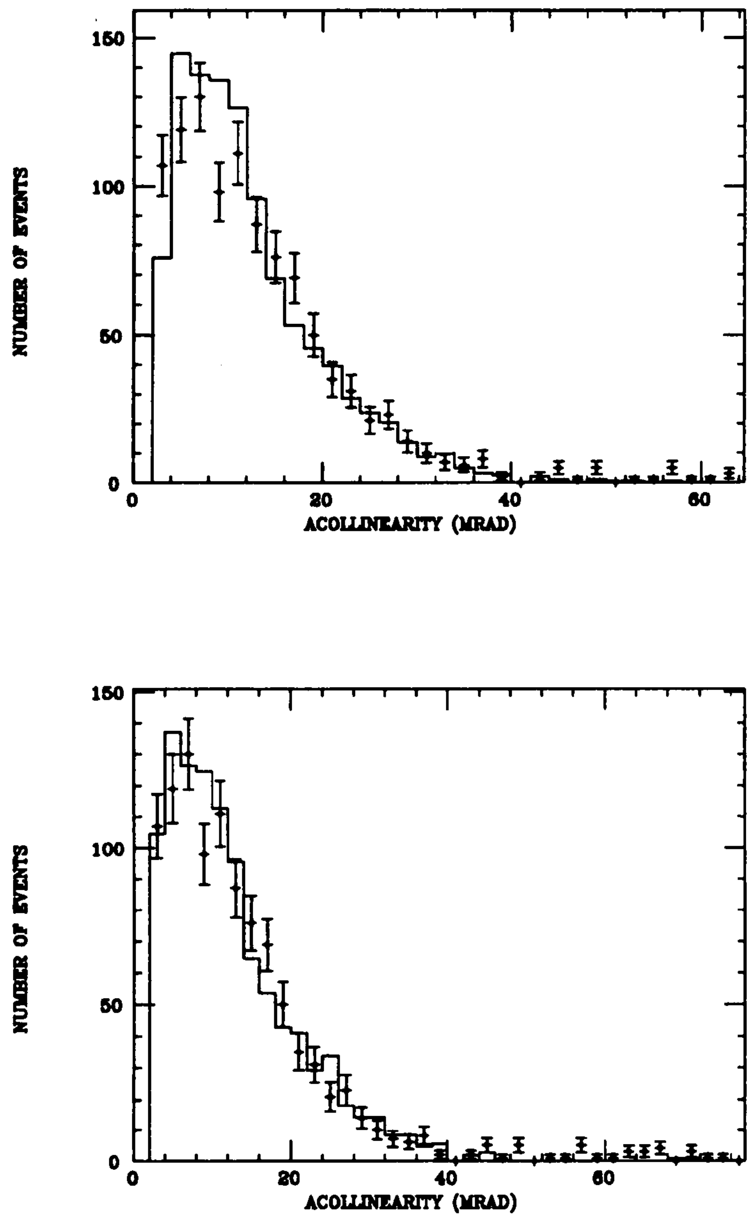

Figure 57: Acollinearity distribution of separate photon events. The top figure shows vector Monte Carlo in the histogram compared to data. The bottom figure shows full shower Monte Carlo in the histogram compared to data. Monte Carlo is normalized to the 1045 data events.

6.4.4 Photon Energy

BHLUMI predictions for the photon energy distribution are compared with the observed data. Since photons cannot be distinguished from electrons and positrons in the LMSAT, the smaller of the two clusters in data is plotted as the "photon" and the same convention is maintained for the four vectors from BHLUMI. Figure 58 shows the photon energy distribution for data and BHLUMI events, using both full shower and vector BHLUMI events. Figure 59 shows the BHLUMI four vector photon energies with the detector energy resolution folded in to give a more realistic distribution, and the data is replotted as well. It was possible to get a full shower Monte Carlo sample slightly larger than the data sample in this case, and the energy distribution agrees well with the data. Figure 60 shows the energy distribution of the main cluster energy for the events with a visible photon. Both North and South energy distributions are shown, and an entry is made into one of the two plots only for the side having the observed photon. Data and full shower Monte Carlo are shown.

6.5 Radiative Events with Highly Forward Photons

6.5.1 Event Selection

A class of radiative events that can be readily identified are events with a photon or photons radiated at such low angles that they escape down the beampipe and are not directly detected in the luminosity monitor. These events are characterized by acollinearity and missing energy in the luminosity monitor. Figure 61 shows an acollinearity distribution of BHLUMI vector events with a photon of at least 5 GeV down the beampipe (angles less than 28 mrad). The events are classified as gross-precise or precise-precise events but are not required to pass a $\Delta\phi$ cut, and 90.3% of the events have an acollinearity greater than 5 mrad. In contrast,

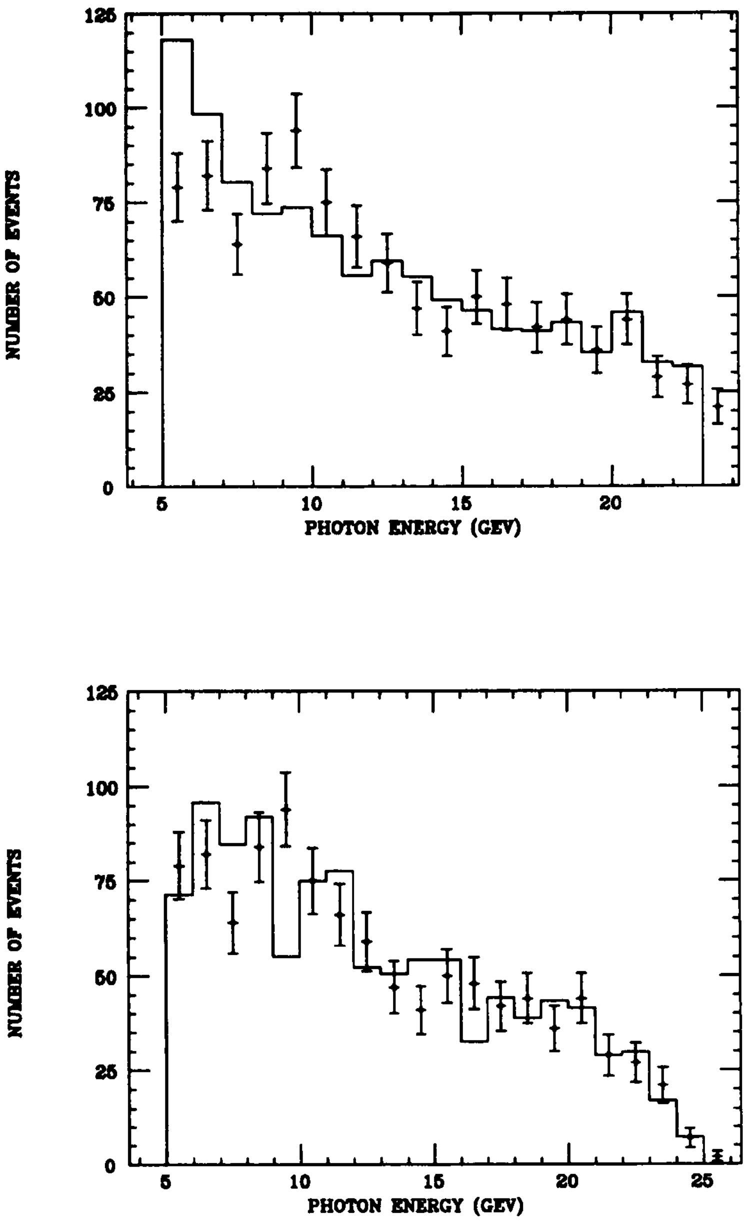

Figure 58: Photon energy distribution for separate photon events. The top figure shows vector Monte Carlo in the histogram compared to the points showing the data. The bottom figure shows full shower Monte Carlo in the histogram compared to data. Monte Carlo is normalized to the 1045 data events.

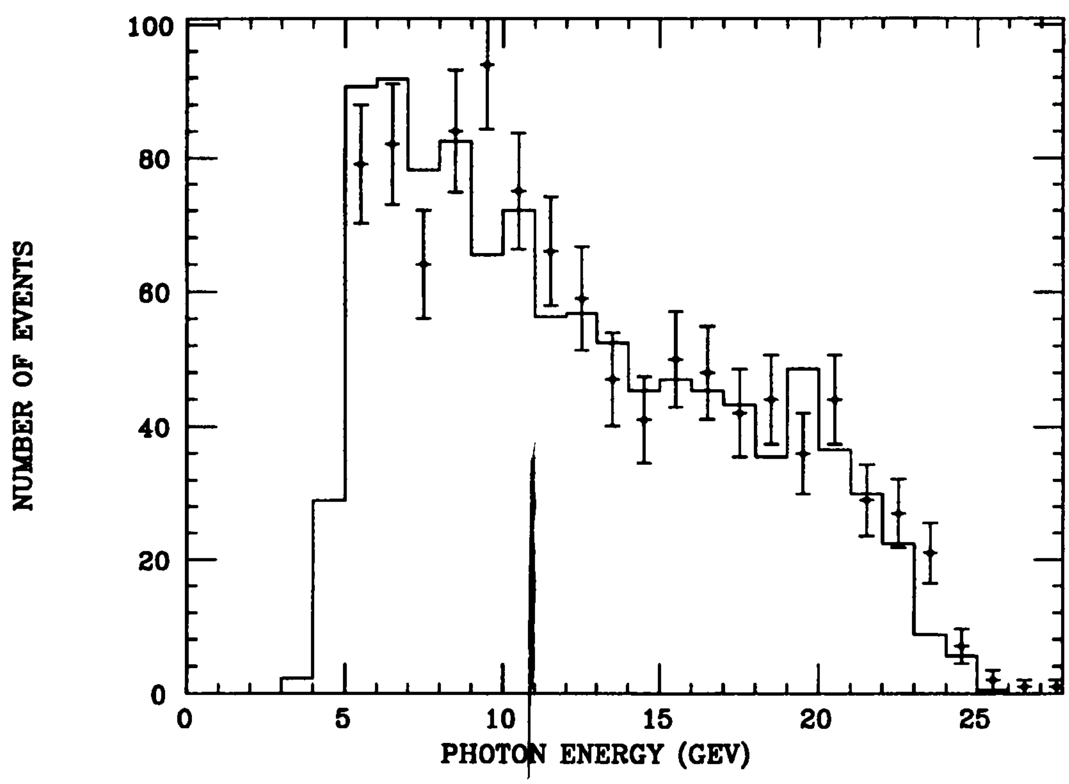

Figure 59: Photon energy distribution for separate photon events. Vector Monte Carlo smeared by the energy resolution is shown in the histogram, the points are data. Monte Carlo is normalized to the 1045 data events.

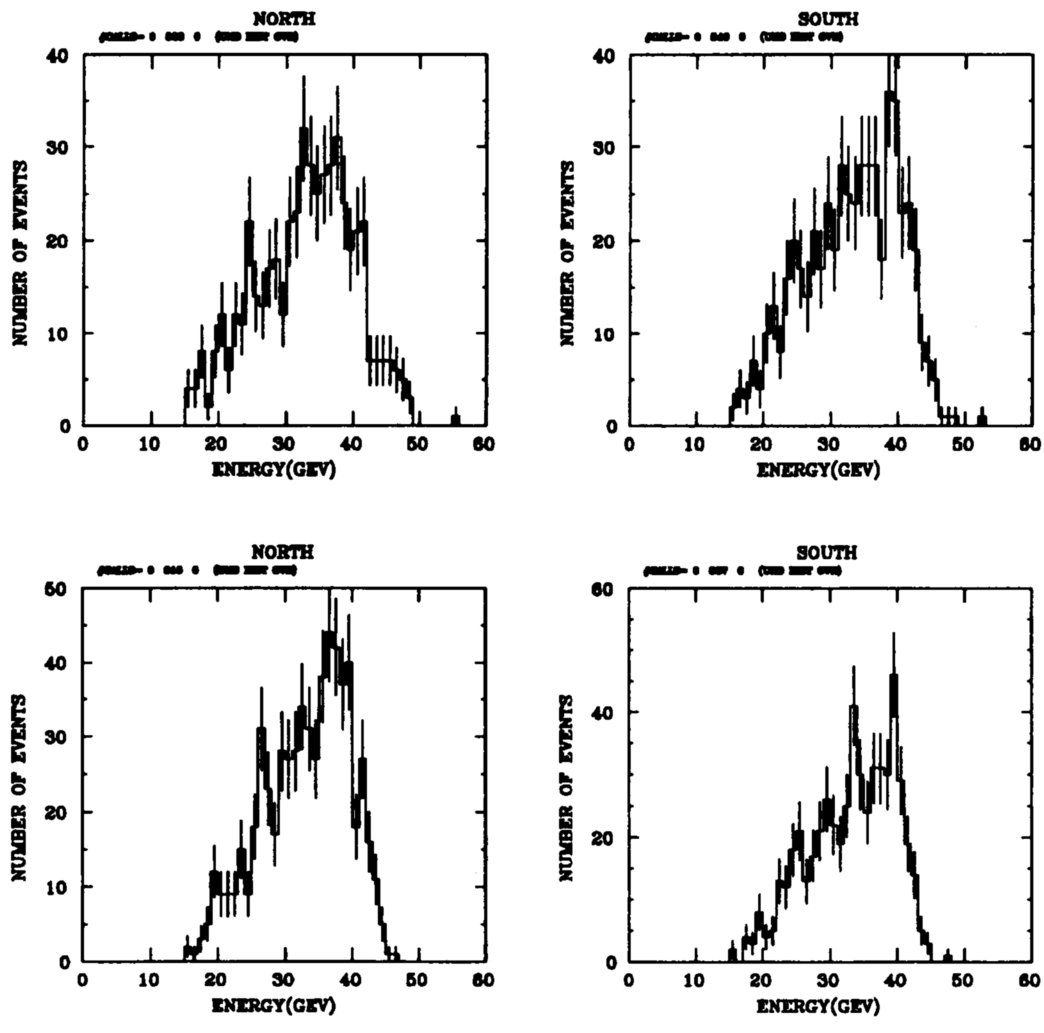

Figure 60: Energy distributions for the main cluster energy for events with a visible photon. The top figures show data and the bottom figures show full shower Monte Carlo.

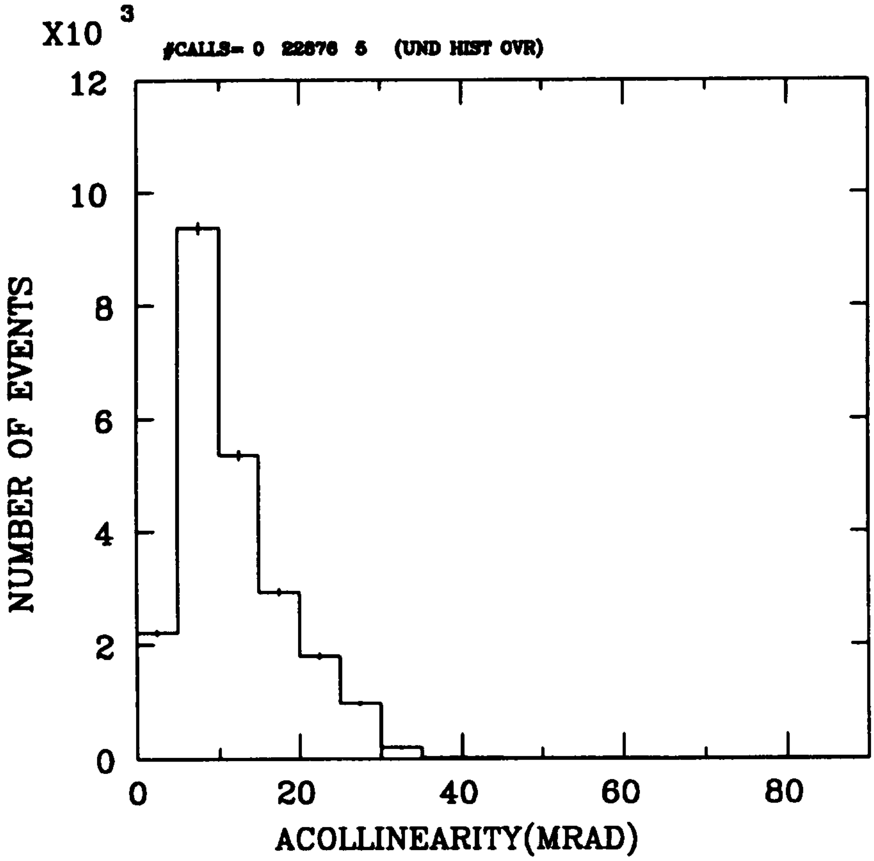

Figure 61: Acollinearity distribution for BHLUMI vector events which have a photon of at least 5 GeV down the beampipe.

Figure 62 shows the acollinearity distribution for the general set of all BHLUMI events that pass the basic set of cuts to classify them as precise-precise or gross-precise events, with no cut on $\Delta\phi$. A much greater percentage of these have small acollinearity, which demonstrates that acollinearity > 5 mrad is a distinguishing feature of events with a photon down the beampipe. The 5 GeV cut is placed on the beampipe photons because in the real data, with position and energy smearing due to the detector resolution, missing low angle photons with energy less than 5 GeV cannot be reliably identified.

The cuts applied to data to select events with at least one photon down the beampipe are as follows:

$$E_N + E_S \geq 35 \ \text{GeV} \tag{24}$$

$$E_N \geq 15 \ \text{GeV} \quad \text{and} \quad \mathrm{E_S} \geq 15 \ \text{GeV} \tag{25}$$

$$E_N \leq 125 \ \text{GeV} \quad \text{and} \quad \mathrm{E_S} \leq 125 \ \text{GeV} \tag{26}$$

$$\text{precise} - \text{precise} \ \text{or} \ \text{gross} - \text{precise} \ \text{event} \tag{27}$$

$$E_N \leq 42 \ \text{GeV} \ \text{or} \ \mathrm{E_S} \leq 42 \ \text{GeV} \tag{28}$$

$$\text{acollinearity} \geq \ 5 \ \text{mrad} \tag{29}$$

$$\text{event not already identified with separate photon in the LMSAT} \tag{30}$$

$$\mathrm{E_{N\ cluster}/E_{N\ total}} \geq .5 \ \text{or} \ \mathrm{E_{S\ cluster}/E_{S\ total}} \geq .5 \tag{31}$$

$$\text{if} \ \mathrm{E_3} > 10 \ \text{GeV}, \ \text{then} \ \theta_3 \ \text{must be} \ < 65 \ \text{mrad} \ (\mathrm{E_3}, \ \theta_3 \ \text{defined below}) \tag{32}$$

The first three cuts are the same basic cuts that apply to all events identified as a Bhabha in the gross-precise or precise-precise region but without a $\Delta\phi$ cut. The energy cut of 42 GeV allows for some smearing, since we are searching for events with a photon of at least 5 GeV down the beampipe, and thus at least 5 GeV of missing energy. The acollinearity cut helps ensure that non-radiative events that happen to have somewhat lower than average energy in the cluster due to fluctuations, leakage, etc. are not counted as events with beampipe photons. As was shown in Figure 61, only 9.7% of events with a 5 GeV or greater photon down

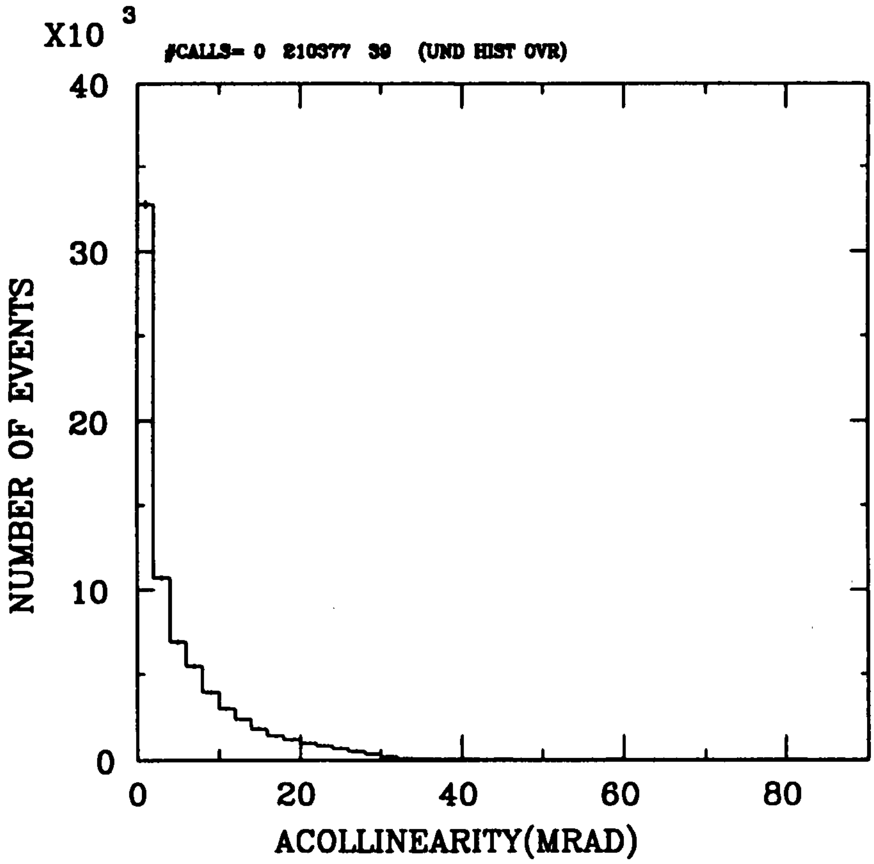

Figure 62: Acollinearity distribution for BHLUMI vector events which pass cuts for being a precise-precise or gross-precise event except they need not pass the $\Delta\phi$ cut.

the beampipe will be lost by this cut. The cut excluding events with identified separate photons is used since events with separate visible photons also are non-collinear and will appear to have missing energy if only the main clusters are considered. The cut on the ratio of the cluster energy to the total energy eliminates noisy events with noise spread over a large area in the luminosity monitor. The last cut excludes events with a photon at large angles, outside the LMSAT and which will also have missing energy and usually an acollinearity larger than 5 mrad. To apply this cut, the vector sum of the momentum vectors of the largest clusters on each side of the interaction point is formed. Then a third vector is calculated, which, when added to the vector sum of the other two, sums to zero. This third vector represents the momentum of a third particle (a photon) which conserves momentum. The energy and theta angle for this vector are represented by E_3 and θ_3 in the list of cuts above. This third vector will give an approximation for the expected direction and energy of the photon, but it will not be exact due to position and energy resolution smearing and also, there may be more than one photon. For these reasons, the third vector is not accurate enough to reliably predict the angle and energy of low energy photons at small angles. However, it does accurately indicate the presence of high energy photons at large angles ($E_3 > 10$ GeV, $\theta_3 >$ 65 mrad), and it is used to exclude events with photons at large angles outside the LMSAT which would otherwise pass the cuts for events with a photon down the beampipe. These large angle photons are detectable in the LAC but LAC data was not recorded when the events were originally filtered off the raw data tapes.

6.5.2 Monte Carlo Cross Section Determination

An insufficient number of full shower events is available for an accurate cross section measurement for events with a photon down the beampipe using full shower events alone. As before, cuts are applied to the four vectors in a larger sample of events. A sample of 6329 full shower events which contains events of all types, is used to study the cuts applied to data and compare with the results using four vector cuts.

It is important here to use all types of events to study the cuts, since events with a large photon outside the LMSAT at large angles will also have missing energy and acollinearity greater than 5 mrad, and may pass the full shower cuts as an event with a photon down the beampipe. The cut efficiency will be determined by comparison of the vector and full shower cuts.

The cuts applied to the four vectors in the BHLUMI events are more straightforward in this case than they were for the events with a separate photon in the LMSAT, since for those events the cuts had to determine not only the existence of a photon in the LMSAT, but had to establish criteria for whether it would form a distinct cluster from the e^+ or e^- cluster. In this case, the four vectors are combined as usual, and the combined vectors are used to classify an event as precise-precise or gross-precise, passing the usual energy cuts, but with no $\Delta\phi$ cut. In addition, an acollinearity cut is imposed, requiring the acollinearity to be greater than 5 mrad, since such a cut is necessary in the data to reduce noise effects. Then, if there is at least one photon at an angle less than 28 mrad, and having energy ≥ 5 GeV, that event is flagged as an event having a beampipe photon.

To study the cuts applied to the data, a special set of full shower BHLUMI events which all have a photon down the beampipe were used as well as the general set. Only the general set is used, however, to determine the overall efficiency of the cuts and the necessary corrections. Identical cuts to those applied to data to select events with a beampipe photon can be applied to the full shower events and the number of passing events compared with the result from the four vector cuts. In the general set of 6329 full shower events, 248 events pass the vector cuts with a photon down the beampipe of at least 5 GeV. Twelve events pass the vector cuts but fail the full shower cuts, and 46 events fail the vector cuts but pass the full shower cuts. The net effect then is an excess of 34 events if data cuts are applied to the full shower events. Thus, in order to compare the Monte Carlo cross section for beampipe photon events with the data, the number of data events will be corrected down by $12.1\% \pm 2.7\%$.

The predicted cross section for events with photons of at least 5 GeV down the beampipe is calculated using 1,682,707 BHLUMI 2.01 events. The number of events passing the vector cuts was 60,241. This number is already corrected for the measured displacement in the luminosity monitor, since the vectors were displaced before cuts were applied. The total BHLUMI cross section for these events is 202.68 ± 0.0987 nbarn. The Monte Carlo cross section is given by the fraction of events passing the cuts for a beampipe photon multiplied by the total BHLUMI cross section, with a resulting value of:

$$\sigma_{\substack{\text{beampipe photon}\\ \text{Monte Carlo}}} = 7.26 \pm .030 \quad \text{nbarn}.$$

A further uncertainty must be added to the error to take into account the uncertainty in the outer acceptance boundary. This uncertainty was determined in the same way as described for the separate photon events, and here an error of ± 0.12 nbarn is combined with the above error. The final Monte Carlo result to compare with data is then:

$$\sigma_{\substack{\text{beampipe photon}\\ \text{Monte Carlo}}} = 7.26 \pm 0.124 \quad \text{nbarn}.$$

6.6 Comparison of BHLUMI with Data for Events with Photons In the Beampipe

The following sections describe the comparison between BHLUMI and data for events with at least one photon with energy $\geq$ 5 GeV radiated down the beampipe. Comparisons will be made for the cross section and the acollinearity distribution. Several corrections are made to the data to correct for systematic errors.

6.6.1 Systematic Effects for the Beampipe Photon Events

The systematic errors which affect the beampipe photon events are similar to those for the visible photon events. The displacement effect is again included in the Monte Carlo cross section, by displacing the vectors before the cuts are applied.

Dead Tower and Trigger Efficiency

The combined effect of the one dead tower in the 1993 run and the slight inefficiency of the trigger causes a small decrease in the number of beampipe photon events detected. This effect was studied by using a sample of 2191 full shower radiative BHLUMI events, as well as the 4552 general events. The energy in the dead tower is set to zero, and the online trigger is applied. The number of passing events is 978, compared to 998 which pass when the dead tower is not zeroed and no trigger is required. Thus it was determined that the trigger and dead tower combine to cause a loss of 2.05% $\pm$ .46% of the events. The correction to the data sample is made by adding 276.2 $\pm$ 61.8 events.

SLC Noise

Beam noise mixed with a Bhabha may cause an event with a photon down the beampipe to fail the cuts since enough energy may be added to the main clusters to raise the energy above the cut of 42 GeV. The effect was studied by overlaying a sample of luminosity weighted random events from SLD onto 2191 full shower radiative BHLUMI events and then applying the beampipe photon event cuts. The net effect of the noise is to cause good events to be lost. The correction required adding 3.9% $\pm$ 0.2% to the data sample, which is equivalent to 530.9 $\pm$ 22.6 events.

Energy Measurement

The data was corrected for the local hardening effect before applying cuts for beampipe photons, but events are lost at the trigger level due to this effect. This effect was studied by using the sample of 2191 full shower radiative events and the 4552 general events without correction for the local hardening effect, and flagging the events that fail the trigger. These same events are then corrected for the local hardening effect, and the number that pass the trigger and the beampipe photon cuts after the correction represent the percentage of events lost in data at the trigger stage. The result was that the data sample must be corrected upward by 1.1% ± 0.37%, or 149.2 ± 49.7 events.

Cut Efficiency and Background

The data must be corrected for the net effect of the efficiency of the cuts and background from non-radiative events or events which do not meet the criteria of the vector cuts. The net effect is that more events pass data cuts compared to vector cuts, so the data must be corrected downward by 12.1% ± 0.27%. The raw number of data events is 13,508, so this number must be corrected down by 1628.7 ± 365.3 events.

Monte Carlo

As described in Section 6.5.2, the Monte Carlo cross section must be corrected for the effect of displacement and the uncertainty in the outer acceptance boundary.

6.6.2 Cross Section Measurement

The raw number of events with beampipe photons in the data is 13,508. The average luminosity measured in Chapter 5 will be used to calculate the cross section using $\sigma_{beampipe\ \gamma} = N_{beampipe\ \gamma}/\mathcal{L}$. Table 8 summarizes the corrections made to the data. The measured cross section in data is then given by:

Table 8: Corrections to raw number of beampipe photon events

Correction Type	Number of Events	nbarn
trigger and dead tower	+276.24 ± 61.82	+0.1604 ± .0359
local hardening	+149.17 ± 49.74	+0.08660 ± 0289
SLC noise	+530.93 ± 22.57	+0.3082 ± .0131
cut efficiency,background	-1628.66 ± 365.26	-0.9455 ± .212
statistical	±116.224	± .0675

$$\sigma_{\mathrm{beampipe}} = \frac{N}{\mathcal{L}} = \frac{12835.7 \pm 374.5_{sys} \pm 116.2_{stat}}{1722.49 \pm 7.79\ \ \mathrm{nbarn}}$$

$$\sigma_{\text{beampipe}} = 7.45 \pm 0.22_{sys} \pm 0.07_{stat} \pm 0.03_{lum} \ \text{nbarn}.$$

The BHLUMI prediction for the cross section was

$$\sigma_{\text{BHLUMI}} = 7.26 \pm .12 \ \text{nbarn}$$

again in reasonable agreement within errors.

6.6.3 Acollinearity

A comparison of the acollinearity distribution of the events with a photon down the beampipe in data and Monte Carlo is also of interest to examine how well BHLUMI describes this type of radiative event. Figure 63 shows the acollinearity

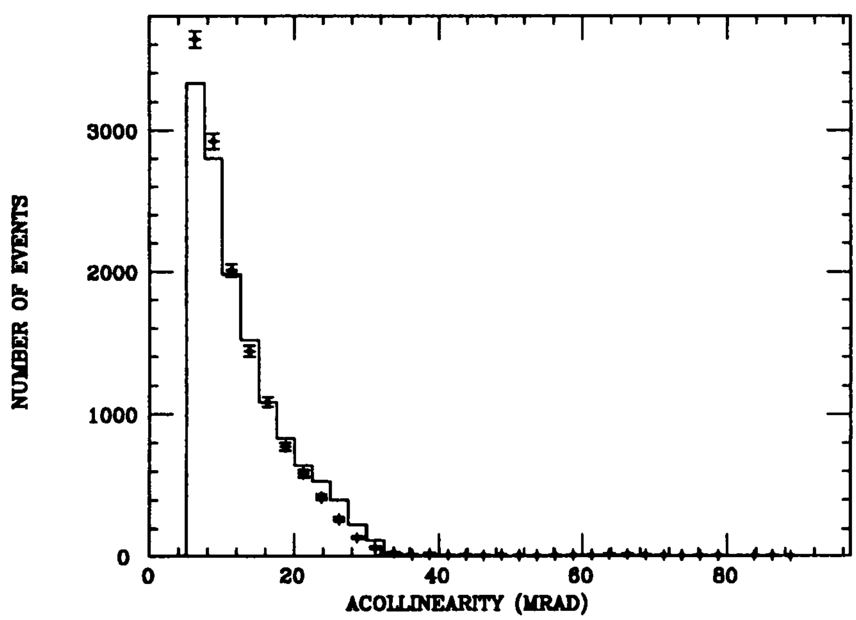

Figure 63: Acollinearity distribution for data (points) and vector BHLUMI events (histogram) with a photon down the beampipe.

distribution of data events and BHLUMI vector events. This figure shows that BHLUMI reproduces the acollinearity distribution well. Figure 64 shows the energy distribution of the main cluster energy on each side of the interaction point, for events selected to have a photon down the beampipe for both data and full shower Monte Carlo events.

6.7 Conclusions

The comparison of cross section, acollinearity, and photon energy between data and BHLUMI for the two types of radiative events studied show that the QED theory which describes radiative Bhabhas with a hard photon is well represented in BHLUMI. The cross sections agree, and the distributions compare well.

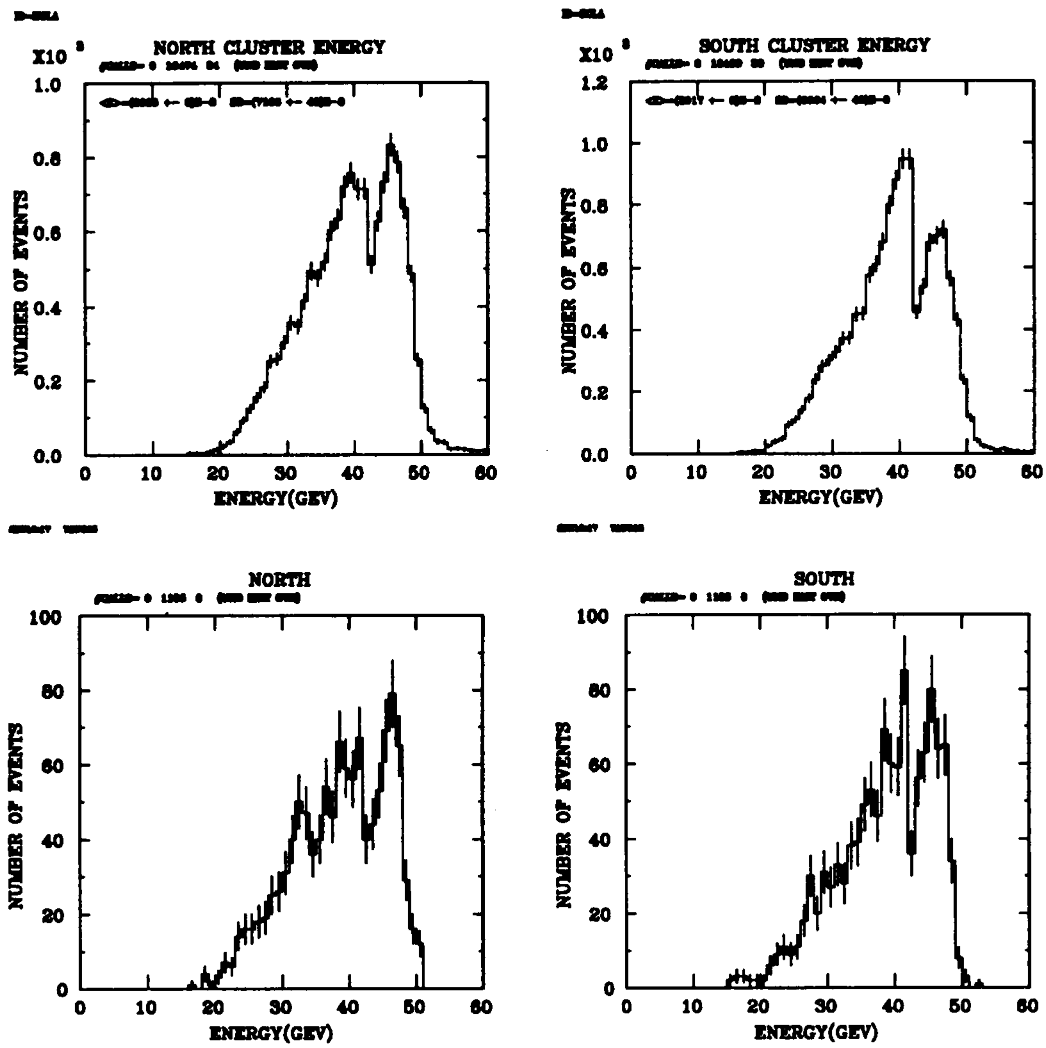

Figure 64: Energy distributions using the main clusters for North and South LMSATs for events with a photon down the beampipe. The top figures are data, the bottom figures are full shower Monte Carlo.

Chapter 7

Conclusions

Small angle Bhabha scattering has been used to measure the luminosity at SLD for the 1993 run. A silicon tungsten luminosity monitor was used to detect the Bhabha scattering events, and a description of this device and its performance characteristics were presented. The luminosity was measured using two different methods to correct for small displacements of the luminosity monitor, and the results were:

$$\mathcal{L} = 1726.5 \pm 5.1_{stat} \pm 3.9_{sys} \pm 4.6_{MC} \ \text{nbarn}^{-1}$$

$$\mathcal{L} = 1718.5 \pm 5.0_{stat} \pm 2.2_{sys} \pm 5.5_{MC} \ \text{nbarn}^{-1}$$

The BHLUMI 2.01 Monte Carlo program was used to determine the theoretical cross section for Bhabha scattering.

A study of radiative Bhabha events at small angles, (28-68 mrad) was also undertaken. Two types of radiative events were studied, those with a visible photon in the luminosity monitor and events with an undetected photon radiated down the beampipe. The cross section for these types of events in the luminosity monitor acceptance region was measured by counting the number of events of this type and dividing by the measured luminosity. The measured cross section for the events with a visible photon in the luminosity monitor was:

$$\sigma_{sep\ photon} = 0.644 \pm 0.019_{stat} \pm 0.013_{sys} \pm 0.003_{lum} \ \text{nbarn}$$

and the prediction from BHLUMI was:

$$\sigma_{BHLUMI} = 0.665 \pm 0.025 \text{ nbarn.}$$

For events with a photon down the beampipe, the measured cross section was:

$$\sigma_{\mathbf{beampipe}} = 7.45 \pm 0.22_{sys} \pm 0.07_{stat} \pm 0.03_{lum} \text{ nbarn}$$

and the BHLUMI prediction for the cross section was:

$$\sigma_{\mathrm{BHLUMI}} = 7.26 \pm .12 \text{ nbarn.}$$

In both cases the measured value and Monte Carlo predictions agreed within errors. Characteristics of the radiative events, the photon energy distribution and acollinearity distributions, were also compared to BHLUMI distributions and it was shown that BHLUMI reproduced the characteristics of the data, confirming that radiative corrections are well described by BHLUMI.

BIBLIOGRAPHY

Bibliography

[1] S. L. Glashow. Nuclear Physics, **22**:579, (1961).

[2] S. Weinberg. Physical Review Letters, **19**:1264, (1967).

[3] A. Salam and J.C. Ward. Physics Letters, **13**:168, (1964).

[4] Francis Halzen and Alan D. Martin. *Quarks and Leptons: An Introductory Course in Modern Particle Physics.* John Wiley and Sons, 1984.

[5] William B. Rolnick. *The Fundamental Particles and their Interactions.* Addison-Wesley Publishing Company, 1994.

[6] F. Abe *et. al.* Physical Review Letters, **74**:2626, (1995).

[7] S. Abachi *et. al.* Physical Review Letters, **74**:2632, (1995).

[8] H. J. Bhabha. Proceedings of Royal Society, **A154**:159, (1935).

[9] S. Jadach, E. Richter-Was, B.F.L. Ward, and Z. Was. Computer Physics Communication, **70**:305, (1992).

[10] D. R. Yennie, S. C. Frautschi, and H. Suura. Ann. Phys. (NY), **13**:379, (1961).

[11] Stanislaw Jadach and B.F.L. Ward. Physical Review, **D40**:3582, (1989).

[12] S. Jadach, E. Richter-Was, B.F.L. Ward, and Z. Was. Physics Letters, **B268**:253, (1991).

[13] S. Jadach, E. Richter-Was, B.F.L. Ward, and Z. Was. Physics Letters, **B253**:469, (1991).

[14] S. Jadach, E. Richter-Was, B.F.L. Ward, and Z. Was. Physics Letters, **B260**:438, (1991).

[15] F.A. Berends and R. Kleiss. Nuclear Physics, **B228**:537, (1983).

[16] F.A. Berends, R. Kleiss, and W. Hollik. Nuclear Physics, **B304**:712, (1988).

[17] C. Y. Prescott. Prospects for Polarized Electrons at High Energies. SLAC-PUB-2630, (October, 1980).

[18] G.S. Abrams *et. al.* Nuclear Instruments and Methods, **A281**:55, (1989).

[19] G.S. Abrams *et. al.* Physical Review Letters, **63**:1558, (1989).

[20] SLAC Linear Collider Conceptual Design Report. SLAC-Report 229, (June, 1980).

[21] Martin Breidenbach (representing the SLD and SLC Collaborations). SLC and SLD – Experimental Experience with a Linear Collider. In *Waikola Linear Collider*, pages 30–45, 1993. SLAC-PUB-6313, (August, 1993), presented at the 2nd International Workshop on Physics and Experiments with Linear Colliders, April 26-30, 1993.

[22] Morris L. Swartz (representing the SLD and SLC Collaborations). First Measurement of the Left-Right Z Cross Section Asymmetry in Polarized e^+e^- Collisions at the SLC. In *Nagoya Spin Workshop*, pages 195–204, 1992. SLAC-PUB-6034, (January, 1993), presented at the 10th International Symposium on High Energy Spin Physics, Nagoya, Japan, November 9-14, 1992.

[23] Nan Phinney. The Heart of a New Machine. SLAC Beam Line, **24**:2, (1994).

[24] J. Frisch *et. al.* Operation of a Ti:Sapphire Laser for the SLAC Polarized Electron Source. SLAC-PUB-6165, (April, 1993).

[25] T. Maruyama *et. al.* Physical Review B, **46**:4261, (1992).

[26] Raymond E. Frey (representing the SLD Collaboration). SLAC-PUB-6470, OREXP-94-01, (March, 1994), presented at the SLAC Summer Institute on Particle Physics: Spin Structure in High Energy Processes, Stanford, CA, July 26-August 6, 1993.

[27] T. Maruyama *et. al.* Physical Review Letters, **66**:2376, (1991).

[28] Ross C. King. *A Precise Measurement of the Left-Right Asymmetry of Z Boson Production at the SLAC Linear Collider.* PhD thesis, Stanford University, 1994.

[29] K. Abe *et. al.* Physical Review Letters, **73**:25, (1994).

[30] D. Calloway *et. al.* SLAC-PUB-6423, (June, 1994).

[31] Michael J. Fero (representing the SLD Collaboration). The Compton Polarimeter for SLC. In *Nagoya Spin Workshop*, pages 899–904, 1992. SLAC-PUB-6026, (December, 1992), presented at the 10th International Symposium on High Energy Spin Physics, Nagoya, Japan, November 9-14, 1992.

[32] Michael J. Fero (representing the SLD Collaboration). SLAC-PUB-6027,(December, 1992), presented at the SLAC Summer Institute on Particle Physics: The Third Family and the Physics of Flavor, Stanford, CA, July 13-24, 1992.

[33] C.J.S. Damerell *et. al.* Nuclear Instruments and Methods, **A288**:236, (1990).

[34] M.G. Strauss (representing the SLD Collaboration). SLAC-PUB-5970, (October, 1992), presented at Particles and Fields 92, 7th Meeting of the Division

of Particles and Fields of the APS (DPF92), Batavia, IL, November 10-14, 1992.

[35] M.G. Strauss (representing the SLD Collaboration). SLAC-PUB-6686, (October, 1994), presented at the 27th International Conference on High Energy Physics (ICHEP), Glasgow, Scotland, July 20-27, 1994.

[36] M.D. Hildreth *et. al.* Performance of the SLD Central Drift Chamber. In *Nuclear Science Symposium and Medical Imaging Conference, 1994 IEEE Conference Record*, page 277, 1995.

[37] D. Aston *et. al.* Nuclear Instruments and Methods, **A283**:582, (1989).

[38] K. Abe *et. al.* IEEE Transactions on Nuclear Science, **41**:862, 1994.

[39] J. Va'Vra *et. al.* IEEE Transactions on Nuclear Science, **35**:487, 1988.

[40] D. Aston *et. al.* IEEE Transactions on Nuclear Science, **36**:276, 1989.

[41] D. Axen *et. al.* Nuclear Instruments and Methods, **A328**:472, (1993).

[42] Eric Vella (representing the SLD Collaboration). SLAC-PUB-5953, (October, 1992), presented at the III International Conference on Calorimetry in High Energy Physics, Corpus Christi, Texas, September 29– October 2, 1992.

[43] J.E. Brau and T.A. Gabriel. Nuclear Instruments and Methods, **A238**:489, (1985).

[44] J.E. Brau and T.A. Gabriel. Nuclear Instruments and Methods, **A279**:40, (1989).

[45] Hwanbae Park. *A Measurement of the Left-Right Cross Section Asymmetry in Z^0 Production with Polarized e^+e^- Collisions.* PhD thesis, University of Oregon, 1993.

[46] A.C. Benvenuti *et. al.* Nuclear Instruments and Methods, **A276**:94, (1989).

[47] A.C. Benvenuti *et. al.* Nuclear Instruments and Methods, **A290**:353, (1990).

[48] S.C. Berridge *et. al.* IEEE Transactions on Nuclear Science, **36**:339, 1989.

[49] S.C. Berridge *et. al.* IEEE Transactions on Nuclear Science, **37**:1191, 1990.

[50] S.C. Berridge *et. al.* IEEE Transactions on Nuclear Science, **39**:1242, 1992.

[51] Glenn F. Knoll. *Radiation Detection and Measurement.* John Wiley and Sons, 1979.

[52] Achim W. Weidemann. LUM Note 91-03, May 21, 1991, unpublished.

[53] G. Lindstrom *et. al.* M.C. Simulations with EGS4 for Calorimeters with Thin Silicon Detectors. In *SSC Calorimetry Workshop 1989*, pages 215–226, 1989.

[54] E. Borchi *et. al.* CERN-PPE-91-34, (February, 1991), presented at the 2nd International Conference on Advanced Technology in Particle Physics, Villa Olmo, Como, Italy, June 1990.

[55] F. Lemeilleur *et. al.* Physics Letters, **B222**:518, 1989.

[56] A.L.S. Angelis *et. al.* Nuclear Instruments and Methods, **A314**:425, (1992).

[57] Y.B. Bushnin *et. al.* Nuclear Instruments and Methods, **106**:493, (1973).

[58] Kevin T. Pitts. *Electroweak Coupling Measurements from Polarized Bhabha Scattering at the Z^0 Resonance.* PhD thesis, University of Oregon, 1994.

[59] R. Brun, R. Hagelberg, M. Hansroul, and J.C. Lassalle. Geant: Simulation Program for Particle Physics Experiments. User Guide and Reference Manual. CERN-DD/78/2, (July, 1978), revised version.

[60] W. Ralph Nelson, H. Hirayama, and David W.O. Roger. The EGS4 Code System. SLAC-Report-0265, (December, 1985).

[61] L.H. O'Neill *et. al.* Physical Review Letters, **37**:395, (1976).

[62] Guido Barbiellini *et. al.* Nuclear Instruments and Methods, **123**:125, (1975).

[63] J. F. Crawford *et. al.* Nuclear Instruments and Methods, **127**:173, (1975).

[64] U. Amaldi *et. al.* Nuclear Physics, **B145**:367, (1978).

Vita

Sharon Leigh White was born in Dallas, Texas on November 13, 1961. She received her early education there, and benefitted from many good teachers at Zion Lutheran School, and then later at First Baptist Academy, where she obtained her high school diploma in 1980. She entered Texas A&M University in College Station, Texas in the fall of 1980 and received her Bachelor of Science degree in physics in 1984. She received her Master of Science degree in physics from the Univeristy of Colorado in 1986 and her PhD in physics from the University of Tennessee in 1995, in experimental high energy physics.